Validation of Physical Processes in the Geant4 Simulator for the Gamma-ray Satellite GLAST (GLASTGeant4)

M1279003

Department of Physics, Hiroshima University

March 18, 2002

Abstract

In this paper, we have validated the physical processes reproduced by the Geant4 to perform the simulation for the development of the GLAST (Gamma-ray Large Area Spece Telescope) with a reliability. The Balloon experiment for the GLAST has been performed on August, 2001 at Palestine, Texas and Geant4 2.0 has been used for the simulation. What we have validated are the processes related to the observation of GLAST satellite, e.g. the ionization and electromagnetic cascades in the materials used in the GLAST satellite. As for the ionization, we have investigated the stopping power, dE/dx, due to the ionization, the most probable energy loss of Landau distribution and range of protons, and have found that the Geant4 reproduced the theoretical values quite well. On the other hand, the narrow shower development in the electromagnetic cascades of the Geant4 has been found by comparing with the experiment and the EGS4 simulator. To seek the origin of narrow shower profile, we have looked further into the physical processes in the electromagnetic cascade, e.g., Møller scattering, Bhabha scattering, bremsstrahlung and pair production. Then the problem of the implementation of the angular distribution for pair creation have been found in the Geant4 code and we have modified it. As a result we have appropriately fixed it and the modified angular distribution has come to follow the theoretical one. Other processes has agreed with the theoretical predictions. However the narrow shower development have not been improved, and the cause of this discrepancy is unknown at present. In this paper we discuss these results of the validation.

Contents

Chapter 1

Introduction

Around 1970s the X- and gamma-ray observation of astrophysical sources by satellites was started. These satellites are UHURU (1970) and Einstein (1978) for X-ray observation, OSO III (1967), SAS-2 (1973) and COS-B (1975) for gamma-ray observation. The diffuse gamma-ray emission of the Milky Way was detected and many pulsars and quasars already identified in other wavelength were also discovered to emit X- and gamma-rays. The Energetic Gamma Ray Experiment Telescope (EGRET) instument on NASA's Compton Gamma-Ray Observatory (CGRO), launched in 1991, found more gamma-ray objects and measured the distribution of gamma-ray emission along the Galactic plane with improved position accuracy than previous observations. This emission is thought to be due to the interactions between cosmic-rays and interstellar matter. The development of gamma-ray observation will enable us to determine the distribution of materials in our galaxy without any bias. The EGRET also conducted the first complete survey of the sky in the range from 30 MeV to 10 GeV. Although it discovered many gamma-ray pulsars and blazars, about half of the detected gamma-ray sources remain unidentified. To investigate the property of these sources the measurement of electromagnetic spectrum and variability with higher sensitivity is essential. To search the counterparts in other wavelength the improvement of spatial resolution is also needed.

The important processes for the study of the high-energy phenomena in the universe are synchrotron radiation of high-energy electrons and positrons, non-thermal bremsstrahlung of high-energy electrons, inverse compton scattering between high-energy electrons and soft photons and line gamma-ray emission from the π^0 decay, which is produced by the interaction between cosmic protons and interstellar matter. These processes are strongly related to particle acceleration. Therefore, the gamma-ray observation is suitable for the study about the cosmic-ray acceleration. The results of EGRET observation indicate that many high-energy phenomena occur in the universe, where electron/positron plasma were accelerated in the shock front of the super nova remnant, pulsar wind, black hole candidates and active galactic nuclei. These high-energy objects are the most probable candidates in which cosmic-ray electrons are accelerated effectively. They may also accelerate protons, hence can be a source of cosmic ray protons. The next generation gamma-ray satellites are expected to confirm this scenario.

The Gamma-ray Large Area Space Telescope (GLAST) is an international mission that will study the high-energy phenomena in gamma-rays universe. The GLAST will be launched by NASA in 2006. The energy range, field of view and angular resolution of the GLAST are vastly improved in comparison with those of the EGRET so that the GLAST will provide a factor of 30 or more advance in the sensitivity as shown in Table 1.1. The number of gamma-ray objects to be discovered are expected to increase greatly. The GLAST is also expected to make an answer to the unsolved questions raised by previous gamma-ray observation and yield many unanticipated findings.

Table 1.1: GLAST specifications and performance compared with EGRET

Quantity	EGRET	GLAST (Minimum Spec.)
Energy Range	20 MeV - 30 GeV	20 MeV - 300 GeV
Peak Effective Area	1500 cm^2	>8000 cm^2
Field of View	0.5 sr	>2 sr
Angular Resolution	5.8° (100 MeV)	<3.5° (100 MeV)
		<0.15° (>10 GeV)
Energy Resolution	10 %	<10 %
Deadtime per Event	100 ms	<100 μs
Source Location Determination	15′	<0.5′
Point Source Sensitivity	$\sim 1 \times 10^{-7}$ cm^{-2} s^{-1}	$<6 \times 10^{-9}$ cm^{-2} s^{-1}

The GLAST is a very complex system, and detailed computer simulations are required to design the instrument, to construct the response function and to predict the background in the orbit. The simulations are used to filter out the instrumental background, produce realistic triggering and readout schemes and evaluate the performance of the instrument after background rejection. To accomplish these tasks, we use object-oriented C++ toolkit called Geant4 [1], which is useful for the simulation of the passage of particles through matter. Its application areas include high energy physics and nuclear experiments, medical science, accelerator and space physics studies. However it is only three years since its public release in December 1998. Therefore, the systematic validation of the simulator and evaluation how it affects the performance of the GLAST are required. The validation of physical processes of Geant4 is the main theme of this thesis.

Chapter 2

GLAST Satellite Development

2.1 Overview of GLAST Satellite

The Gamma-ray Large Area Space Telescope (GLAST) is an international and multi-agency space mission that will study the universe in the energy range from 20 MeV to 300 GeV. The GLAST will be launched by NASA in March 2006. The main instrument, the Large Area Telescope (LAT), is e^+e^- pair production telescope and consists of a 4×4 array of identical towers, which are composed of the tracker, calorimeter and data acquisition module. The schematic view of the intrument is shown in Fig.2.1. It measures the direction and energy of incident gamma-ray simultaneously. The trajectories of the resulting electron and positron from pair production in the tracker are measured and their energies are then measured by the calorimeter. Employing the single-side Silicon Strip detector through successive planes in the tracker achieves a few arcminutes of the angular resolution and wide field of view which covers 20 % of all sky at once. The GLAST can survey intermittently the all sky within a few hours so that it can widely study from the active galactic nuclei flares on the short time scales to the objects which show weak valiability on time scales of a year, and will increase the number of gamma-ray objects greatly. The energy range, field of view and angular resolution of the GLAST are vastly improved in comparison with those of EGRET and the GLAST will provide a factor of 30 or more advance in the point-source sensitivity. The GLAST is expected to make an answer to the unsolved questions arised by previous gamma-ray observation and also provide many

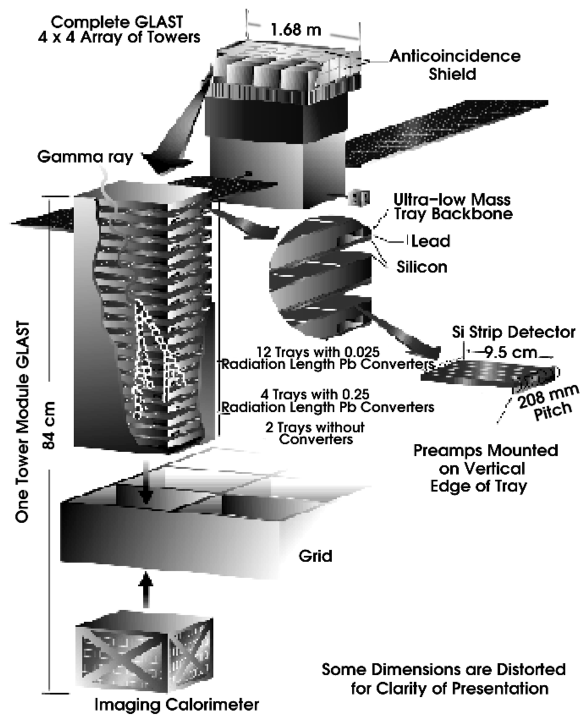

Figure 2.1: Schematics of the LAT instrument composed of the Si detector layers, the stacking of the CsI crystals in the calorimeter and the integration of the data acqusition systems.

unexpected discoveries.

2.2 GLAST Simulation

2.2.1 Overview

To exploit the full capability of the GLAST-LAT the instrumental background (all events of non-gamma ray origins) needs to be filtered out to about 10% of the extragalactic gamma ray flux [2]. Potential background events are predicted to be mostly due to interactions with cosmic-ray particles. These particle fluxes vary over the satellite orbit and over the solar cycle. Thus their event rate and characteristics have to be predicted accurately as a function of time and location along the orbit. Hardware configuration and software algorithm to filter out background have to be optimized based on thorough studies of all possible background event types.

Once the instrumental background is reduced to the required level, bit patterns and pulse heights recorded in the the GLAST-LAT have to be reconstructed accurately. Here direction, energy and probability for being non-gamma ray origin are to be extracted out. Errors in their estimations have to be assessed. To accomplish these two major tasks, we need a reliable simulation program. The only candidate available at present is Geant4 [1]. This is an object-oriented C++ toolkit for the simulation of the passage of particles through matter and provides a complete set of tools for all the elements of detector simulation: Geometry, Tracking, Detector Response, Run, Event and Track management, Visualisation and User Interface. An abundant set of physics processes handle the various interactions of particles with matter across a wide energy range.

2.2.2 Balloon Flight Experiment of GLAST

The GLAST is now under development, and to verify the performance of the GLAST-LAT instrument in a space-like environment and to validate the reconstruction software and the background rejection scheme, the Balloon Flight Engineering Model (BFEM) of the GLAST was launched on August 4, 2001 at Palestine, Texas. The BFEM represents one of the 16 towers that compose the GLAST-LAT instrument and also has four eXternal Gamma-ray Target scintillators (XGTs) above the instrument which act as sources of tagged gamma-rays as shown in Fig.2.2(a) [3]. To study the cosmic-ray background we constructed a simulation program of the BFEM based on the Geant4 and the cosmic-ray generators.

Geometry and Physics Processes

In order to build a reliable simulator, the geometry of the real BFEM instrument should be reproduced by the Geant4. The tower of the BFEM instrument consists of the Tracker, the Calorimeter, the Anti Coincidence Detector, data acquisition electronics, a pressure vessel, four eXternal Gamma-ray Target scintillators (XGTs) and other support structures. All components are precisely reproduced in the simulator as shown in Figure 2.2 (b). For example we show the geometry of the Tracker and Calorimeter in the simulator in Figure 2.3 and 2.4, respectively. There are 14 trays in the Tracker and five types of the trays of different material composition exist. Among them, Standard Tray is shown in Figure 2.3. In the simulator every kinds of tray are appropriately reproduced.

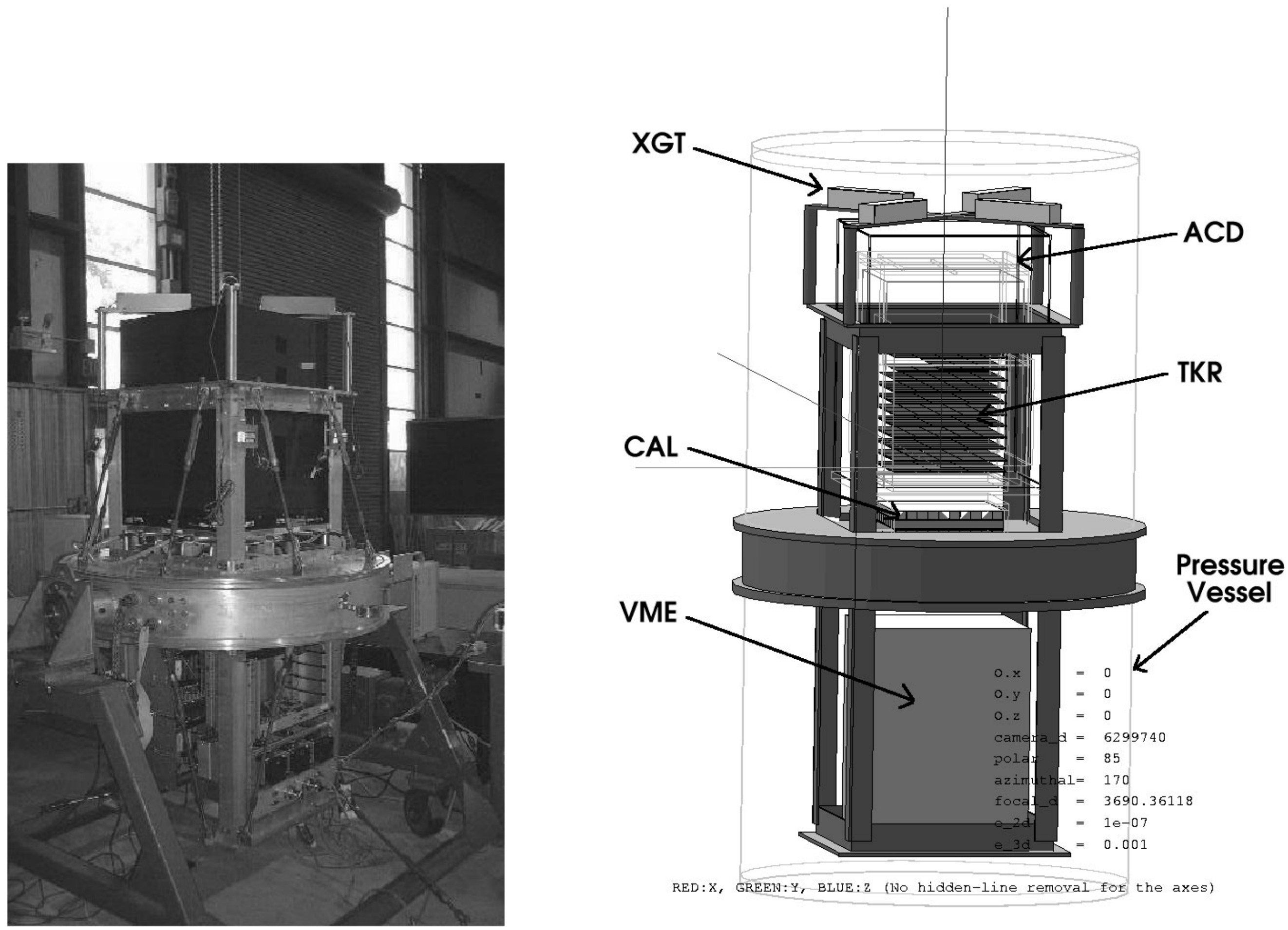

(a) (b)

Figure 2.2: (a)Picture of the BFEM instrument before being enclosed in Pressure Vessel to keep the pressure during the flight. It has four XGTs above the instrument to act as sources of tagged gamma-rays. (b) Detector geometry of the Geant4 BFEM simulator which precisely reproduce that of the real instrument. The cosmic-ray generator is also implemented to produce the same radiation environment during the flight.

The Calorimeter consists of 8 identical trays placed alternately in two perpendicular directions to get the two dimensional position of energy deposition as shown in Figure 2.4. Each tray has 10 CsI crystals. Components surrounding CsI crystal, e.g., wrapping materials, rubber, and Al sheets, as well as support frames, are also reproduced in the simulator. Details about the geometry implemented in the simulator can be refered from other article [4]. The model of the cosmic-ray flux is also included to represent a radiation environment and the detailed discussion is summarized in other article [5].

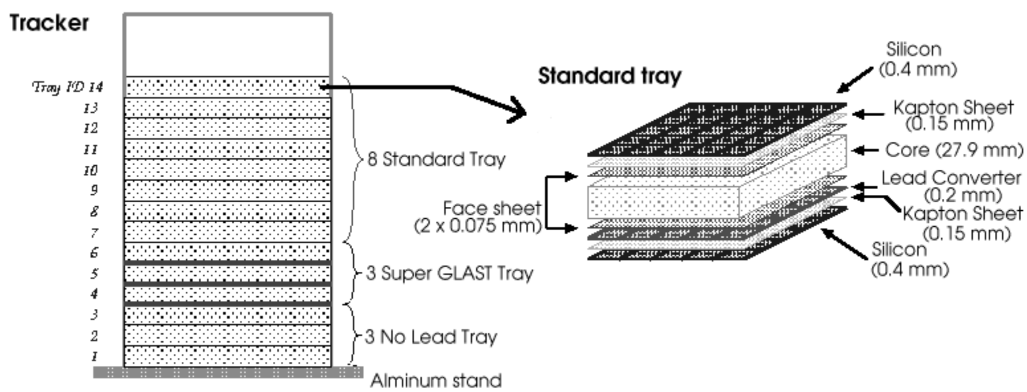

Figure 2.3: The geometry of the tracker and Standard Tray implemented in the simulator. The Tracker consists of 8 Standard Trays, 3 Super GLAST Trays, and 3 No Lead Trays. Standard Tray is composed of Silicon Strip Detectors (SSDs), two kapton sheets, core and lead converter.

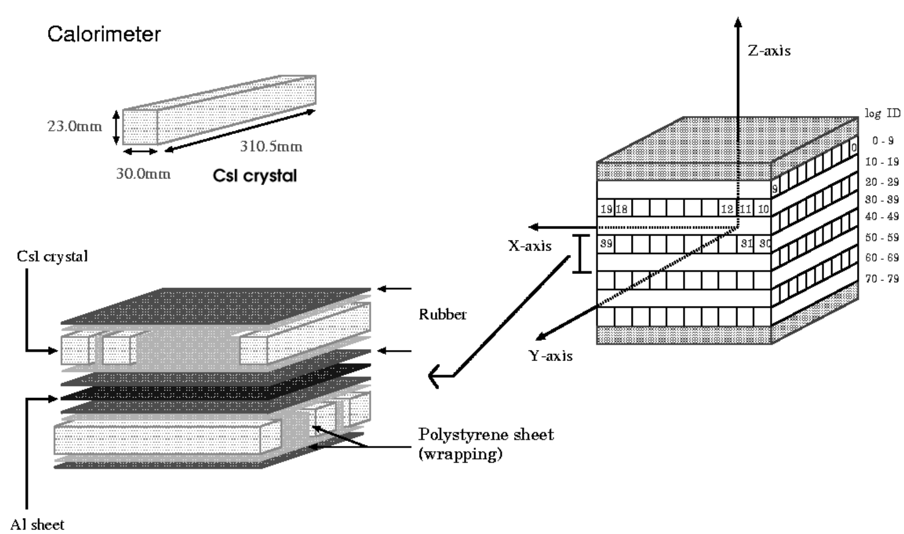

Figure 2.4: The geometry of the calorimeter and CsI crystal. The Calorimeter consists of 8 trays and each tray, composed of 10 CsI crystals, is placed alternately in two perpendicular directions.

Geant4 provides various kinds of electromagnetic, hadronic and other physics process, and one must define which physics process to be used in the simulator. Following physics processes are implemented in the BFEM simulator.

- General Process
  Decay
- Electromagnetic Processes
  ionization, multiple scattering, photoelectric effect, compton scattering, pair production, bremsstrahlung, e^+e^- annihilation
- Hadronic Processes
  elastic scattering, inelastic scattering

Summary of the Simulation

We estimated the event rate on the balloon flight. As a result of the comparison between the observed data and the simulation results, the observed trigger rate was reproduced quite well by our BFEM simulation program, indicating that both the cosmic-ray generator and BFEM simulation programs are basically appropriate. These studies also provide us with opportunity to validate Geant4. The detailed results are discussed in other paper [5, 6].

2.3 Necessity of Validating Physical Processes in Geant4

The Geant4 has been mainly used in the fields of high energy physics, and the energy range of the GLAST from 20 MeV to 300 GeV is relatively low for Geant4. Futhermore, the Geant4 is only three years since its public release in December 1998 and has not been fully validated in this energy range. Therefore, the systematic validation of the Geant4 simulator, especially around this energy region, and evaluation how it affects the performance of the GLAST are required. We describe the result of the physics process validation and accuracy of the Geant4 in the paper. What we have validated are electromagnetic processes related to gamma-ray observation by the GLAST. We discuss energy loss and range of particles through matter in Chapter 3. The validation of gamma-induced electromagnetic shower then follows in Chapter 4 and Chapter5.

Chapter 3

Validation of Particle Ionization Loss in Matters

The charged particles lose their energy and deflect their incident direction in matters due to the various processes, e.g., the ionization, the emission of Cherenkov radiation, the nuclear reactions, and the bremsstrahlung. The ionization is one of the most fundamental physics processes and also frequently occurs in materials in comparison with other processes except for Cherenkov radiation. In the GLAST simulation, ionization is an essential process because it is related to the background rejection caused by the charged particles, and the measurement of the direction and energy of the incident gamma-rays. Furthermore, the distribution of the energy loss due to the ionization depends on the thickness of the absorbers. The distribution in thin absorbers obeys Landau distribution in form although that in thick absorbers becomes Gaussian. The GLAST satellite includes thin materials, e.g., Silicon Strip Detector in the tracker. Therefore, it is important to confirm whether the Geant4 correctly reproduce these processes related to the ionization or not. In this chapter we exmine the stopping power, dE/dx, of protons, Landau distribution of protons and electrons and the range of protons in materials.

3.1 Energy Loss Distribution

For any given particles, the amount of energy loss is not be equal to the mean energy loss because of the statistical fluctuations which occur in the number of collisions suffered and a energy transfer in each collision. An initially monoenergetic beam, after passing through a given thickness of material, therefore shows a broaden distribution in energy. Calculation of the distribution of energy loss is generally divided into two cases: in thick absorbers and in thin absorbers.

Thick Absorber For relatively thick absorbers where the number of collisions is large, the energy loss distribution can easily be shown to become Gaussian in form. This is because of the Center Limit Theorem; the sum of N random variables, all following the same statistical distribution, approaches the Gaussian-distribution in the limit of N$\rightarrow \infty$. If we take our random variable to be the energy loss in a single atomic collision, and assume that the absorber is thick enough to be N$\rightarrow \infty$ and the energy loss in each collision is so small that the velocity of the particle is negligibly altered (so that the velocity-dependent collision cross-section stays constant), then the total energy loss is the sum of many independent energy loss in a single collision. The average energy loss per unit path length is called the stopping power or dE/dx, which is calculated by Bethe-Bloch formula[7].

Thin Absorber In contrast to the thick absorber case, the number of collisions in thin absorbers is too small for the Center Limit Theorem to hold. Because charged particles suffer large energy deposition in a sigle collision, the distribution of energy loss becomes a skewed, asymmetric form with a long tail to the high energy side. Thus, the mean energy loss no longer corresponds to the peak but is displaced because of the high energy tail. The position of peak now defines the most probable energy loss.

3.2 Bethe-Bloch Formula

3.2.1 Theoretical Equation

To validate the stopping power of the ionization of the Geant4, we shot protons into the thick absorber in the Geant4 simulation and compared the obtained results with Bethe-Bloch formula given as a following equation [7],

$$-\frac{dE}{dx} = 2\pi N_a r_e^2 m_e c^2 \rho \frac{Z}{A}\frac{z^2}{\beta^2}\left[ln(\frac{2m_e\gamma^2 v^2 W_{max}}{I^2}) - 2\beta^2 - \sigma - 2\frac{C}{Z}\right] \tag{3.1}$$

with $2\pi N_a r_e^2 m_e c^2 = 0.1535$ MeVcm^2, and the rest of variables used in the equation are summarized in Table 3.1. The maximum energy transfer, W_{max}, is that produced by a head-on or knock-on collision. For elementary particles and nuclei up to the α-particle, this formula which includes the shell and density corrections gives results accurate to within a few percent for velocities ranging from the relativistic region down to $\beta \simeq 0.1$, which approximately corresponds to 5 MeV for proton. In the energy range of $0.01 < \beta < 0.05$, there is no satisfactory theory for protons.

As we mentioned in the previous section (§3.1), whether the energy distirubtion obeys the Gaussian or Landau distribution depends on the absorber thickness and also energy of the incident particle. We can determine which distribution should be used from the ratio, κ, between the mean energy loss, $\overline{\Delta}$, and the maximum energy transfer, W_{max}, allowable in a single collision. The ratio is expressed as below, [7],

$$\kappa = \overline{\Delta}/W_{max}, \tag{3.2}$$

where $\overline{\Delta} \simeq 2\pi N_a r_e^2 m_e c^2 \rho \frac{Z}{A}(\frac{z}{\beta})^2 x$ and x is the material thickness. For an incident particle of mass, M, kinematics gives

$$W_{max} = \frac{2m_e c^2 \eta^2}{1 + 2s\sqrt{1+\eta^2+s^2}} \tag{3.3}$$

where $s = m_e/M$ and $\eta = \beta\gamma$. If $M \gg m_e$,

$$W_{max} \simeq 2m_e c^2 \eta^2 \tag{3.4}$$

We used this approximate equation to calculate the theoretical stopping power of proton (equation 3.1, 3.2 and 3.4). The distribution shows Gaussian in the region $\kappa > 1$ and approaches the Landau distribution below $\kappa = 1$.

Table 3.1: Summary of variables used in this section

r_e : classical electron radius = 2.817×10^{-13} cm
ρ : density of absorbing material
m_e : electron mass
z : charge of incident particle in units of electron charge
N_a : Avogadro's number = 6.022×10^{23} mol^{-1}
$\beta = v/c$ of the incident particle
$\gamma = 1/\sqrt{1-\beta^2}$
I : mean excitation potential
σ : density correction
C : shell correction
Z : atomic number of absorbing material
A : atomic mass
W_{max} : maximum energy transfer in a single collision

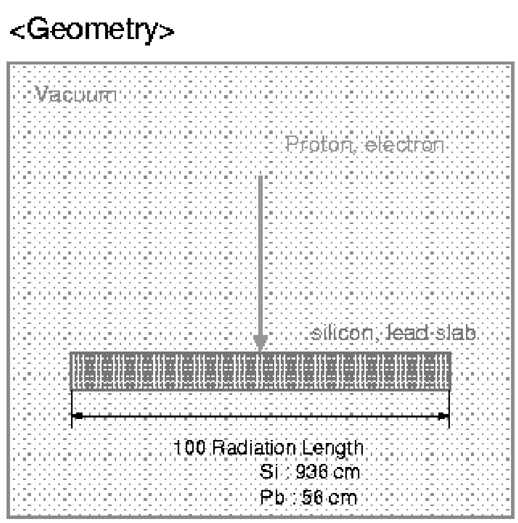

Figure 3.1: The geometry for the simulation to validate the Bethe-Bloch and the Landau distribution. The absorber is a rectangular slab. The width of the layer is 100 radiation length. We changed the absorber thickness according to the incident particle energy.

3.2.2 Geant4 Simulation

We have injected protons of various energies into the silicon and lead absorber, and have measured the energy loss of the incident particle. In the simulator, we must define the cut values, or energy threshold for secondary particle production. If the energy of the secondary particle comes out to be below this value, the secondary particle production is cancelled and the energy is deposited locally. In the Geant4, the cut value is defined as a stopping range and we have set the values as 0.4 mm and 0.1 mm for electron and all other particles, respectively. In the Table 3.2, these cut values are expressed as the total energies. The absorber is a rectangular slab as shown in Figure 3.1 and the thickness has been set so that $\kappa = 3$ except for 3 GeV and 10 GeV protons. Then, we have made the histogram of the energy loss distribution and have fitted it with a Gaussian distribution. From the peak of the Gaussian distribution and the thickness of the absorber, we have calculated the stopping power, dE/dx. In order to collect only the energy loss by ionization, we have discarded events where inelastic scattering occured.

Table 3.2: Cut values used in the Geant4 simulation, shown in total energy of the particle.

Material	Electron	Photon
Silicon	578 keV	2.29 keV
Lead	637 keV	29.3 keV

The results are shown in Figure 3.2, Table 3.3 and 3.4. The Geant4 results in the energy region above 50 MeV are consistent with the theoretical values within $\leq 6\%$. The differences between the Geant4 data and theoretical values are relatively large at 10 MeV for a lead absorber, but is still below 10%. The cause of this difference is unknown. We conclude the conclusion that the Geant4 reproduces the stopping power, dE/dx of protons in lead and silicon absorbers in the range from 10 MeV to 10 GeV.

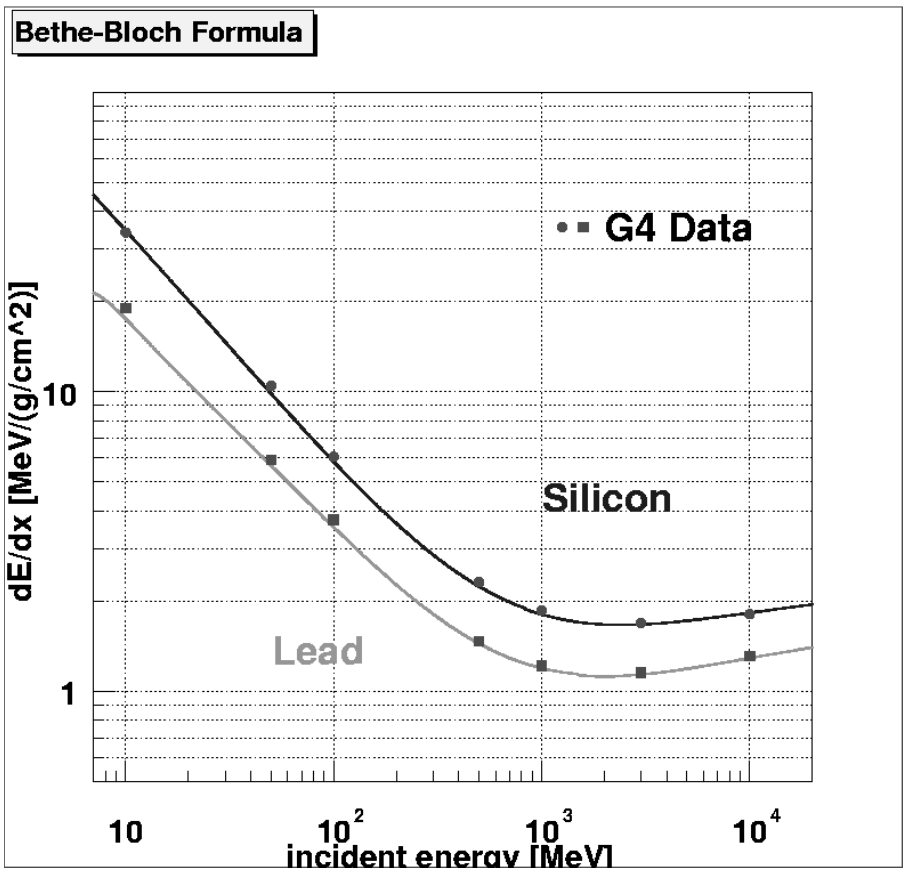

Figure 3.2: The curve of Bethe-Bloch formula (solid line) and the energy loss (filled marks) derived from the Geant4 simulation, in a silicon layer and a lead layer.

Table 3.3: Validation of Bethe-Bloch formula for protons in silicon. The values of κ are 3 except for 3 GeV and 10 GeV proton.

particle energy	thickness (cm)	$\frac{dE}{dx}$ [MeV/(g/cm^2)] (Geant4)	$\frac{dE}{dx}$ [MeV/(g/cm^2)] (Theoretical Value)	difference* between data and theo. [%]
10 MeV	4.00×10^{-3}	34.13 ± 0.29	34.52	-1.1
50 MeV	1.87×10^{-1}	10.46 ± 0.02	9.861	+6.1
100 MeV	7.08×10^{-1}	6.068 ± 0.009	5.843	+3.8
500 MeV	1.33×10	2.317 ± 0.016	2.241	+3.4
1 GeV	4.30×10	1.868 ± 0.041	1.807	+3.4
3 GeV	70.0 ($\kappa = 0.78$)	1.692 ± 0.006	1.674	+1.1
10 GeV	44.0 ($\kappa = 0.06$)	1.810 ± 0.008	1.829	-1.0

$$\text{*difference} = \frac{\text{(Geant4 data - theoretical value)}}{\text{theoretical value}} \times 100$$

Table 3.4: The same as Table 3.3, but for lead.

particle energy	thickness (cm)	$\frac{dE}{dx}$ [MeV/(g/cm^2)] (Geant4)	$\frac{dE}{dx}$ [MeV/(g/cm^2)] (Theoretical Value)	difference between data and theo. [%]
10 MeV	2.00×10^{-3}	19.05 ± 0.04	17.50	+8.8
50 MeV	4.80×10^{-2}	5.926 ± 0.011	5.672	+4.5
100 MeV	1.83×10^{-1}	3.747 ± 0.006	3.530	+6.1
500 MeV	3.45	1.471 ± 0.001	1.443	+1.9
1 GeV	1.11×10	1.217 ± 0.001	1.195	+1.8
3 GeV	69.7 ($\kappa = 1$)	1.155 ± 0.003	1.138	+1.5
10 GeV	19.9 ($\kappa = 0.1$)	1.309 ± 0.009	1.291	+1.4

3.3 Landau Distribution

3.3.1 Proton

To check out Landau distribution for protons reproduced by the Geant4, we have made the thin layers of a silicon and lead, and have shot proton into the layers. The thin absorber region is generally taken to be $\kappa \ll 1$. In this region, the energy loss distribution obeys Landau distribution. We have took $\kappa = 0.01$ and have run the Geant4 simulator for various energy and have fitted the obtained histogram using ROOT to measure the most probable energy loss. In the ROOT, the histogram is fitted using CERNLIB routine ranlan(G110) for Landau distribution, which can be refered to "http://www.irb.hr/~cern/shortwrups_html3/node151.html". One of the results is shown in Figure 3.3. Then, we have compared the obtained most probable energy loss with that of theoretical value. The latter is calculated as follows [7],

$$\Delta_{mp} = \overline{\Delta}[\ln \frac{2m_e c^2 \beta^2 \overline{\Delta}}{(1-\beta^2)I^2} - \beta^2 + 0.198 - \delta], \tag{3.5}$$

where δ is the correction for the density effect. The comparison between Geant4 results and the theoretical prediction is collected in Table 3.5, 3.6 and Figure 3.4. The results shows that the Geant4 overestimates the most probable energy loss in both materails below 100 MeV. So far the cause of this difference is unknown. In the energy range from 500 MeV to 10 GeV, the Geant4 data are consistent with the theoretical values within $\leq 5\%$.

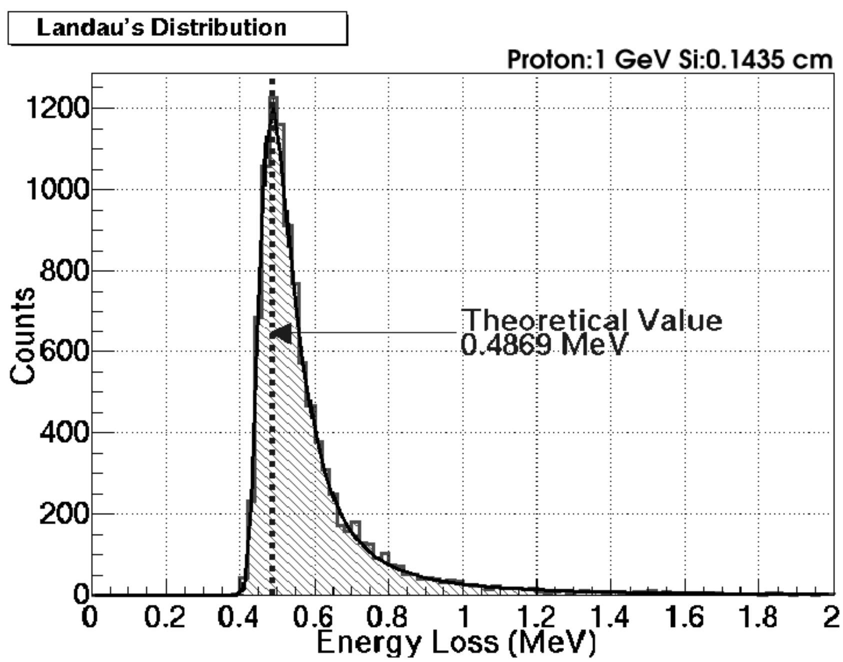

Figure 3.3: Deposit energy distribution of proton of 1 GeV in a silicon absorber. The absorber thickness is 0.144 cm which corresponds to $\kappa = 0.01$. The distribution obeys Landau distribution. The histogram is fitted by ROOT CERNLIB routine ranlan(G110) for Landau distribution.

Table 3.5: Validation of Landau distribution of protons in silicon.

particle energy	thickness (cm)	Δ_{mp} (Geant4)	Δ_{mp} (Theoretical Value)	difference between data and theo. [%]
10 MeV	2.58×10^{-5}	1.244 ± 0.007 keV	1.154 keV	+7.3
50 MeV	6.19×10^{-4}	10.16 ± 0.03 keV	9.448 keV	+7.0
100 MeV	2.36×10^{-3}	24.20 ± 0.06 keV	22.48 keV	+7.1
500 MeV	4.45×10^{-2}	184.2 ± 0.3 keV	179.5 keV	+2.6
1 GeV	1.44×10^{-1}	492.9 ± 0.7 keV	486.9 keV	+1.2
3 GeV	8.99×10^{-1}	3.003 ± 0.002 MeV	2.917 MeV	+2.9
10 GeV	7.68	28.79 ± 0.04 MeV	28.02 MeV	+2.7

Table 3.6: The same as Table 3.5, but for lead absorber.

particle energy	thickness (cm)	Δ_{mp} (Geant4)	Δ_{mp} (Theoretical Value)	difference between data and theo. [%]
10 MeV	6.67×10^{-6}	575.1 ± 3.7 eV	466.3 eV	+23
50 MeV	1.60×10^{-4}	6.435 ± 0.038 keV	5.939 keV	+8.4
100 MeV	6.11×10^{-4}	16.77 ± 0.06 keV	15.30 keV	+9.6
500 MeV	1.15×10^{-2}	141.3 ± 0.3 keV	136.1 keV	+3.8
1 GeV	3.71×10^{-2}	387.2 ± 0.7 keV	382.1 keV	+1.3
3 GeV	2.33×10^{-1}	2.474 ± 0.003 MeV	2.417 MeV	+2.4
10 GeV	1.97	25.73 ± 0.03 MeV	24.38 MeV	+5.5

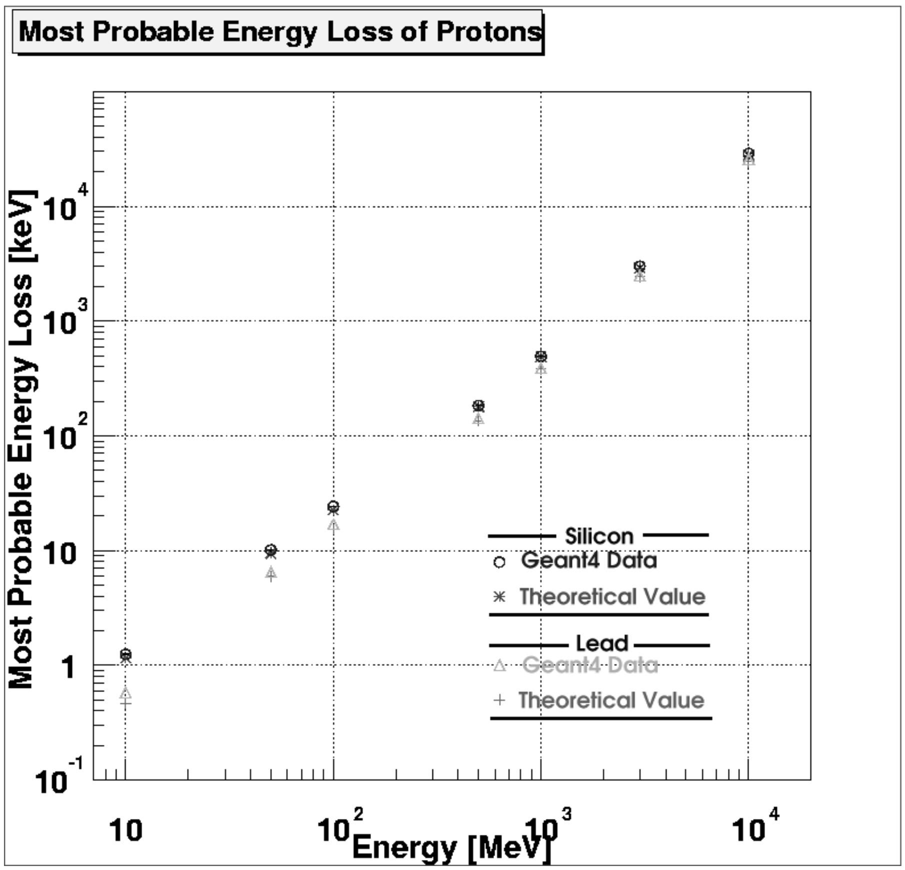

Figure 3.4: The most probable energy loss of protons. The absorbers are silicon and lead. The values of κ are 0.01 for all protons.

3.3.2 Electron

In the same way as the proton analysis of Landau distribution, we have constructed the thin silicon and the lead slab to validate the Landau distribution for electrons. Unlike the proton, high energy electrons frequently produce photons by bremsstrahlung. To check out Landau distribution for electrons, we have subtracted events where bremsstrahlung occured. We have also set the thickness of layers sufficiently small to meet the requirement for the Landau distribution and to reduce events of bremsstrahlung. In order to compare the Geant4 data with theoretical values, we have used the same theoretical formula as we did in the proton analysis except for the maximum allowable energy transfer, W_{max}. The maximum allowable energy transfer for electron becomes $W_{max} = T_e/2$ where T_e is the kinetic energy of the incident electron. The obtained results are shown in Table 3.7, 3.8 and Figure 3.5. Unlike the proton analysis the Geant4 data are consistent with the theoretical values quite well. In conclusion, the Geant4 simulator has precisely reproduced Landau distribution for electrons in the energy range from 10 MeV to 10 GeV.

Table 3.7: Validation of Landau distribution for electrons in the silicon. The κ is 0.0004 except for the last two data. In the Geant4 data, we exclude events where bremsstrahlung occured.

particle energy	thickness (cm)	Δ_{mp} (Geant4)	Δ_{mp} (Theoretical Value)	difference between data and theo. [%]
10 MeV	1.12×10^{-2}	28.37 ± 0.6 keV	28.30 keV	+0.2
50 MeV	5.61×10^{-2}	163.2 ± 0.3 keV	162.9 keV	+0.2
100 MeV	1.12×10^{-1}	342.3 ± 0.5 keV	341.2 keV	+0.3
500 MeV	5.61×10^{-1}	1.878 ± 0.003 MeV	1.869 MeV	+0.5
1 GeV	1.00	3.503 ± 0.020 MeV	3.435 MeV	+2.0
($\kappa = 4 \times 10^{-5}$)5 GeV	5.61×10^{-1}	1.880 ± 0.003 MeV	1.869 MeV	+0.6
($\kappa = 4 \times 10^{-6}$)10 GeV	1.12×10^{-1}	339.3 ± 0.5 keV	341.7 keV	-0.7

Table 3.8: Validation of Landau distribution for electron in the lead. Here, $\kappa = 0.0001$ except for the last two energies. Events including bremsstrahlung are excluded in the Geant4 data.

particle energy	thickness (cm)	Δ_{mp} (Geant4)	Δ_{mp} (Theoretical Value)	difference between data and theo. [%]
10 MeV	7.24×10^{-4}	4.985 ± 0.034 keV	5.166 keV	-3.5
50 MeV	3.63×10^{-3}	32.65 ± 0.10 keV	32.52 keV	+0.4
100 MeV	7.25×10^{-3}	69.95 ± 0.17 keV	69.86 keV	+0.1
500 MeV	3.63×10^{-2}	389.1 ± 1.0 keV	397.0 keV	-2.0
1 GeV	7.25×10^{-2}	822.0 ± 3.1 keV	830.6 keV	-1.0
($\kappa = 1 \times 10^{-5}$)5 GeV	3.63×10^{-2}	391.3 ± 1.2 keV	398.2 keV	-1.7
($\kappa = 1 \times 10^{-6}$)10 GeV	7.25×10^{-3}	68.15 ± 0.19 keV	71.60 keV	-4.8

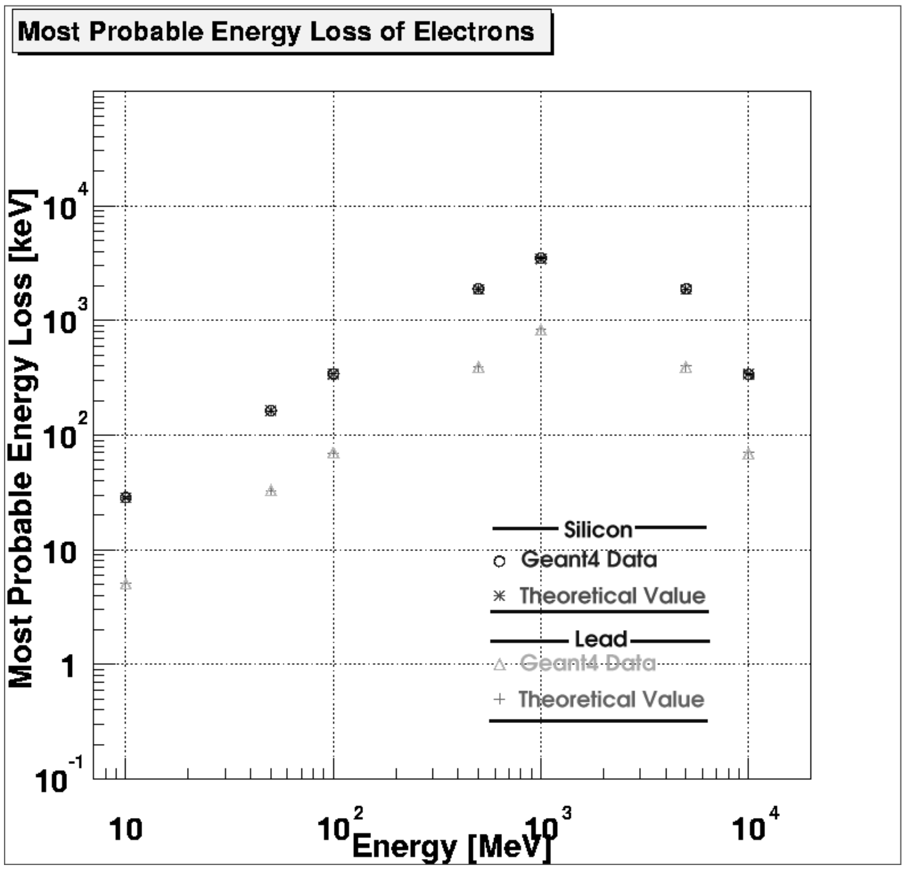

Figure 3.5: The same as Figure 3.4 but for electrons. The values of κ are 0.0004 and 0.0001 for silicon and lead, respectively. Above 5 GeV electrons, we applied different κ. See Table 3.7 and 3.8

3.4 Proton Range

In this section we have investigated whether the Geant4 simulator reproduced the proton range correctly or not. In the Geant4 simulation, our absorber is large enough for protons to deposit their whole energy in the material. The size of the absorber is $1000X_0 \times 1000X_0 \times 1000X_0$, and the species of the material are tungsten, lead, and CsI, as shown in Figure 3.6. Here, "X_0" stands for a radiation length, the mean distance over which high-energy electrons lose 1/e of their energy due to bremsstrahlung only. These values are collected in Table 3.9 [8]. The injected paricle energies are 200 MeV and 1 GeV. We have compared the Geant4 results with the theoretical vaules calculated by "PSTAR program". This program calculates the stopping power and range tables for protons in various materials and can be refered to "http://physics.nist.gov/PhysRefData/Star/Text/PSTAR.html". When the range is calculated in the program, it is assumed that the energy loss is continuous. Therefore, we have removed events which included the inelastic scattering in the Geant4 simulation. The cut values we applied are 0.4 mm for electrons and 0.1 mm for other particles. We have shot 10k protons and have made histograms of the particle track length, which are collected in Figure 3.7. The peak of the histograms corresponds to the mean range determined by the simulation. The comparisons with the theoretical prediction are shown in Table 3.9 and Figure 3.8. In Figure 3.8 the results are shown in units of cm to make the difference in the materials easily viewable. We have found that the mean proton ranges of the Geant4 are well consitent with those of theoretical calculation within $\leq 0.6\%$.

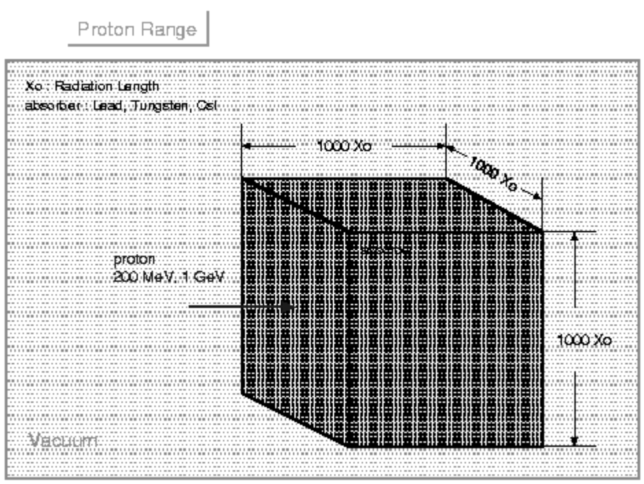

Figure 3.6: The geometry of the absorber used for proton range validation.

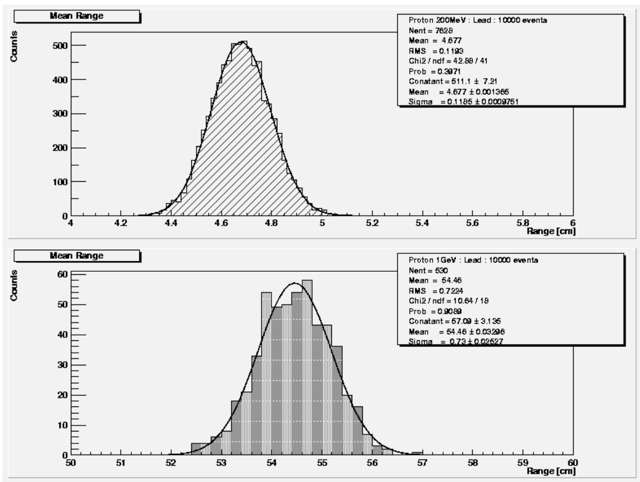

(a) lead

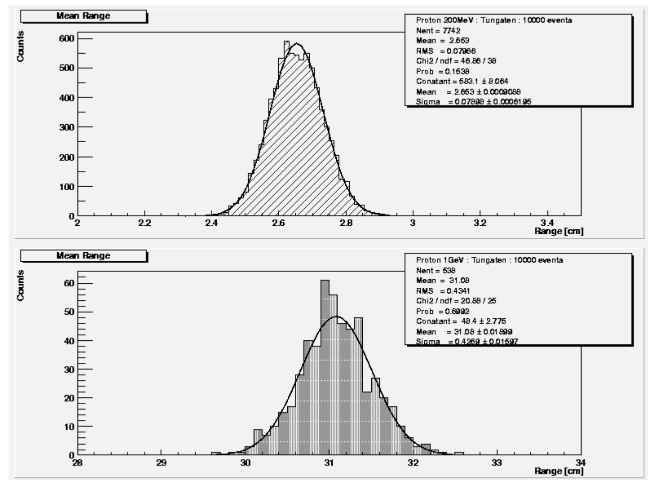

(b) tungsten

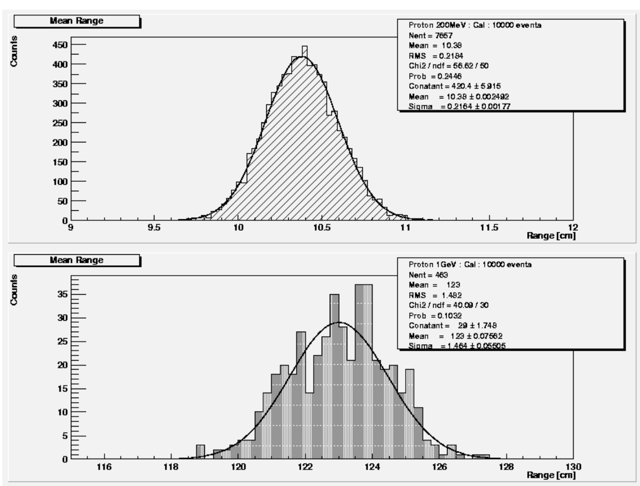

(a) CsI

Figure 3.7: The histograms of the track length of protons. The absorbers are lead, tungsten, and CsI. The histograms are for 200 MeV protons (top) and 1 GeV protons (bottom) in each plot.

Table 3.9: The results of the Geant4 simulation for the mean range of protons.

Material	$X_0[cm]$	Particle energy	Geant4 [g/cm^2]	Theo. [g/cm^2]	difference* [%]
Lead	0.56	200 MeV	53.08 ± 0.01	53.12	-0.08
		1 GeV	618.1 ± 0.3	621.7	-0.6
Tungsten	0.35	200 MeV	51.20 ± 0.02	51.17	+0.06
		1 GeV	599.8 ± 0.4	602.0	-0.4
CsI	1.85	200 MeV	47.02 ± 0.01	46.97	+0.1
		1 GeV	557.2 ± 0.5	557.0	+0.04

$*difference = \frac{(G4data-PSTAR)}{PSTAR} \times 100$

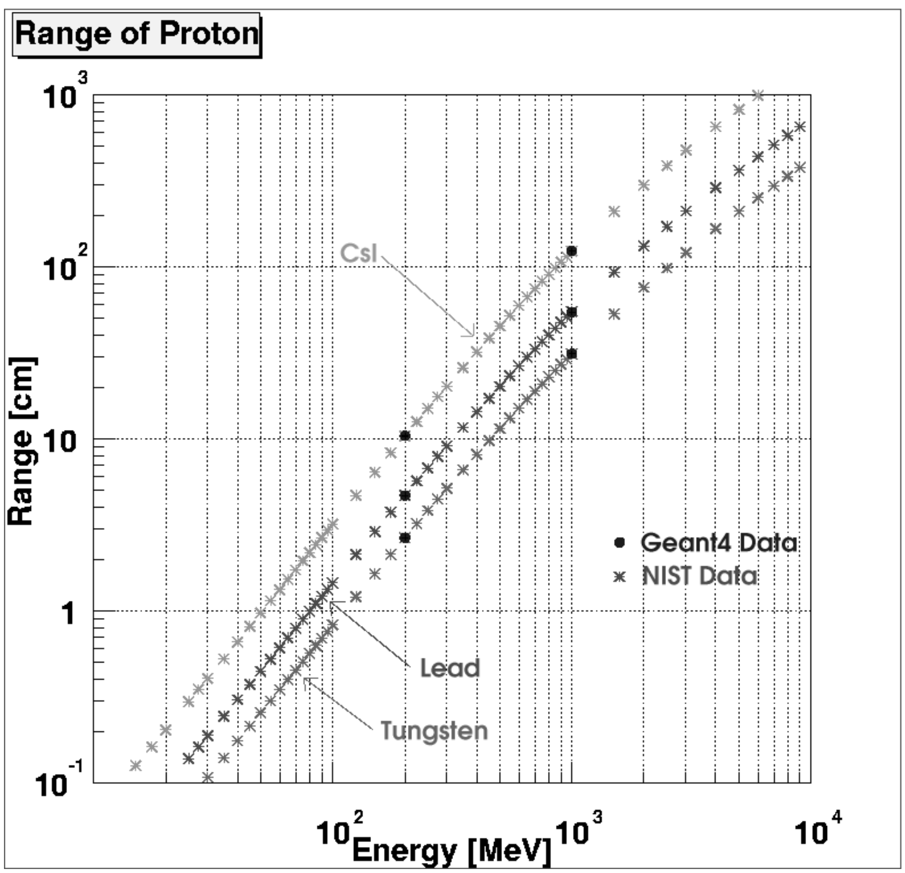

Figure 3.8: The results of the Geant4 simulation for the range of 200 MeV and 1 GeV protons. The absorbers are CsI, lead and tungsten. Stars and filled circles represent the NIST data and the Geant4 results, respectively. All data are shown in units of cm.

3.5 Conclusions

In this chapter we have investigated the ionization loss of charged particles. The energy loss distribution due to the ionization of charged particles varies depending on the absorber thickness. In thick absorbers it becomes Gaussian in form and in thin absorbers it distributes in Landau distribution. First, to investigate the stopping power, dE/dx due to the ionization of the Geant4 we have shot protons from 10 MeV to 10 GeV into thick silicon and lead. Those materials are used in the GLAST satellite. Then we have compared the obtained results with the theoretical Bethe-Bloch formula and have found that the obtained results coincided with that of theoretical values. We have also validated the energy loss distribution in thin materials. To do this, we have examined the most probable energy loss of Landau distribution by shooting electrons and protons from 10 MeV to 10 GeV into the same kinds of materials, but thin ones. As a result it has been found that the Geant4 results were well consistent with theoretical values for electrons, and for protons except for low energy; the Geant4 result of 10 MeV protons in a lead was 23% larger than theoretical one. The cause of the discrepancy is unknown. However, the thickness of lead converters of GLAST (0.2 mm) is sufficiently large for 10 MeV protons and energy deposit distribution becomes Gaussian in form. Therefore this can not cause the serious problem for the GLAST simulation. We have also checked the protons range in lead and it has been found that the Geant4 reproduced the theoretical values quite well. In consequence, we have concluded that the ionization representation of the Geant4 is sufficiently accurate for the GLAST simulation.

Chapter 4

Validation of Electromagnetic Shower Profile

The primary interation of gamma-ray with matter in the GLAST energy range is the pair production. The incident gamma-rays convert to e^+/e^- pairs in the conversion foils in the tracker. After a conversion, their trajectories are measured by the particle tracking detectors (Silicon Strip Detectors) and the direction of the incident gamma-ray is determined via the reconstraction. The energy of incident gamma-ray is measured in the Calorimeter where pair-created e^+/e^- deposit energy through the process of electromagnetic shower. These techniques is illustrated in Figure 4.1. Thus, it is important to precisely reproduce the electromagnetic shower, espectially pair production, in the GLAST simulation.

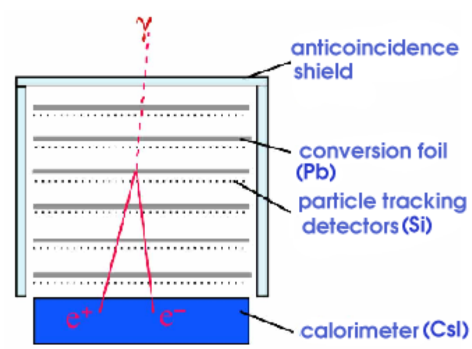

Figure 4.1: Principle of a pair conversion telescope.

In section 4.1 we check out the property of longitudinal and lateral shower profiles of the Geant4. Since there are only a few experiments of electromagnetic shower, we compare the shower profile of the Geant4 with that of the EGS4 simulation [9], as well as the real experimental data. The EGS4 program has been used for a long time in the particle physics field and is reliable simulation tool as for the electromagnetic process. First, we compared the Geant4 data with an experment, i.e., “1 GeV Electron-induced Cascade Shower in Water”, hereafter called “Crannel experiment”, performed by Carol Jo Crannell et al at SLAC in 1969 [10]. We have reproduced this experiment in the Geant4 simulation and have compared the results with the experimental data and the EGS4 simulation. Next, in order to examine the electromagnetic shower profile in a condition closer to GLAST, we have compared how the electromagnetic shower develops in materials used in GLAST satellite between the Geant4 and the EGS4. The comparison for the CsI scintillator, used for the Calorimeter, is described in section 4.1.2. The other results for lead and tungsten are given in Appendix A. Lead will be used as conversion foils in the Tracker and tungsten is another candidate of conversion foils. To see the shower development in the Tracker, we have also constructed the simplified geometry of the Tracker where 10 lead layers and 9 air layers are placed alternately and have examined the shower profiles.

The Italian GLAST-LAT team has found a bug in the pair creation routine of Geant4 2.0 (265th line in the code, G4GammaConversion.cc). The energy sharing between e^+ and e^- was not acturately reproduced in the default Geant4 2.0. This bug should be modified as below,

```
{ epsil = 0.5 - epsilrange*pow(G4UniformRand(), 1/3) ;    (before bug fixed)
{ epsil = 0.5 - epsilrange*pow(G4UniformRand(), 0.3333) ; (after bug fixed)
```

Note that the bug is fixed in the Geant4 4.0. We have also modified it before the validation of the Geant4 in Chapter 4 and Chapter 5.

4.1 Electron-induced Shower Profile in Water

We have reproduced the experiment of "1 GeV Electron-induced Cascade Shower in Water" in the Geant4 simulation and have compared the results with the experimental data and the results of the EGS4 simulation. This is the best experiment to validate the EGS4 and the Geant4 shower profiles because it is highly accurate. As for electron below 1 GeV, there is no reliable experiment.

In the experiment, the water target consists of a steel tank containing 8000 liters of distilled water. The movable detector assembly was mounted on track above the tank, as shown in Figure 4.2. The dimension of target is $122 \times 122 \times 460$ cm^3. The entire detector assembly and the probe could be operated remotely. The probe consists of photomultiplier tube optically coupled to a detector of anthracene and polished aluminum light guide. Then, the three-dimensional distribution of energy deposition was measured by the probe. Due to the inherent limitations of the experimental equipment, the uncertainties in the data are $\pm 3\%$ in energy deposition of each part of rings.

The EGS4 simulation has been performed by Prof. W. Ralph Nelson (SLAC) and the Geant4 simulation by ourselves. In both simulations, we have reproduced the geometry corresponding to the experiment. The geometry is a simple cylinder which has 12 layers longitudinaly. There are 2 types of layer. The thickness of the first 4 layers are 20 cm and others are 40 cm. Each layer has 11 rings of 3 types. Three innermost rings have the width of 1 cm, five outermost ones of 4 cm, and others of 2 cm. The schematic geometry used in the simulations is shown in Figure 4.3. The incident particle is electron of 1 GeV. The numbers of particle we shot are 10k and 2.5M for the Geant4 and EGS4 simulation, respectively. The cutoff energy we applied in the simulation is summarized in Table 4.1.

The results for the longitudinal and lateral distribution of energy deposition are shown in Figure 4.4. The energy deposition in each area has been normalized so that the integration toward the horizontal axis becomes unity. The plots show that the Geant4 and EGS4 have reproduced the real experimental data well, except for the discrepancy of the Geant4 in the lateral profile. The differences in lateral profiles between the Geant4 and experiment, and between the Geant4 and EGS4 are summarized in Figure 4.5. This plots indicates that the

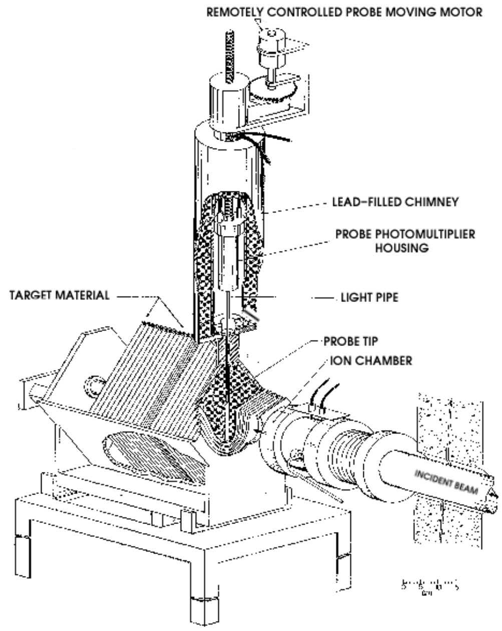

Figure 4.2: Schematic view of the equipment used in the Crannell experiment.

energy depositions in innermost rings of the Geant4 were larger than those of the EGS4 ($< +53\%$) and experimental data ($< +42\%$). On the other hand, far from the center they becomes smaller than those of the EGS4 ($< |-34\%|$) and experimental data ($< |-56\%|$). Futhermore, the dependence of the discrepancy on the depth of layer can be seen although the cause of it is unknown. Then, we have calculated the mean energy leakage from the absorber, and have tabulated the results in Table 4.2. There is no remarkable difference in the mean energy leakage. These results indicate that the growth of electromagnetic shower of the Geant4 is slightly narrower than those of the EGS4 and experiment. As a next step, we examine whether this tendency can be seen in the material used in the GLAST satellite.

Table 4.1: Cut off energy of the Geant4 and EGS4 simulation in total energy. Cut off energies of electron and other particles in the Geant4 corresponds to cut off length of 0.04 mm and 0.01 mm, respectively.

Material	Geant4		EGS4	
	Electron	Photon	Electron	Photon
Water	524 keV	0.99 keV	611 keV	100 keV

Table 4.2: Mean energy leakage

Mean Energy Leakage		
Geant4	EGS4	Experiment
4.87%	4.86%	4.56%

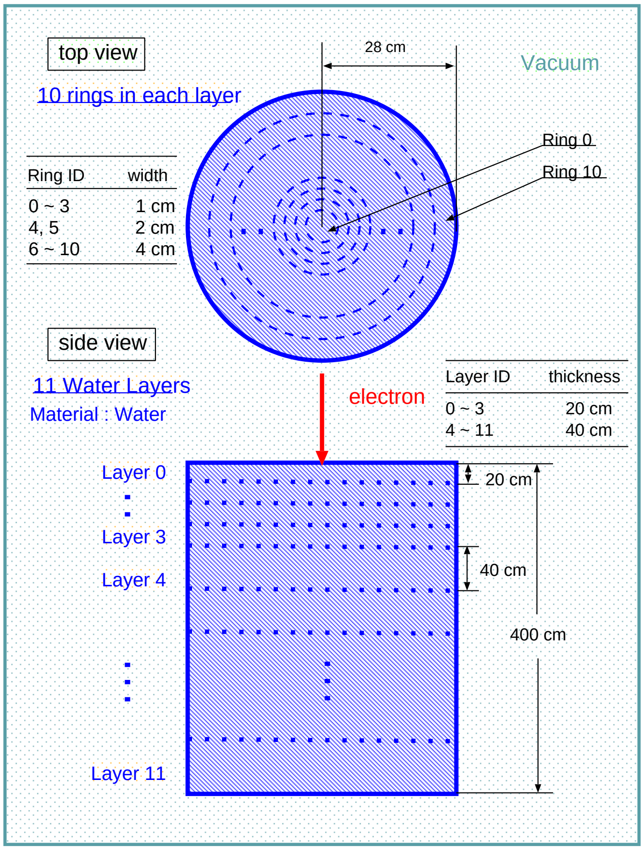

Figure 4.3: The geometry for the simulation of the Crannell experiment. The absorber is water of a simple cylinder, whose radius is 28 cm and height is 400 cm. The cylinder is composed of 12 layers, and each layer has 11 rings.

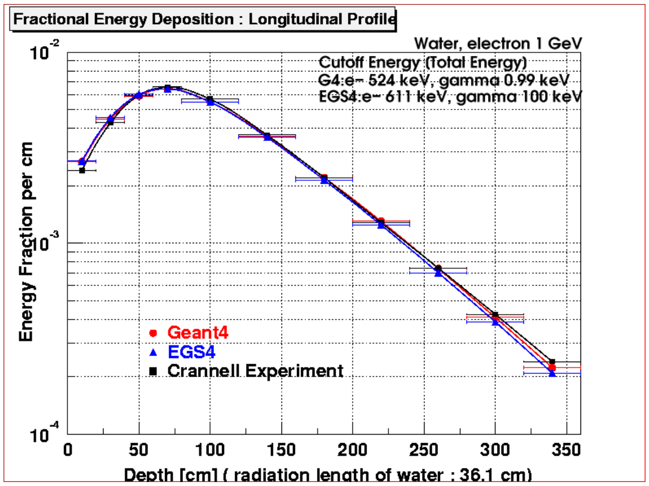

(a) longitudinal shower profile

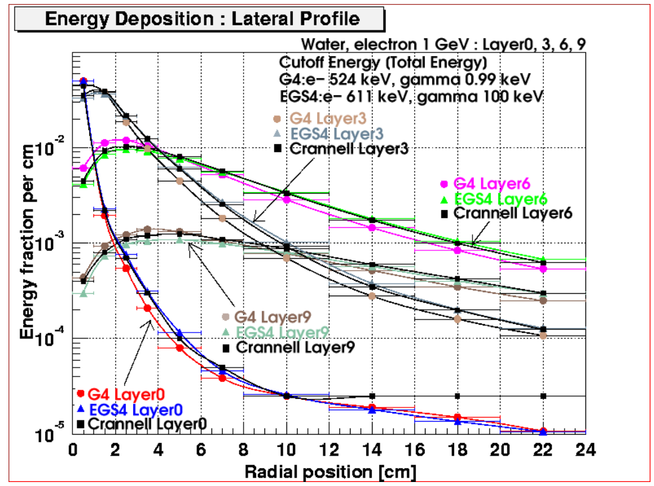

(b) lateral shower profile in layer 0, 3, 6, and 9.

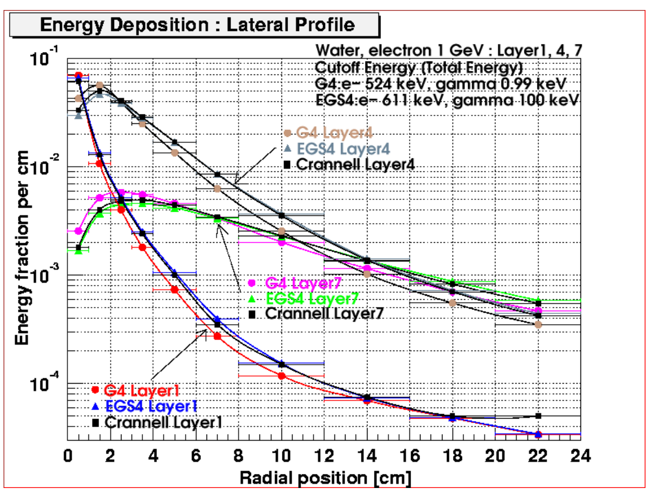

(c) lateral shower profile in layer 1, 4, and 7.

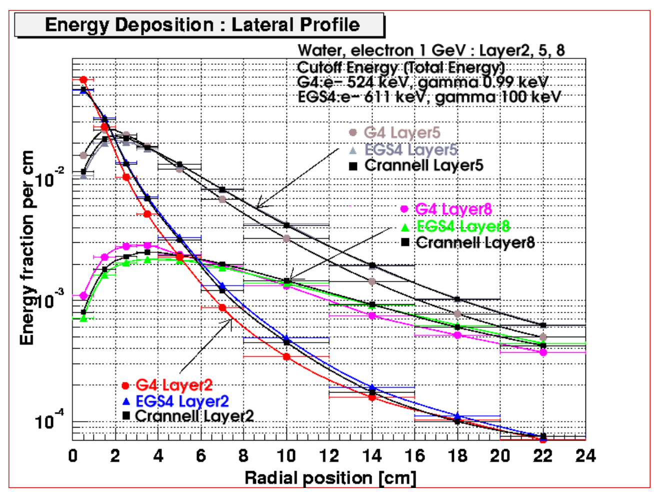

(d) lateral shower profile in layer 2, 5, and 8.

Figure 4.4: Comparison of Geant4 and EGS4 results with the Crannell experiment (water absorber). The panel (a) shows the longitudinal shower profile, and (b), (c), and (d) are lateral shower profile

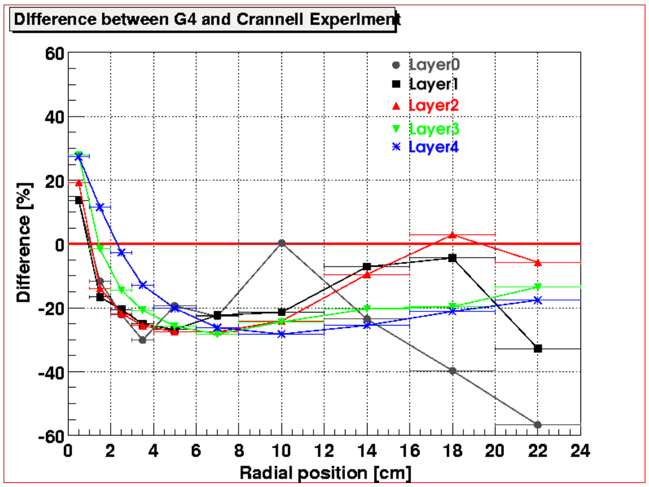

(a) Layer 0 - 4
(Geant4 and Crannell experiment)

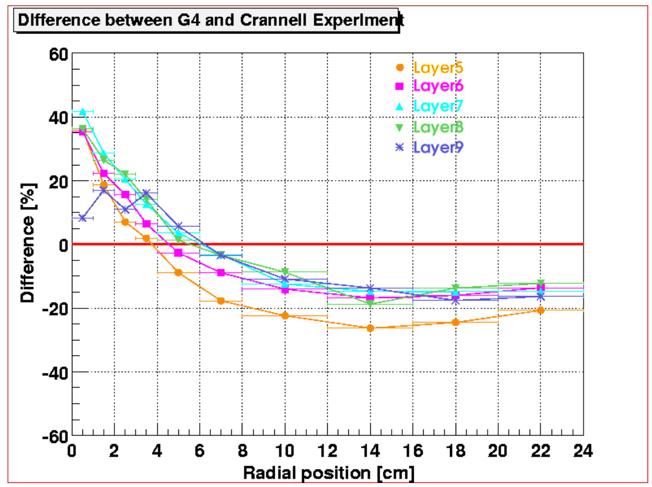

(b) Layer 5 - 9
(Geant4 and Crannell experiment)

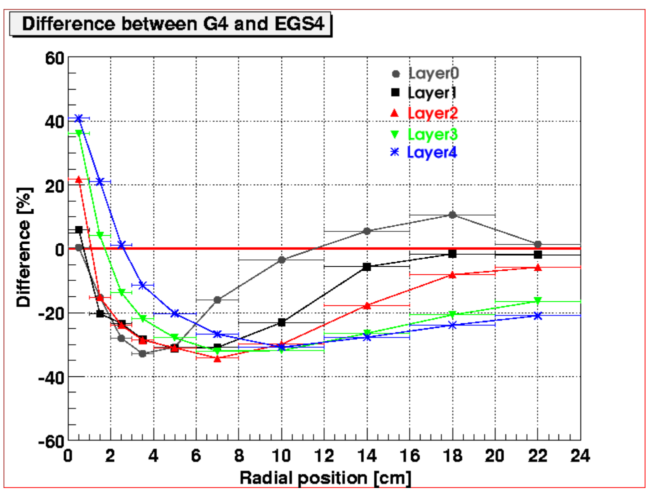

(c) Layer 0 - 4 (Geant4 and EGS4)

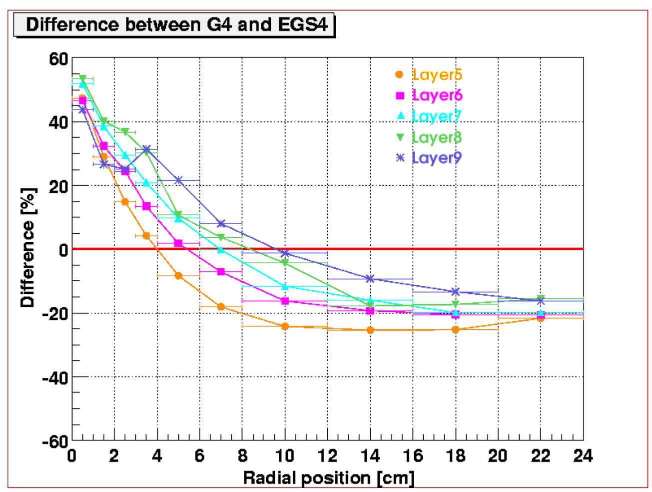

(d) Layer 0 - 9 (Geant4 and EGS4)

Figure 4.5: The difference (simulation - Crannell exp.) in the energy depositions in lateral position of the absorber (water). The panel (a) and (b) show the difference between the Geant4 and the Crannell experiment, and other plots show the difference between the Geant4 and the EGS4.

4.2 Shower Profile in CsI

We have checked out the development of the electromagnetic shower in the materials used in the GLAST satellite. The absorbers are CsI, lead and tungsten. We discuss the result of CsI, used in a Calorimeter, here. The other results are summarized in Appendix A. The geometry is a simple cylinder of homogeneous material. In the simulation, we have constructed a cylinder which is replicated longitudinaly (slice) and radialy (ring). The cylinder is composed of 20 slices. The thickness of each slice is 1 radiation length and each slice is composed of 20 rings. The width of each ring is 0.2 Moliere radius, R_M. The Moliere radius of CsI is 3.8 cm, which is refered to "Particle Physics Booklet" [8]. The lateral shower development in different materials is known to scale with the Moliere radius. On the average, only 10% of the energy escapes from the cylinder with radius R_M. About 99% is contained inside of $3.5R_M$. The schematic geometry is shown in Figure 4.6. In total, the height of cylinder is 20 radiation lengths and the cylinder radius is 4 Moliere radius.

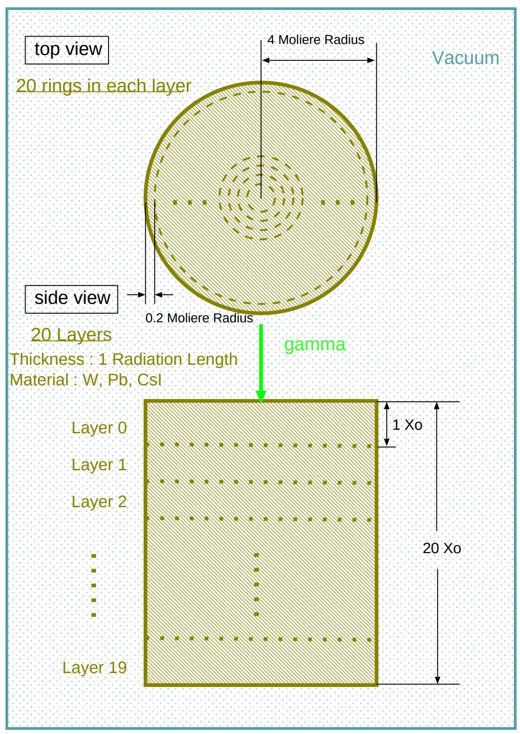

Figure 4.6: The geometry for the simulation of the electromagnetic cascades. The absorber is a simple cylinder. The thickness of each layer is 1 radiation length and the width of each ring is 0.2 Moliere radius.

We have shot 20 MeV, 50 MeV, 100 MeV, 500 MeV, 1 GeV, 5 GeV, 10 GeV, and 100 GeV gamma-rays into various absorbers along the center line of the cylinder. The numbers of the particle we shot are summarized in Table 4.3. The cut values used in the Geant4 and EGS4 simulator are also shown in Table 4.3. These cut off energies for the Geant4 correspond to cut off length of 0.04 mm and 0.01 mm for electrons and photons, respectively.

Longitudinal Profiles In the longitudinal profiles we have taken an average energy deposited in each layer. Then we have normalized them by initial kinetic energy of the injected gamma-

Table 4.3: Parameters we used in the simulation.

Number of Gamma-rays

20 MeV, 50 MeV	100 MeV, 500 MeV, 1 GeV, 5 GeV	10 GeV, 100 GeV
10k	1k	100 (EGS4 1k)

Cut Value

	Geant4		EGS4	
	Electron	Photon	Electron	Photon
CsI	530 keV	2.24 keV	1.5 MeV	100 keV

rays and have made the histogram of the fractional energy deposit as a function of the depth, t, in the material. We have also run the EGS4 simulation in the same configuration. The results are displayed in Figure 4.7. The plots show that the Geant4 results are consistent with the EGS4 results quite well, except for the small discrepancy ($< +4.8\%$) around the peak of the longitudinal profiles. Then we have calculated the mean energy leakage from the absorber, as shown in Table 4.4. There is no remarkable difference between the energy leakages of the Geant4 and EGS4. The longitudinal profiles in a lead and a tungsten also show the similar results, as shown in Table A.1 and Figure A.1.

Table 4.4: Mean energy leakage

Gamma-ray energy	Mean Energy Leakage	
	Geant4 [%]	EGS4 [%]
20 MeV	2.4	2.6
50 MeV	2.3	2.4
100 MeV	2.0	2.3
500 MeV	1.9	2.1
1 GeV	2.0	2.3
5 GeV	2.7	2.9
10 GeV	2.9	3.5
100 GeV	5.4	6.6

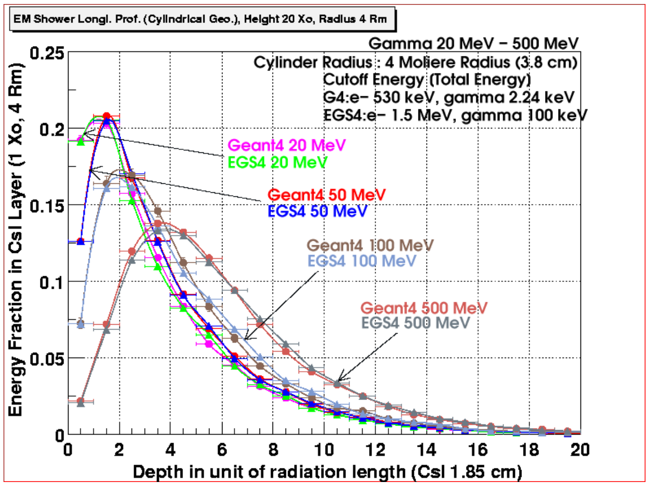

(e) From 20 MeV to 500 MeV for CsI

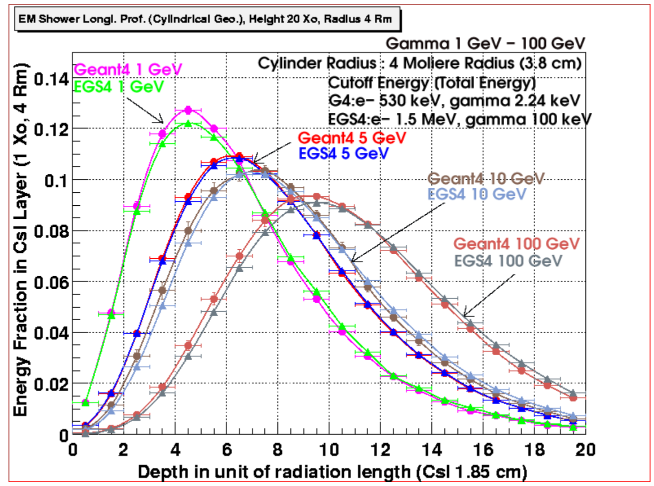

(f) From 1 GeV to 100 GeV for CsI

Figure 4.7: The longitudinal profiles of fractional deposit energy in the gamma-ray-induced cascades for the Geant4 and EGS4. The absorber is CsI. Filled circles indicate the Geant4 data, and filled triangles are the EGS4 data.

Lateral Profiles To confirm whether the Geant4 simulator correctly reproduces the transverse growth of the electromagnetic cascades, we have measured the energy deposition distribution within each layer. The plots of Figure 4.8 and 4.9 show the transverse distribution of the energy deposition. The difference of the energy deposition between the Geant4 and EGS4 are shown in Figure 4.10 and 4.11. Figure 4.10 indicates that the energy deposition near the center of the cylinder of the Geant4 is always larger than that of the EGS4 and becomes smaller than that of the EGS4 at outer radii, like the lateral profile in the simulation for Crannell experiment in section 4.1.1. These results also indicates that the lateral shower development of the Geant4 is slightly narrower than the EGS4. In the shower profiles in lead and tungsten, shown from Figure A.2 to Figure A.5, the same features can be recognized. Except for this slight difference, the Genat4 has reproduced the EGS4 results well.

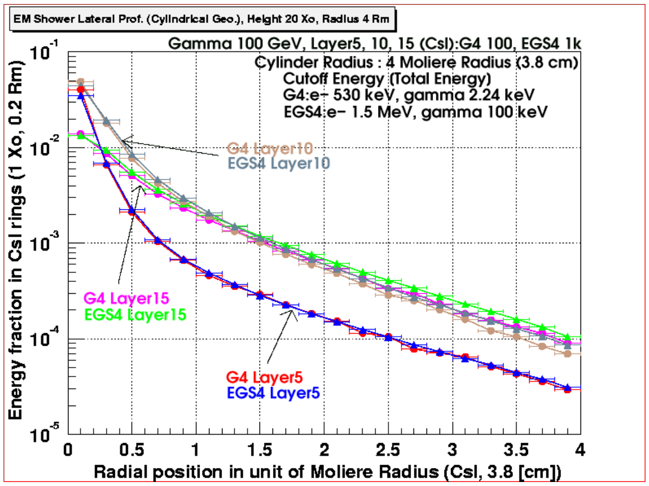

(a) 100 GeV gamma, CsI

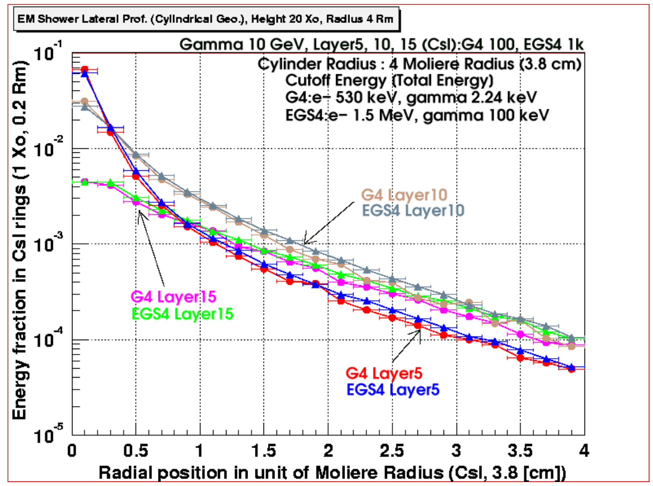

(b) 10 GeV gamma, CsI

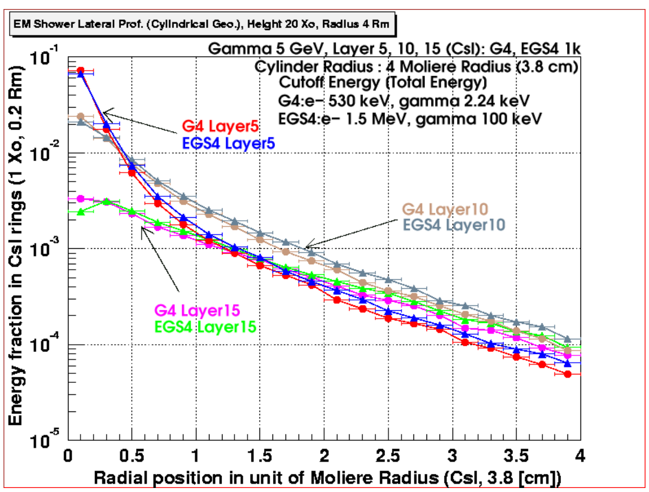

(c) 5 GeV gamma, CsI

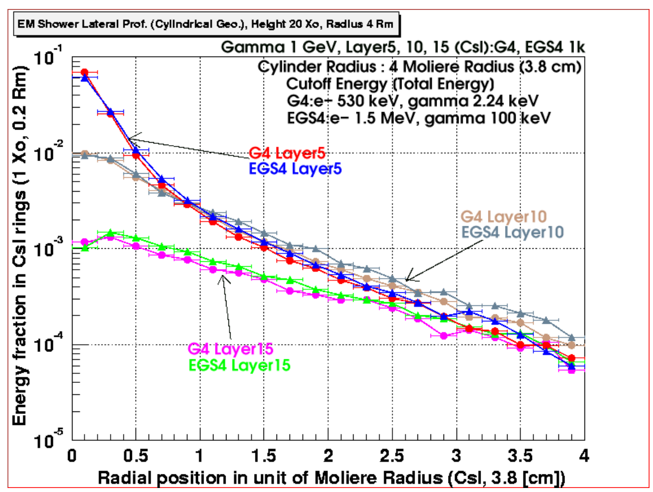

(d) 1 GeV gamma, CsI

Figure 4.8: The Geant4 and the EGS4 lateral profile of the gamma-induced cascades. The absorbers are CsI. The energies of gamma-rays are 100 GeV, 10 GeV, 5 GeV, and 1 GeV. Filled circles indicate the Geant4 data, and filled triangles are the EGS4.

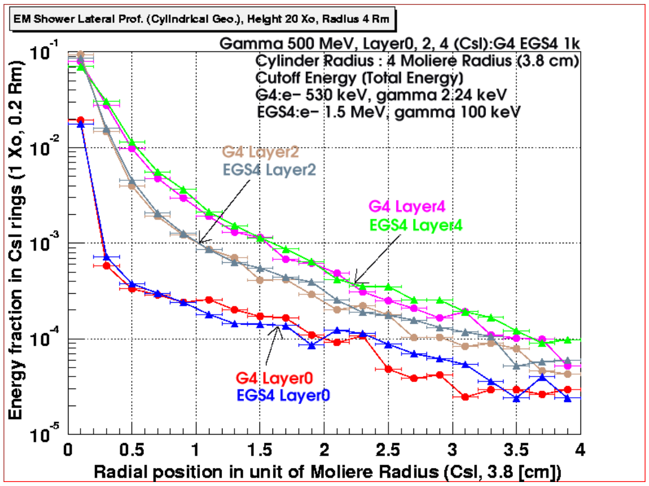

(e) 500 MeV gamma, CsI

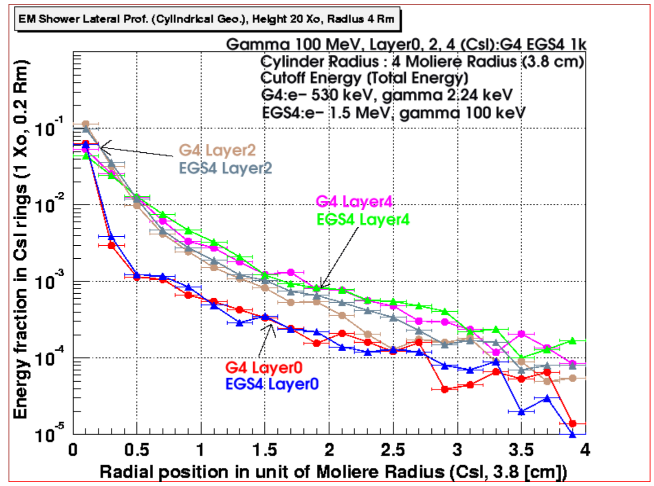

(f) 100 MeV gamma, CsI

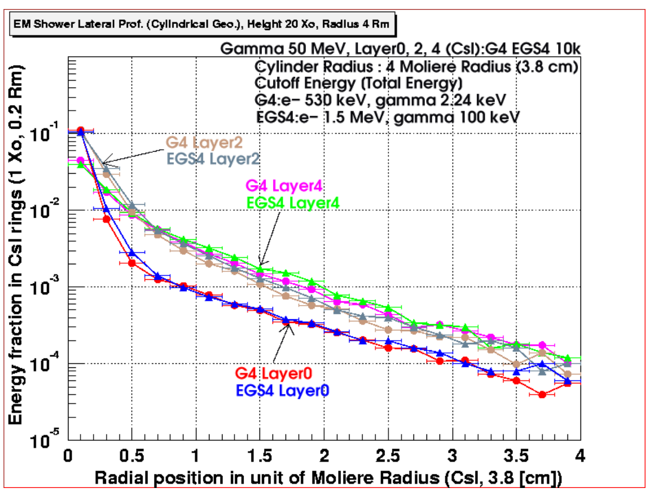

(g) 50 MeV gamma, CsI

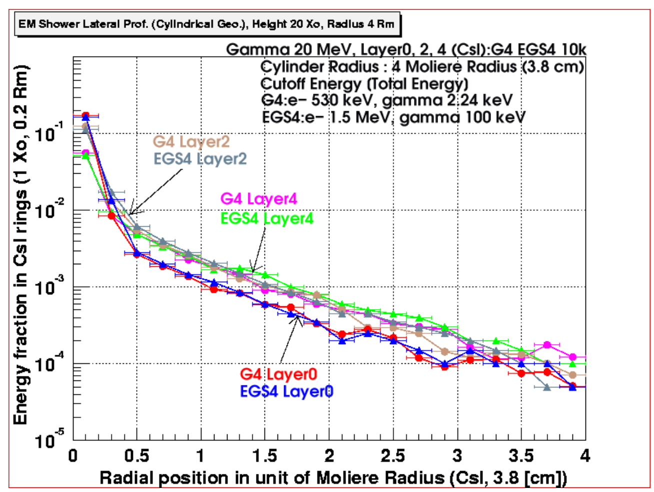

(h) 20 MeV gamma, CsI

Figure 4.9: Same as Figure 4.8, but for the lateral profiles in layer 0, 2, and 4 of 500 MeV, 100 MeV ,50 MeV, and 20 MeV gamma-rays.

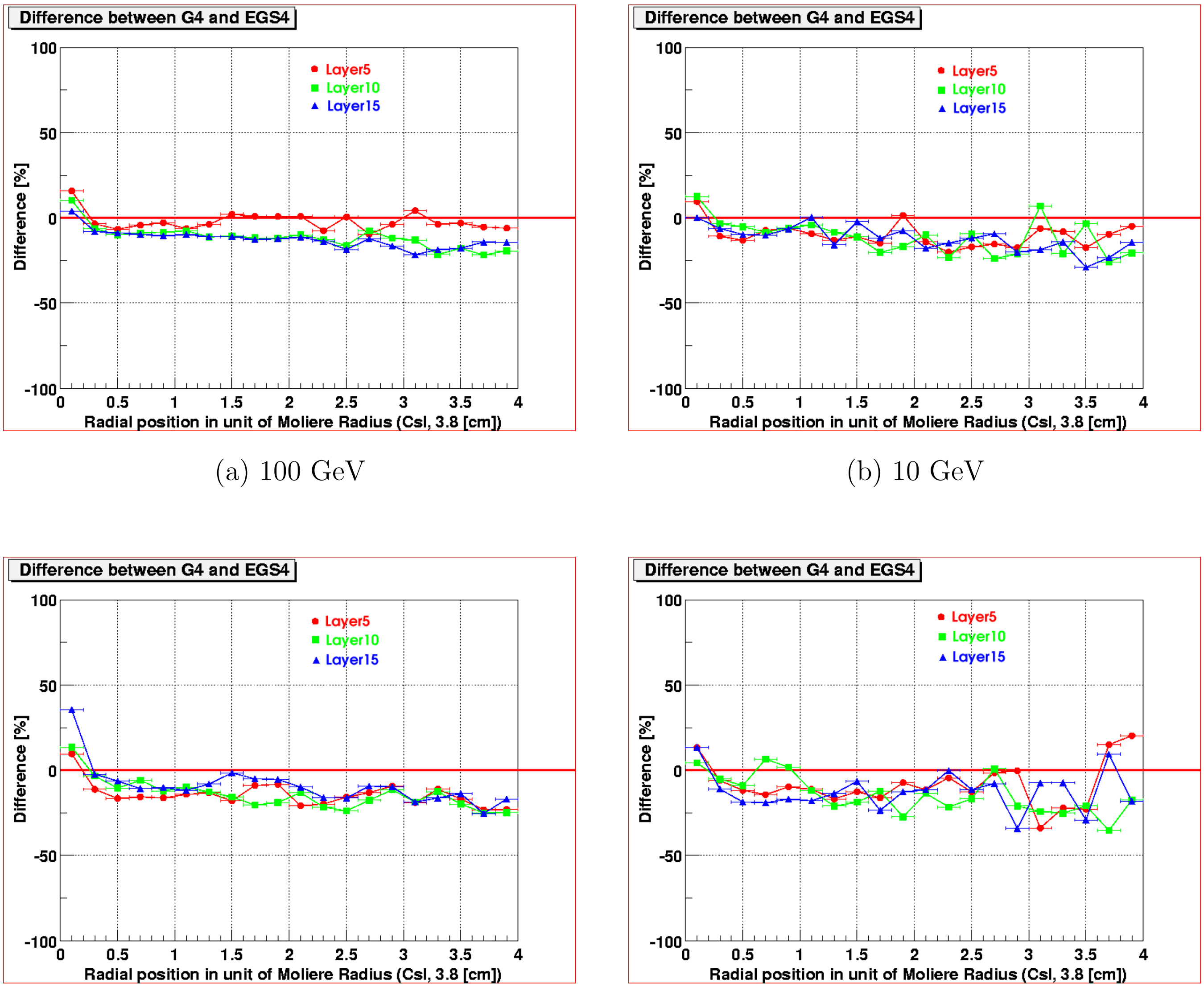

(a) 100 GeV

(b) 10 GeV

(c) 5 GeV

(d) 1 GeV

Figure 4.10: The difference (Geant4 - EGS4) in the energy depositions in lateral position of the absorber (CsI). The results from 100 GeV to 1 GeV are summarized here.

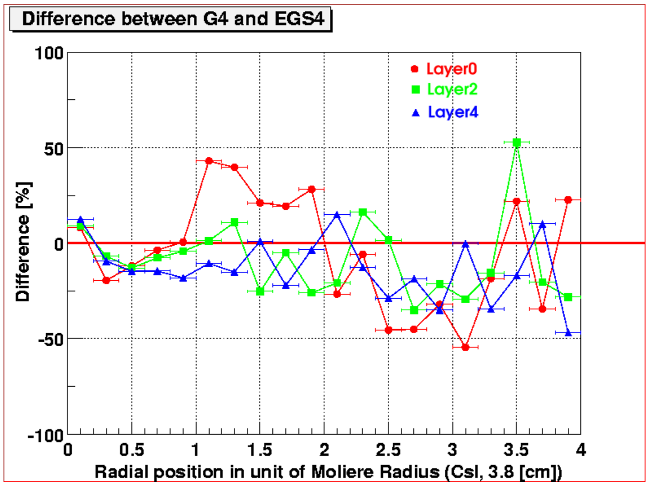

(e) 500 MeV

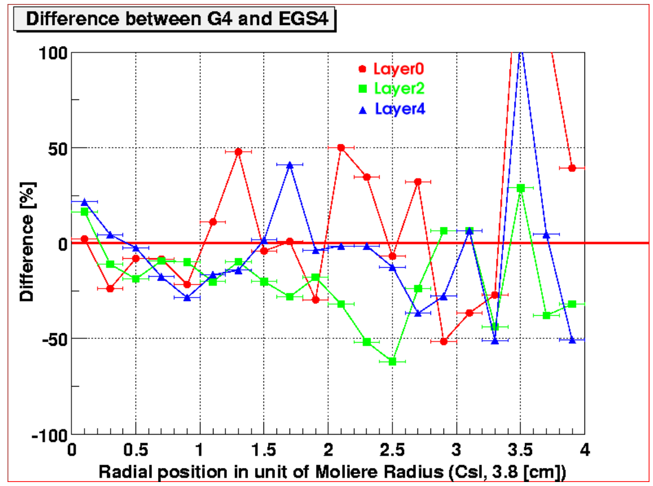

(f) 100 MeV

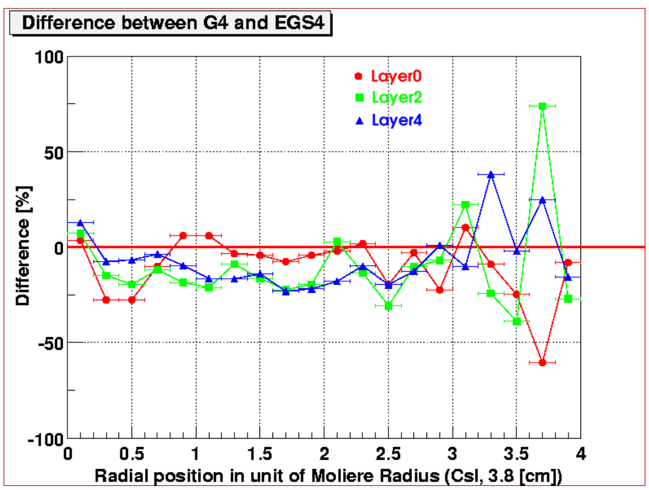

(g) 50 MeV

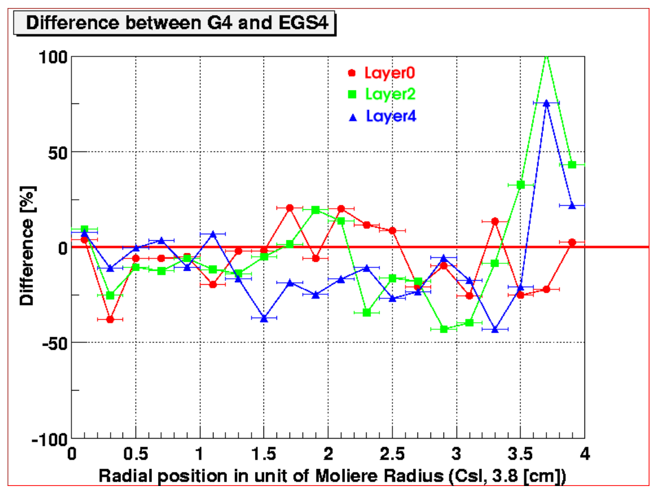

(h) 20 MeV

Figure 4.11: Same as Figure 4.11, but for the results from 500 MeV to 20 MeV.

4.3 Shower Profile in 10 Lead Layers

The shower development in trays in the Tracker of GLAST satellite is expected to spread widely than in the homogeneous geometry because there is a space of about 3 cm between each tray. We have thus investigated the shower profile in the approximated geometry of the Tracker. In the simulation we have constructed the geometry as shown in Figure 4.12. The geometry is a cylinder which is composed of the 10 lead and 9 air layers placed alternately. Total thickness of lead is 1.0 radiation length, almost the same as that of GLAST-LAT.

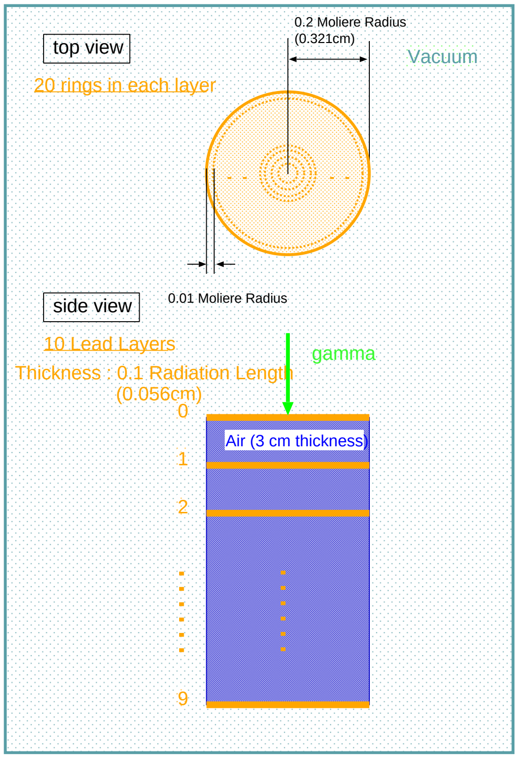

Figure 4.12: Approximated geometry of the trays in the Tracker. The cylinder radius is 0.2 Moliere radius.

We have shot gamma-rays of 20 MeV, 50 MeV, 100 MeV, 500 MeV, 1 GeV and 5 GeV. The results are collected from Figure 4.13 to 4.18. As a result, we can see the difference (10% − 20%) between the Geant4 results and the EGS4 results in all longitudinal profiles. This discrepancy is found to increase as the energy of incident gamma-ray decreases, and is the largest at 20 MeV gamma-ray ($\sim$ 20%). The difference in the lateral profile is shown in Figure 4.19. The plots show the dependence of discrepancy on the energy of incident gamma-ray. At 20 MeV, the energy depositions of Geant4 are larger than those of the EGS4 in innermost rigion and they become smaller at the middle of the radius. Then, they exceed the energy deposition of the EGS4 again toward the outer rings. As the energy of the incident gamma-ray increases, the energy deposition of Geant4 becomes larger than that of the EGS4 at every rings. The cause of these behavior is unknown. Figure 4.19 also show that the Geant4 shower development is narrower than that of the EGS4, like the shower profiles in the homogeneous material in section 4.1.2. Table 4.5 is the mean energy leakage from the absorber, which shows that at lower energy the mean energy leakage of the Geant4 are slightly smaller than that of the EGS4 ($\sim$ 0.3% at 20 MeV). This may be attributed to the narrower shower development of the Geant4.

Table 4.5: Mean energy leakage

	Mean Energy Leakage	
Gamma energy	Geant4 [%]	EGS4 [%]
20 MeV	97.756	98.065
50 MeV	98.622	98.750
100 MeV	98.907	98.978
500 MeV	99.398	99.432
1 GeV	99.585	99.611
5 GeV	99.878	99.878

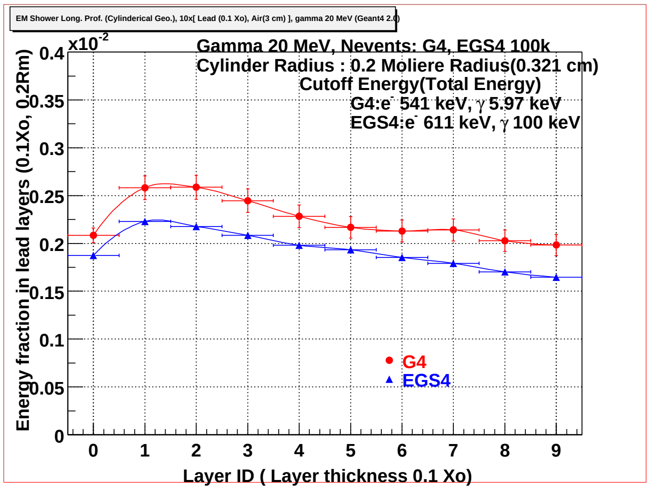

(a) 20 MeV Gamma, Longitudinal

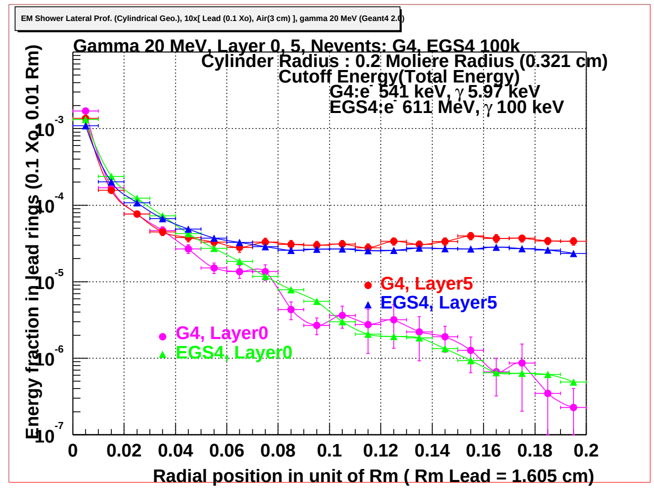

(b) 20 MeV Gamma, Lateral, Layer0, 5

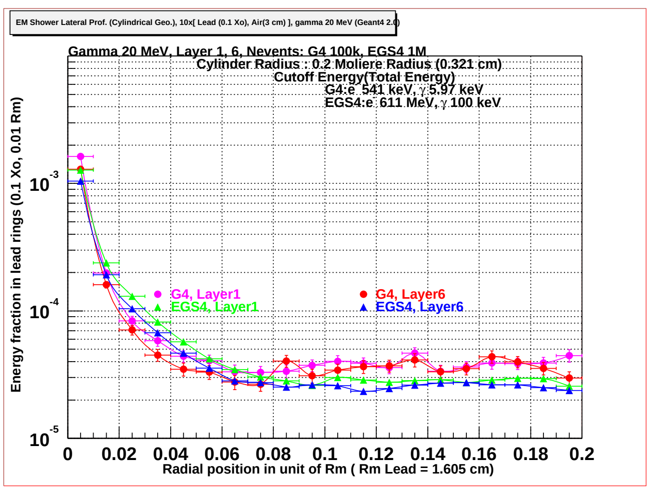

(c) 20 MeV Gamma, Lateral, Layer1, 6

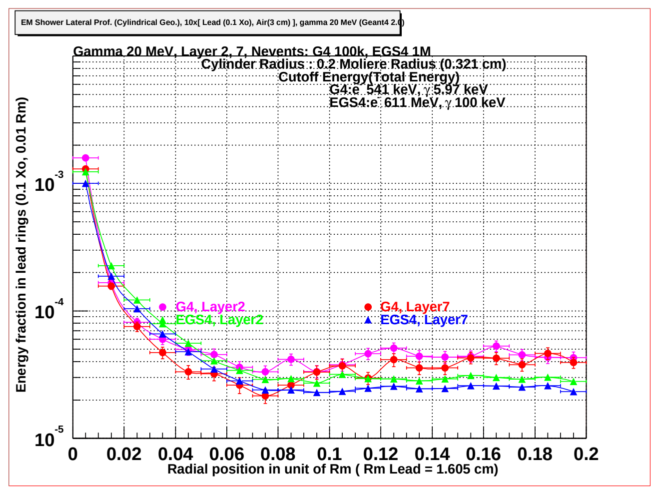

(d) 20 MeV Gamma, Lateral, Layer2, 7

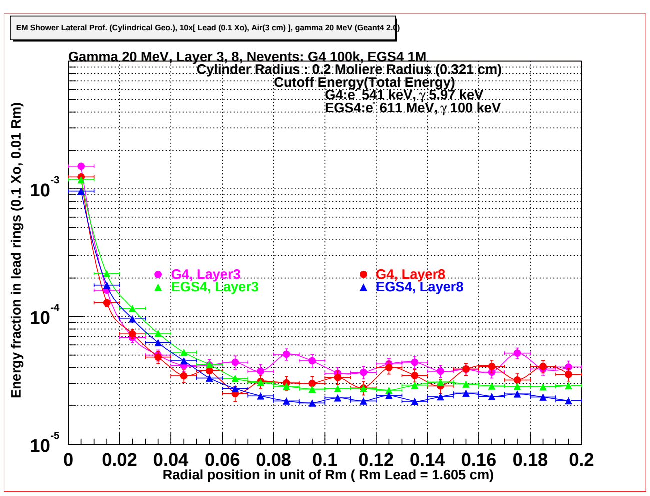

(e) 20 MeV Gamma, Lateral, Layer3, 8

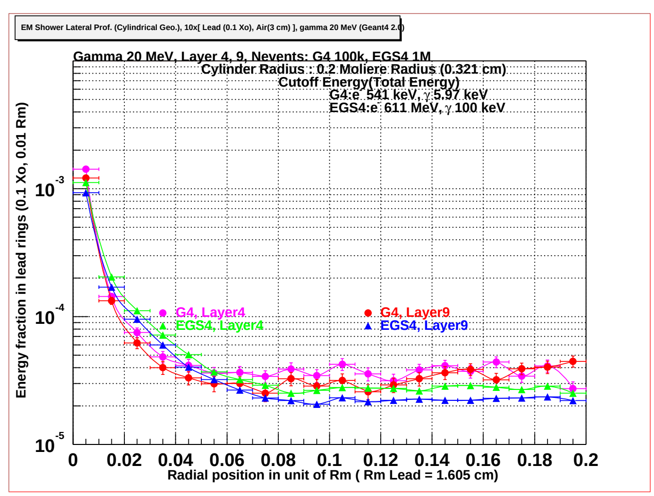

(f) 20 MeV Gamma, Lateral, Layer4, 9

Figure 4.13: Shower profiles in GLAST Tracker-like geometry of 20 MeV gamma-rays.

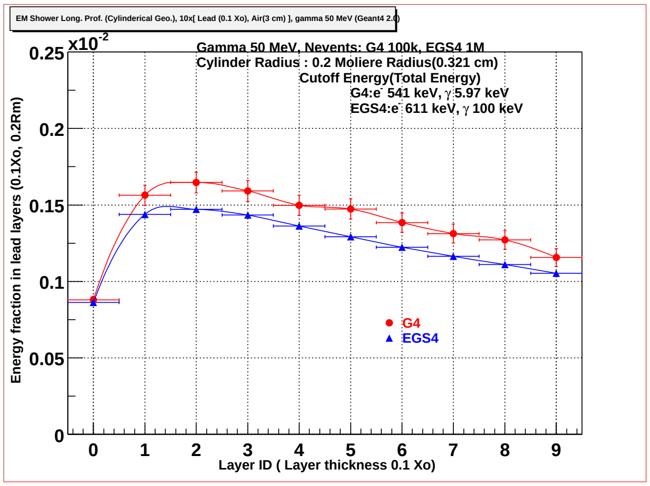

(a) 50 MeV Gamma, Longitudinal

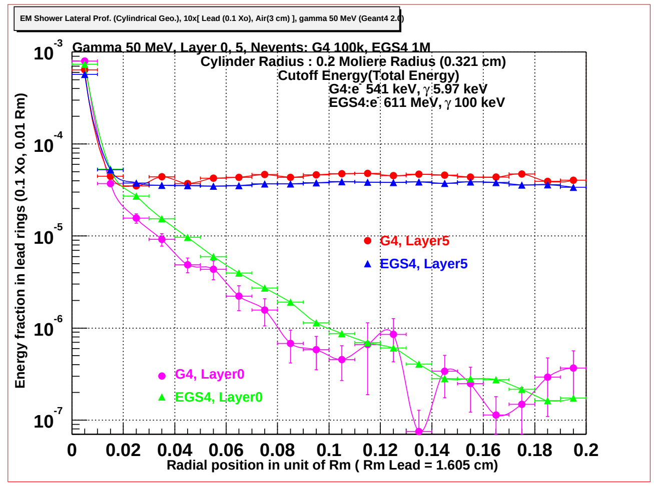

(b) 50 MeV Gamma, Lateral, Layer0, 5

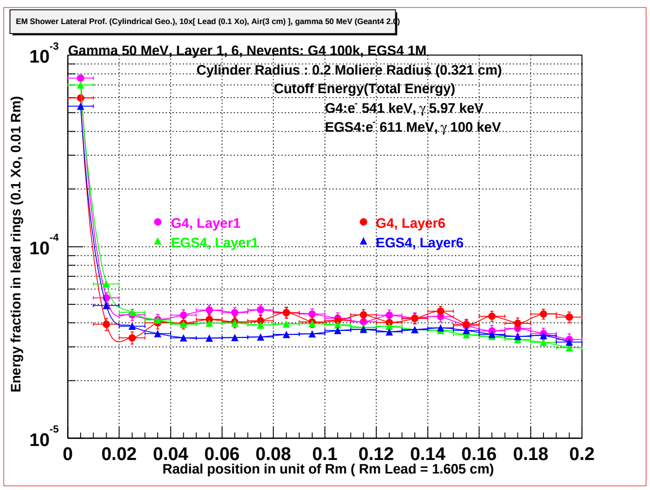

(c) 50 MeV Gamma, Lateral, Layer1, 6

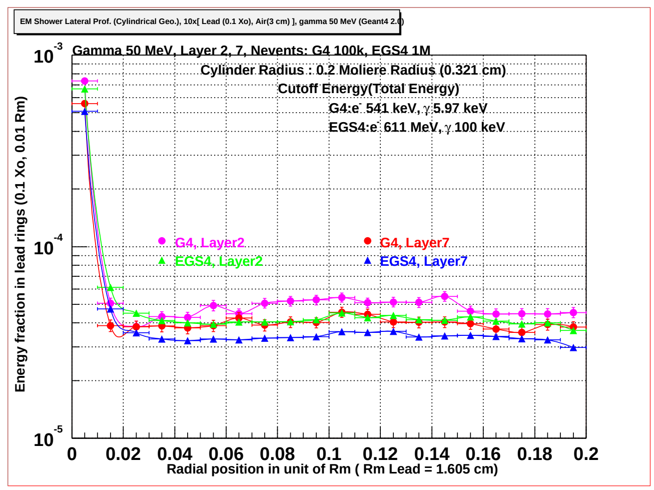

(d) 50 MeV Gamma, Lateral, Layer2, 7

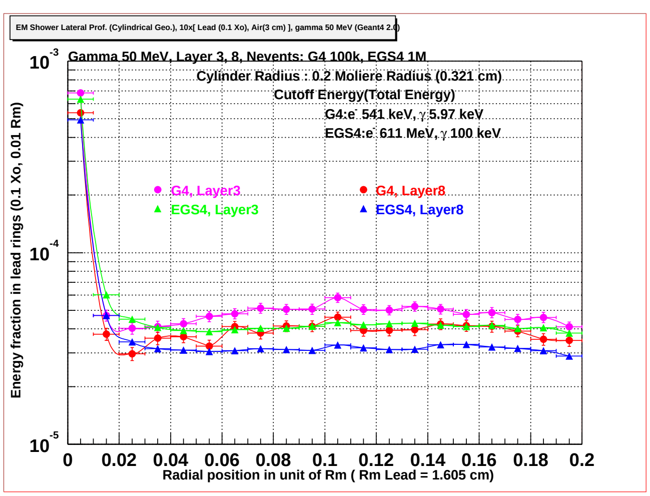

(e) 50 MeV Gamma, Lateral, Layer3, 8

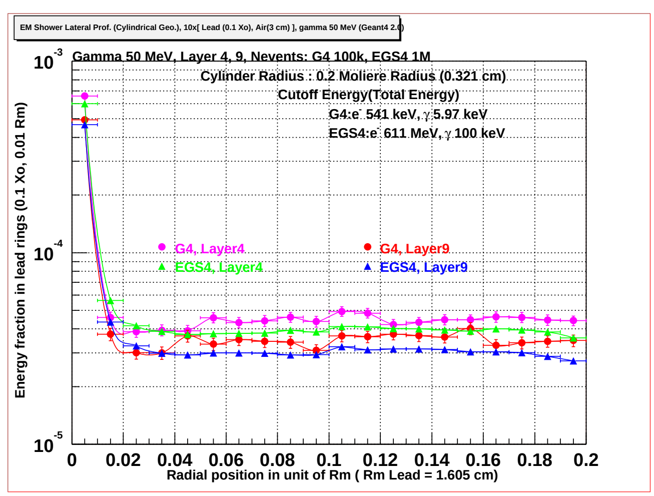

(f) 50 MeV Gamma, Lateral, Layer4, 9

Figure 4.14: Shower profiles in GLAST Tracker-like geometry of 50 MeV gamma-rays.

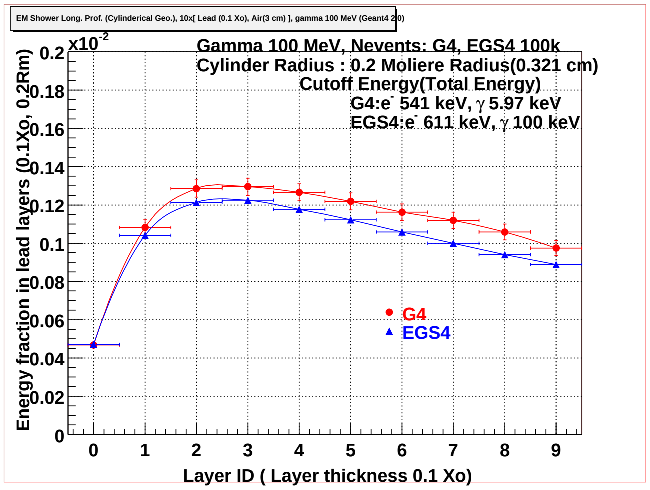

(a) 100 MeV Gamma, Longitudinal

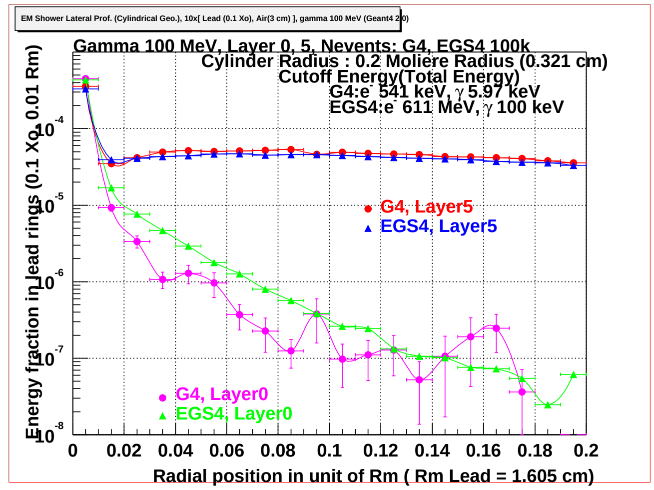

(b) 100 MeV Gamma, Lateral, Layer0, 5

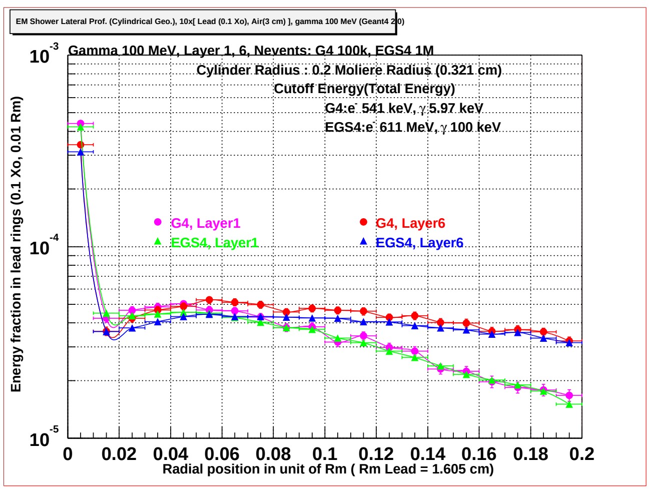

(c) 100 MeV Gamma, Lateral, Layer1, 6

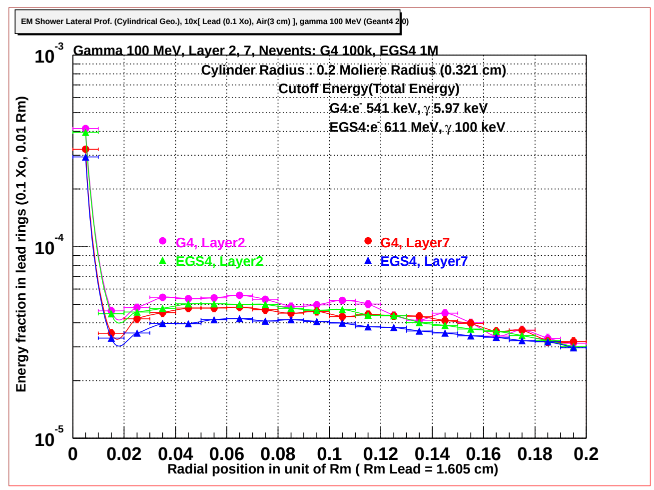

(d) 100 MeV Gamma, Lateral, Layer2, 7

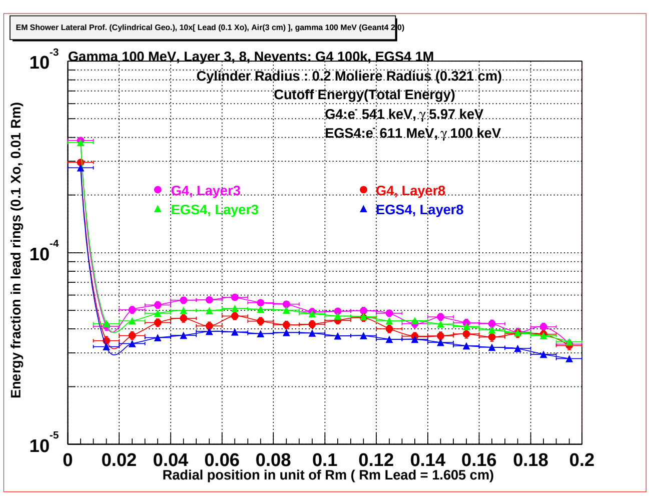

(e) 100 MeV Gamma, Lateral, Layer3, 8

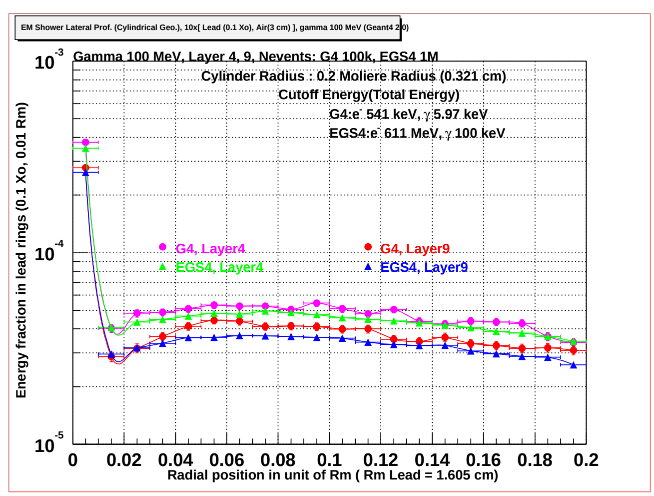

(f) 100 MeV Gamma, Lateral, Layer4, 9

Figure 4.15: Shower profiles in GLAST Tracker-like geometry of 100 MeV gamma-rays.

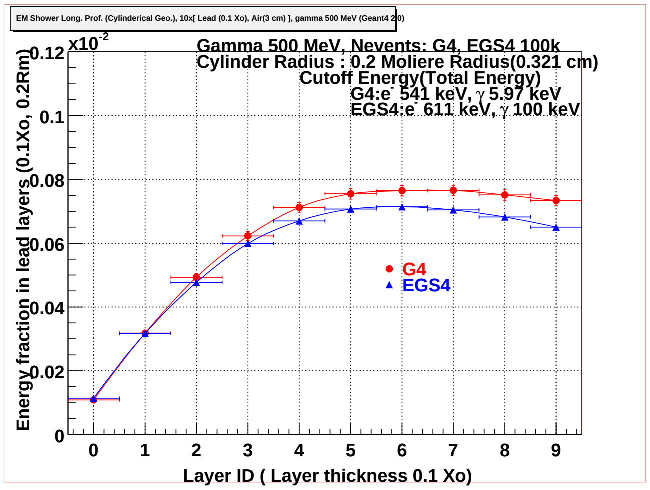

(a) 500 MeV Gamma, Longitudinal

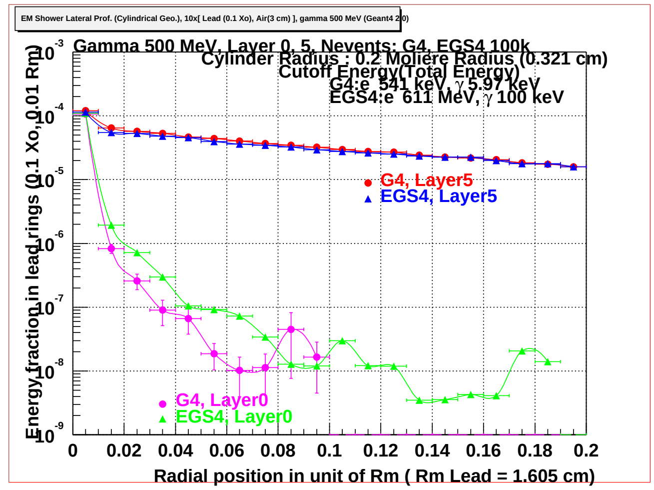

(b) 500 MeV Gamma, Lateral, Layer0, 5

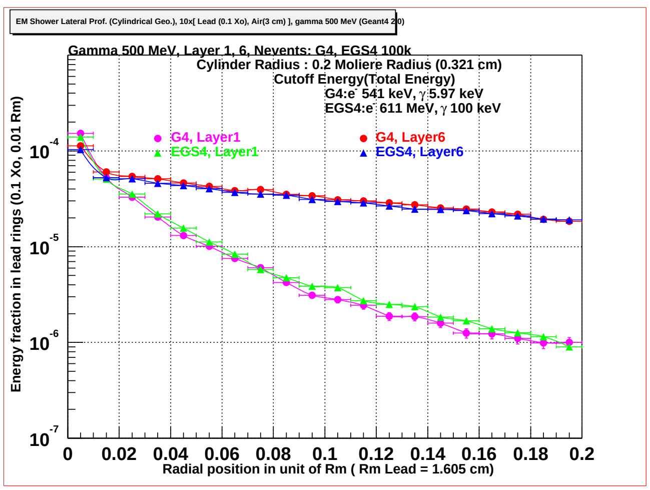

(c) 500 MeV Gamma, Lateral, Layer1, 6

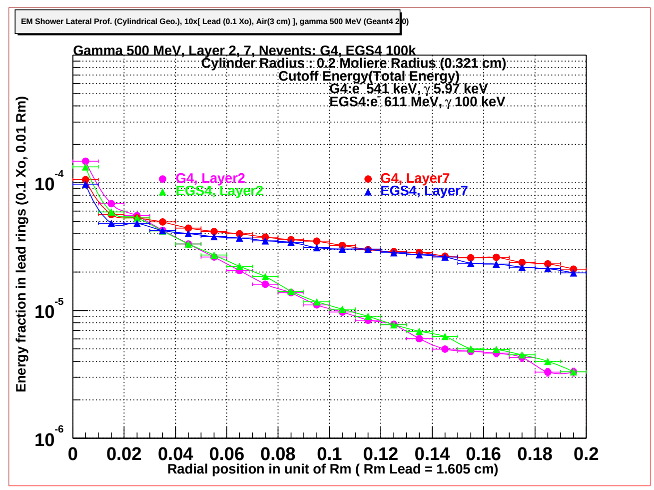

(d) 500 MeV Gamma, Lateral, Layer2, 7

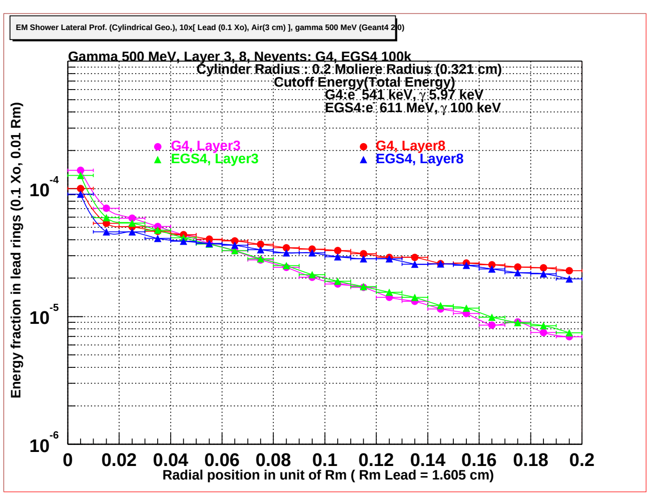

(e) 500 MeV Gamma, Lateral, Layer3, 8

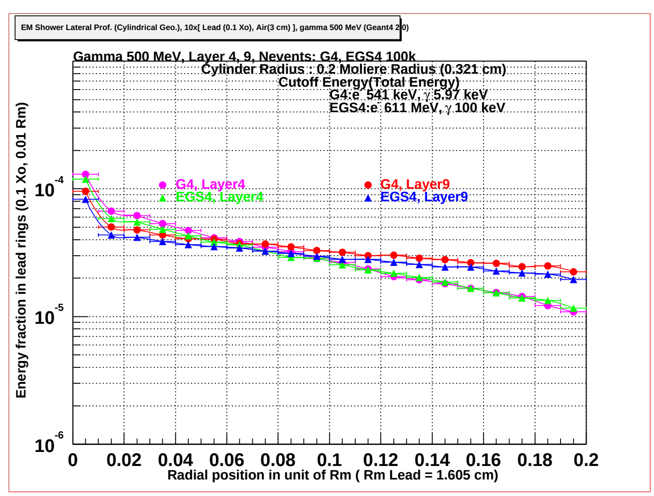

(f) 500 MeV Gamma, Lateral, Layer4, 9

Figure 4.16: Shower profiles in GLAST Tracker-like geometry of 500 MeV gamma-rays.

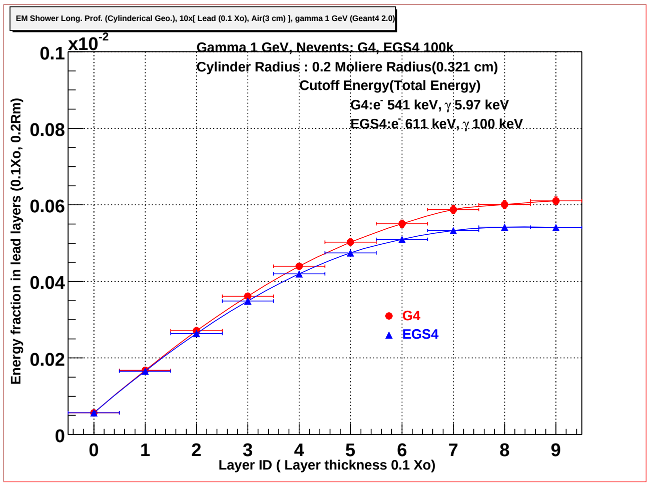

(a) 1 GeV Gamma, Longitudinal

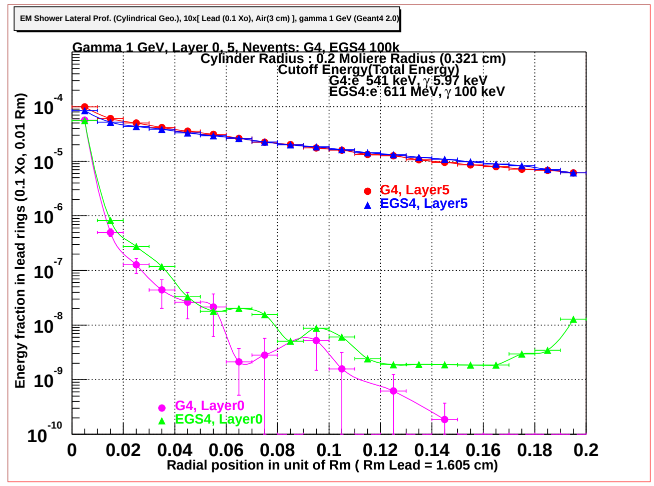

(b) 1 GeV Gamma, Lateral, Layer0, 5

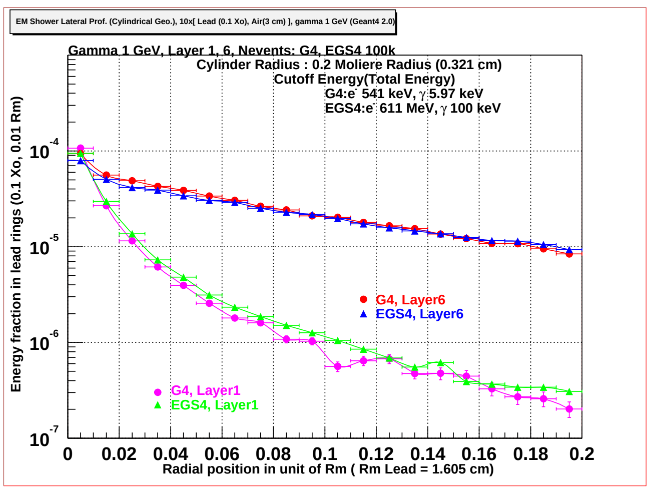

(c) 1 GeV Gamma, Lateral, Layer1, 6

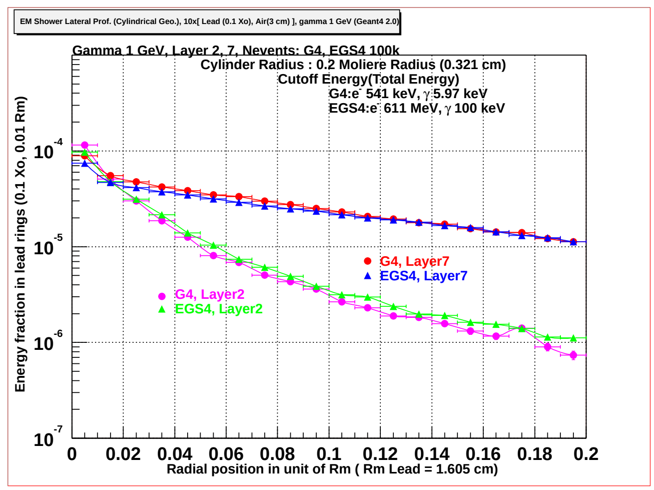

(d) 1 GeV Gamma, Lateral, Layer2, 7

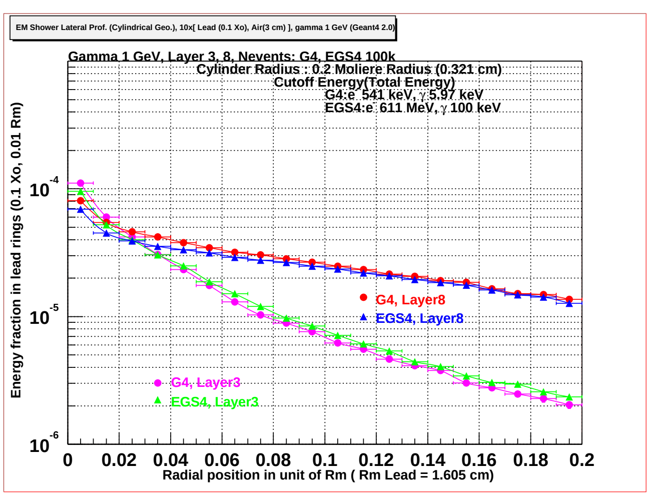

(e) 1 GeV Gamma, Lateral, Layer3, 8

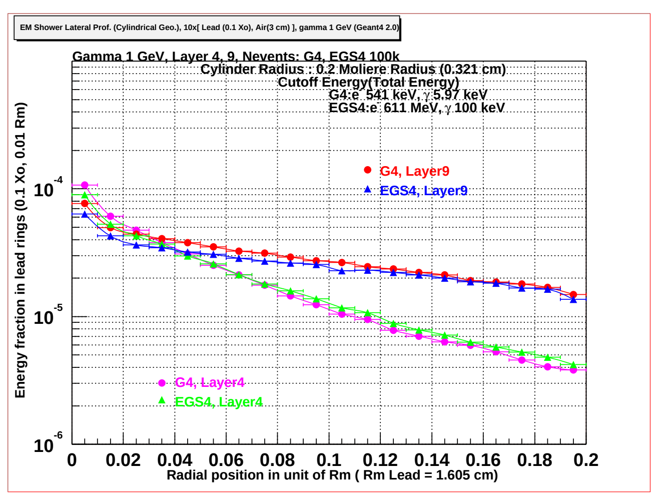

(f) 1 GeV Gamma, Lateral, Layer4, 9

Figure 4.17: Shower profiles in GLAST Tracker-like geometry of 1 GeV gamma-rays.

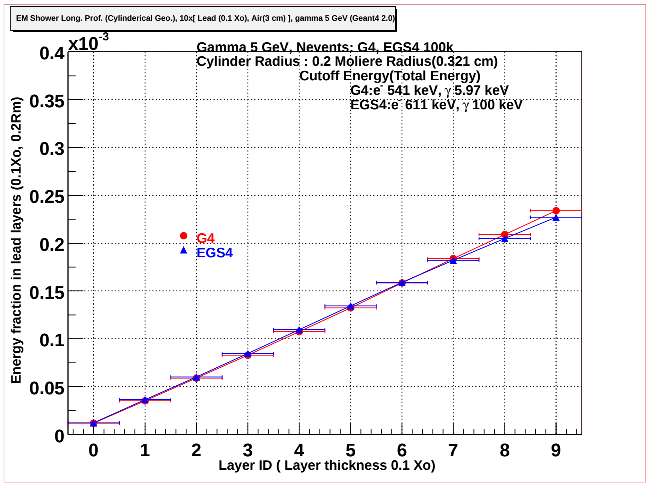

(a) 5 GeV Gamma, Longitudinal

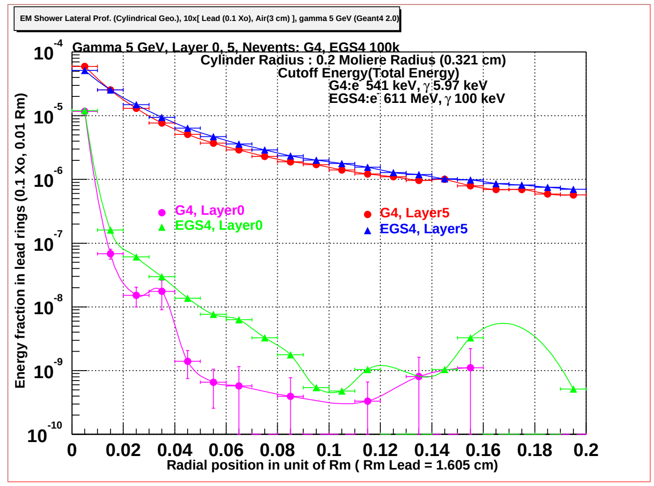

(b) 5 GeV Gamma, Lateral, Layer0, 5

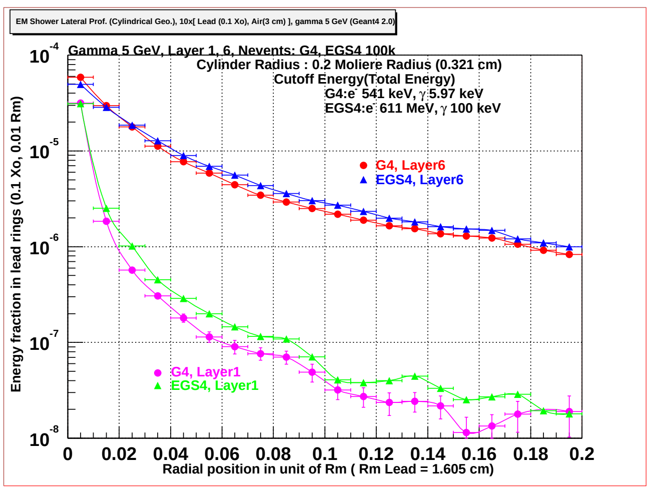

(c) 5 GeV Gamma, Lateral, Layer1, 6

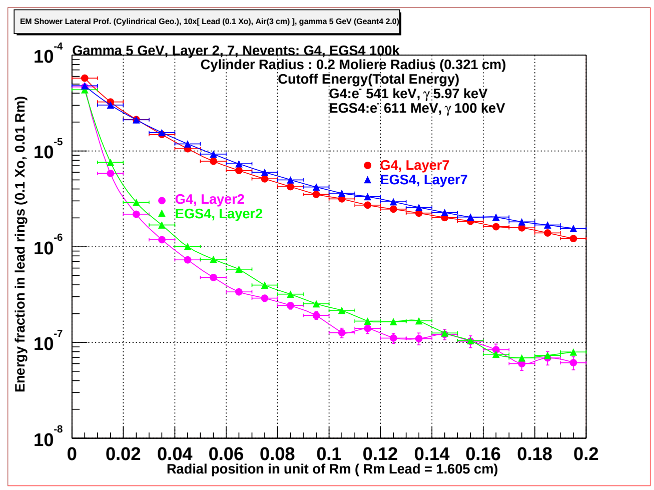

(d) 5 GeV Gamma, Lateral, Layer2, 7

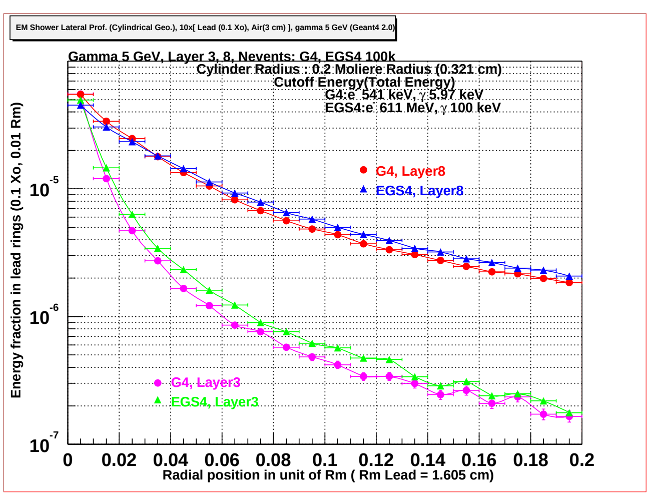

(e) 5 GeV Gamma, Lateral, Layer3, 8

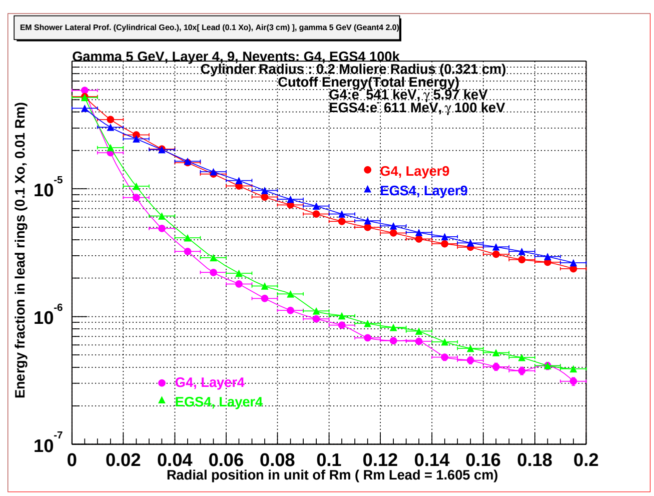

(f) 5 GeV Gamma, Lateral, Layer4, 9

Figure 4.18: Shower profiles in GLAST Tracker-like geometry of 5 GeV gamma-rays.

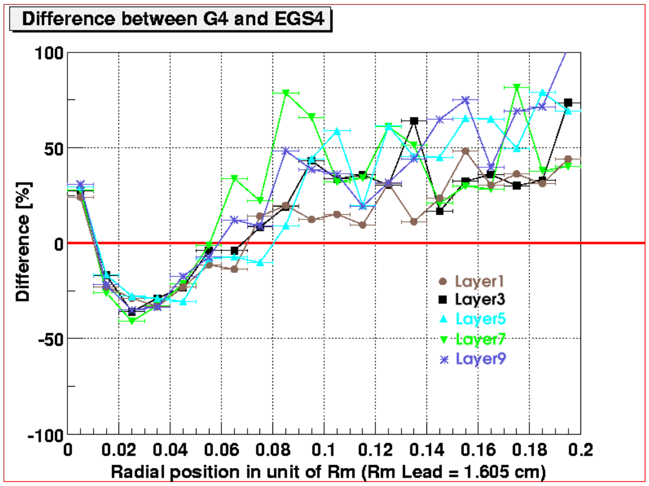

(a) 20 MeV

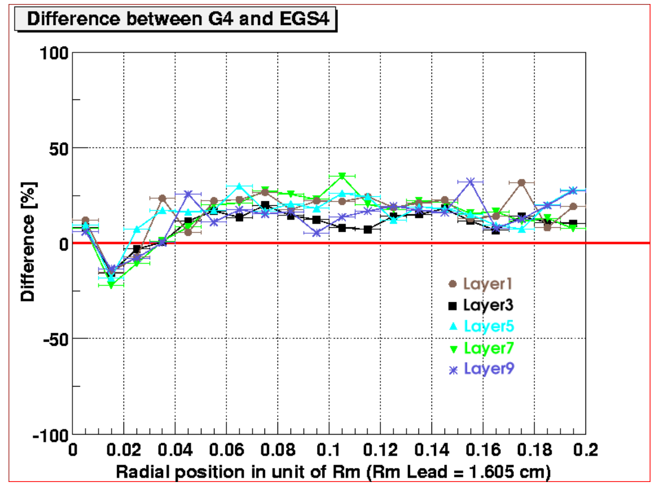

(b) 50 MeV

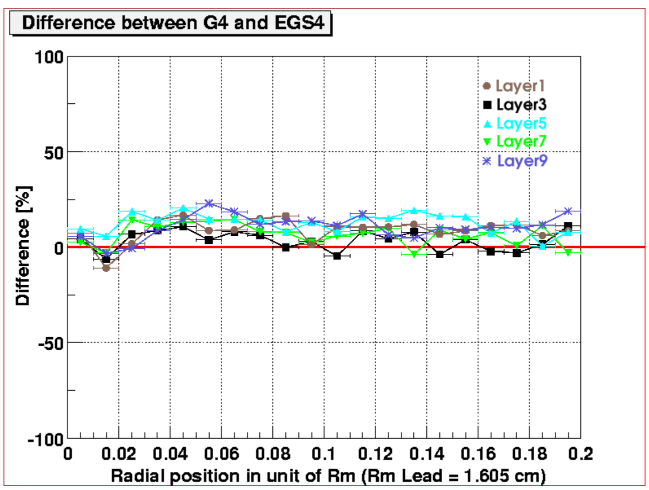

(c) 100 MeV

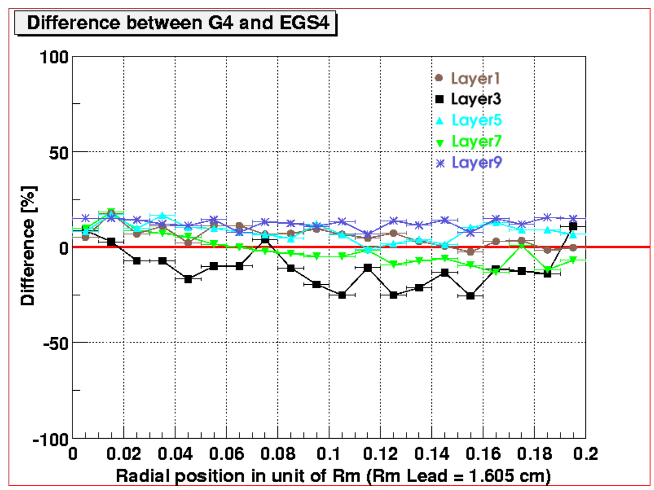

(d) 500 MeV

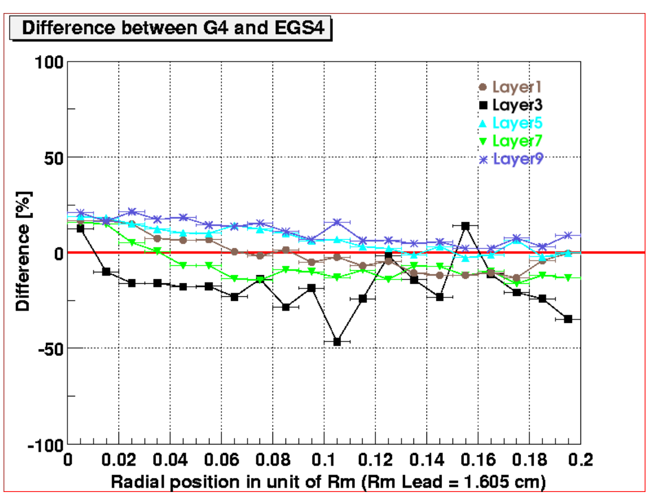

(e) 1 GeV

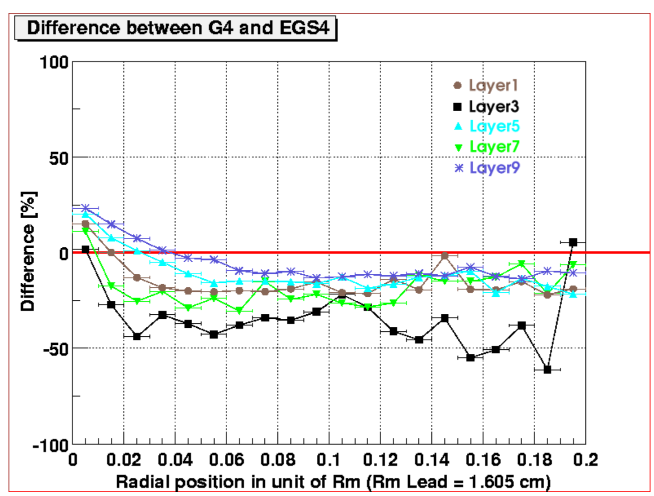

(f) 5 GeV

Figure 4.19: The difference (Geant4 - EGS4) in the energy depostions in lateral position in the absorber (simplified Tracker geo.). The results of odd layers are summarized here.

4.4 Effect of the Cutoff Energy

In the previous analysis of the shower profile in the approximated geometry of the Tracker, we have found that the shower profile of the Geant4 is narrower than that of the EGS4, especially at low energies of incident gamma-rays. To see the effect of the cutoff energy to this dicreancy, we have performed simulation with two types of cutoff, and have examined the difference. We have constructed the absorber of the geometry as shown in Figure 4.12 except for the cylinder radius is 2 Moliere radius. Table 4.6 shows the cutoff energies we applied in the simulation. The cut value we have been used in this chapter is the **cutoff2** where the cut values for electrons and gammas are 0.04 mm and 0.01 mm, respectively. In the case of **cutoff1**, we have applied 0.4 mm and 0.1 mm for the cut values for electrons and gammas, respectively. We have shot 20 MeV gamma-rays along the axis of the cylinder. The number of particles we shot is 100k for the Geant4 and 1M for the EGS4. The results are shown in Figure 4.20. The plot shows no significant difference in the longitudinal profiles bwteen two types of cutoff, indicating that the cutoff value does not cause the narrow shower profile.

Table 4.6: Cut Value in the simulations, shown as an energy of the particle.

	Geant4		EGS4	
	Electron	Photon	Electron	Photon
cutoff1	637 keV	29.3 keV	1.5 MeV	100 keV
cutoff2	541 keV	5.97 keV	611 keV	100 keV

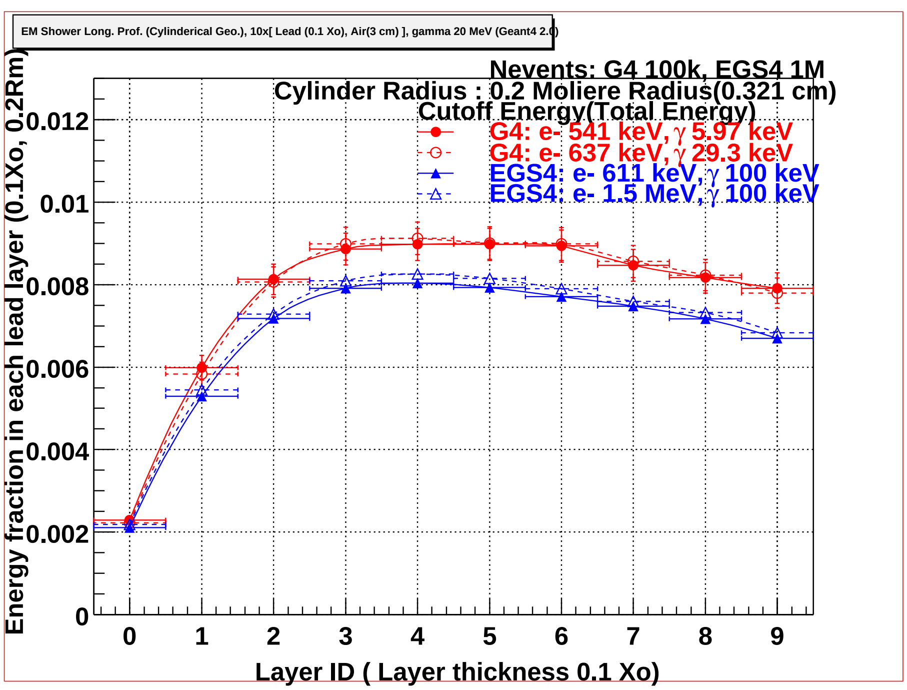

Figure 4.20: The comparison of the longitudinal shower profiles of the Geant4 and EGS4 for two different cutoff energies.

4.5 Conclusions

In section 4.1, we have investigated the growth of the electromagnetic shower and have found that the shower profile reproduced by the Geant4 is narrower than those of the EGS4 and Crannell experiment. This feature could be comfirmed in the gamma-ray-induced electromagnetic shower ranging from 20 MeV to 100 GeV. We have also examined the effect of the cutoff energy by reproducing the electromagnetic shower changing the cutoff energy and have concluded that the cutoff value does not cause the narrow shower profile. Therefore, the phycics process related to the electromagnetic shower in the Geant4, e.g., Møller scattering, Bhabha scattering, bremsstrahlung and pair creation, need to be assessed. In Chapter 5, we investigate whether the Geant4 appropriately reproduces these processes or not.

Chapter 5

Validation of Processes constituting Electromagnetic Shower

The electromagnetic shower is composed of several processes. Electrons and positrons emitted by pair creation suffer the elastic scattering against atomic electrons in matter. These processes, called Møller and Bhabha scattering, also contribute the shower profile, as well as bremsstrahlung and pair creation. To find out the reason of the discrepancy of the electromagnetic shower profile of the Geant4 found in Chapter 4 and to evaluate the accuracy of the each process, we examine Møller scattering, Bhabha scattering, electron bremsstrahlung and pair creation.

5.1 Møller Scattering and Bhabha Scattering

5.1.1 Theoretical formula for Møller Scattering

Møller scattering is the elastic scattering between two electrons. For $pc \gg m_e c^2$ the differential cross section in the center-of-mass system from the first-order perturbation theory can be written as

$$\frac{d\sigma}{d\Omega} = \left(\frac{r_e^2}{4}\right)\left(\frac{m_e c^2}{pc}\right)^2 \frac{(3+\cos^2\theta)^2}{\sin^4\theta} \tag{5.1}$$

where

r_e	classical electron radius
m_e	rest mass of electron
p	momentum in the center-of-mass system

In this section we compare the Geant4 simulation with this equation.

In the Geant4 the direction of the scattered electron is generated with respect to the direction of the incident particle. First, the azimuthal angle is generated isotropically. The polar angles, θ, is calculated from the energy momentum conservation after sampling the kinetic energy, T, of the scattered electron based on the following differentical cross section, [11]

$$\frac{d\sigma}{d\epsilon} = \frac{2\pi Z r_e^2 m_e c^2}{E - m_e c^2}\left(\frac{\gamma^2}{\gamma^2-1}\right)^2 \left[\frac{(\gamma-1)^2}{\gamma^2} + \frac{1}{\epsilon}\left(\frac{1}{\epsilon} - \frac{2\gamma-1}{\gamma^2}\right) + \frac{1}{1-\epsilon}\left(\frac{1}{1-\epsilon}\frac{2\gamma-1}{\gamma^2}\right)\right] \tag{5.2}$$

where,

Z	atomic number of the absorber
E	energy of incident electron
T	kinetic energy of scattered electron
γ	E/m_ec^2
ϵ	$T/(E - m_ec^2)$

5.1.2 Geant4 Simulation of Møller Scattering

We have constructed one disk layer of Pb as Figure 5.1 and shot 20 and 100 MeV electrons into the disk to reproduce the Møller scattering. The parameters used in the Geant4 simulation are summarized in Table 5.1 and the schematic geometry is shown in Figure 5.1. In the Geant4 the cutoff energies are defined in the stopping range and we set the values as 0.4 mm and 0.1 mm for electrons and other particles, respectively. In Table 5.1, the cut values of the total energy for electrons and photons are tabulated. We have modified the Møller scattering part of the Geant4 code, G4eIonisation.cc, to get all information of Møller scattering occurred in the absorber: the scattering angle of two electrons, the energy of parent electron before scattering, and the energies of two electrons after scattering. In general, electrons reduce their energy in the absorber more or less before Møller scattering occurrs and differential cross section varies from energy to energy. To exmine the angular distribution at a certain energy we have selected the electrons between 19 MeV and 20 MeV for the 20 MeV incident electron and those between 99 MeV and 100 MeV for the 100 MeV incident electron when Møller scattering occurred.

Table 5.1: Parameters for the Geant4 simulation of Møller and Bhabha scattering

Incident energy	20 MeV	100 MeV
Energy selection	19 - 20 MeV	99 - 100 MeV
Number of events	1 M	1 M
Cut value	electron	gamma
Lead	541 keV	5.97 keV

We have compared the Geant4 results with the theoretical formula of the differential cross section in the laboratory system for Møller scattering. The results are shown in Figure 5.2. When we nomalized the differential cross section, we removed the events where bremsstrahlung occurred before Møller scattering. The numbers of removed events due to the bremsstrahlung were 29,415 and 51,956 in 1 M events for 20 MeV and 100 MeV, respectively. The numbers of events where Møller scattering occurred were 28,430 and 28,072 for 20 MeV and 100 MeV, respectively. Figure 5.2 shows that the Geant4 reproduced Møller scattering of 20 MeV and 100 MeV electrons quite well.

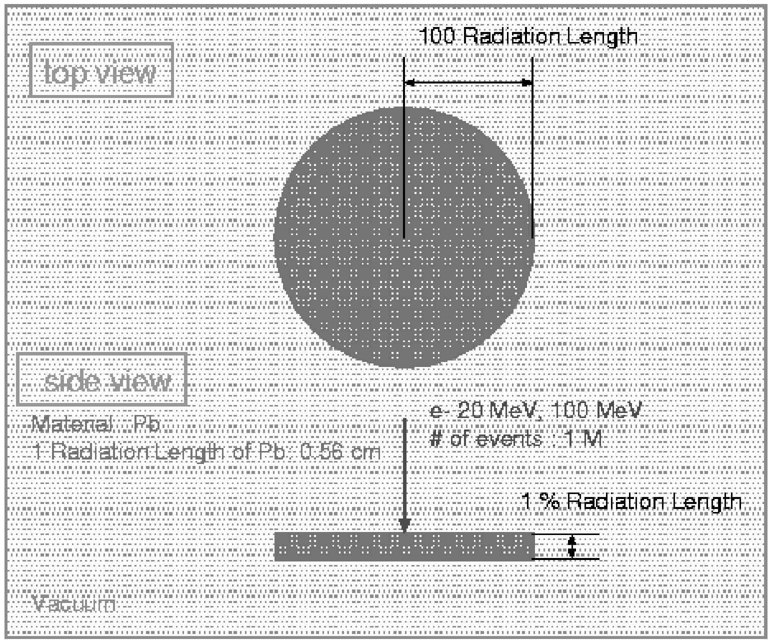

Figure 5.1: The schematic figure of the geometry for the simulation of Møller and Bhabha scattering. The absorber is a disk of Pb with a thickness of 0.0056 cm.

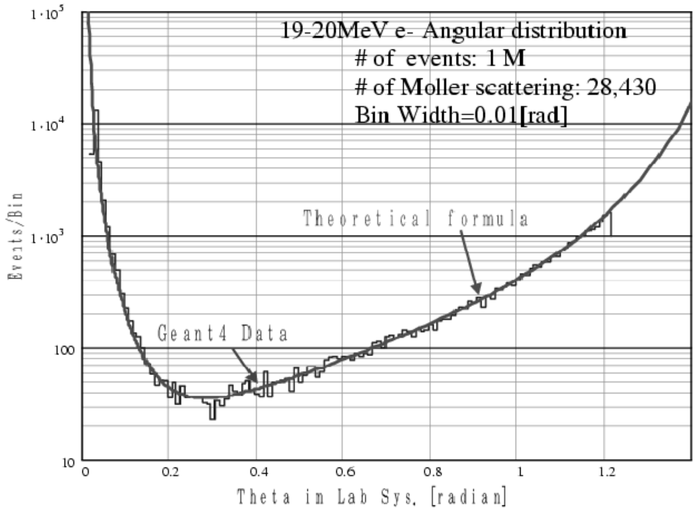

(a) 19 - 20 MeV electrons

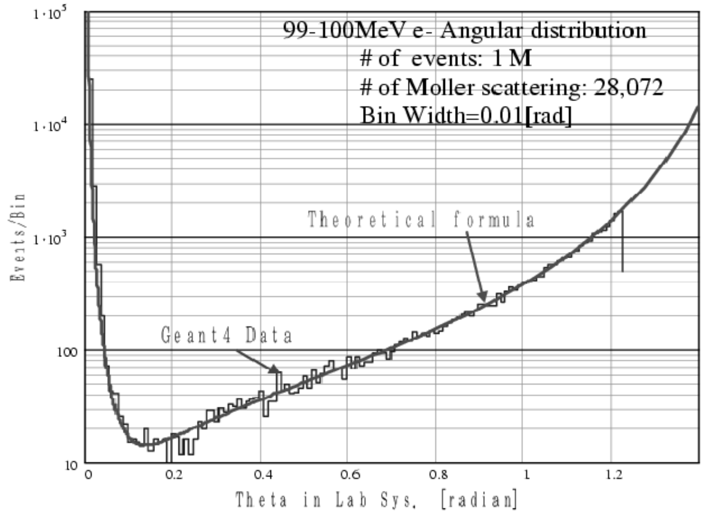

(b) 99 - 100 MeV electrons

Figure 5.2: Angular distribution of Møller scattering in the Geant4 simulation (histogram) and normalized differential cross section in the laboratory system for Møller scattering(solid line).

5.1.3 Theoretical formula for Bhabha Scattering

Bhabha scattering is the elastic scattering of positrons against electrons. For $pc \gg m_e c^2$ one obtains the differential cross section in the center-of-mass system in first-order perturbation theory. In the relativistic limit, we have:

$$\frac{d\sigma}{d\Omega} = \left(\frac{r_{e^2}}{2}\right)\left(\frac{m_e c^2}{pc}\right)^2 \left[\frac{1}{4}\frac{1+\cos^4(\theta/2)}{\sin^4(\theta/2)} + \frac{1}{8}(1+\cos^2\theta) - \frac{1}{2}\frac{\cos^4(\theta/2)}{\sin^2(\theta/2)}\right] \tag{5.3}$$

where

r_e	classical electron radius
m_e	rest mass of electron
p	momentum in the center-of-mass system

We examine the angular distribution of Bhabha scattering by comparing the above equation with the Geant4 data.

The Geant4 calculates the azimuthal and polar angles of scattered electrons (positrons) with respect to the direction of the incident positrons (electrons), same as the calculation of Møller scattering mentioned in the previous section (§5.1.1) although the following differentical cross section is used in order to sample the kinetic energy, T, of particle emitted by Bhabha scattering. [11]

$$\frac{d\sigma}{d\epsilon} = \frac{2\pi Z r_e^2 m_e c^2}{E - m_e c^2}\left[\frac{\gamma^2}{(\gamma^2-1)\epsilon^2} - \frac{B_1}{\epsilon} + B_2 - B_3\epsilon + B_4\epsilon\right] \tag{5.4}$$

where,

Z	atomic number of the absorber	E	energy of incident electron
T	kinetic energy of scattered electron	γ	$E/m_e c^2$
l	$1/(\gamma+1)$	B_1	$2 - l^2$
B_2	$(1-2l)(3+l^2)$	B_3	$(1-2l)^2 + (1-2l)^3$
B_4	$(1-2l)^3$	ϵ	$T/(E - m_e c^2)$

5.1.4 Geant4 Simulation of Bhabha scattering

We have constructed the same disk layer of Pb as in the previous simulation of Moller scattring. Then, we have shot positrons of 20 MeV and 100 MeV into the disk to reproduce Bhabha scattering. The parameters used in the Geant4 simulation are summarized in Table 5.1. As we have done in the analysis of Moller scattering, we have modified the Bhabha scattering part of the Geant4 code, G4eIonisation.cc, to get all information of Bhabha scattering occurred in the absorber: the scattering angles of positrons, the energies of parent positrons before scattering and the energies of positrons after scattering. For the same reason as in the study of Møller scattering, we have selected incident positrons in terms of their energy (Table 5.1).

The comparison of the Geant4 results with the theoretical formula of the differential cross section in the laboratory system are shown in Figure 5.3, indicates that the Geant4 reproduces

Bhabha scattering quite well. There, we have removed the events where bremsstrahlung occurred before Bhabha scattering occurs. The numbers of events sampled in Figure 5.3 were 26,834 and 27,262 for 20 MeV and 100 MeV, respectively.

5.1.5 Conclusions

In this section we have inquired into the angular distribution of Moller scattering and Bhabha scattering by comparing the theoretical differential cross sections. As a result we have found that the Geant4 reproduced the theoretical angular distribution quite well.

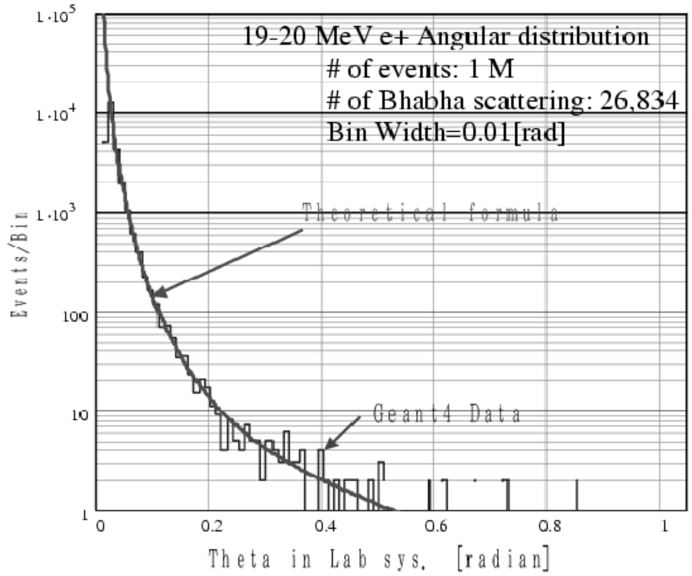

(a) 19 - 20 MeV positrons

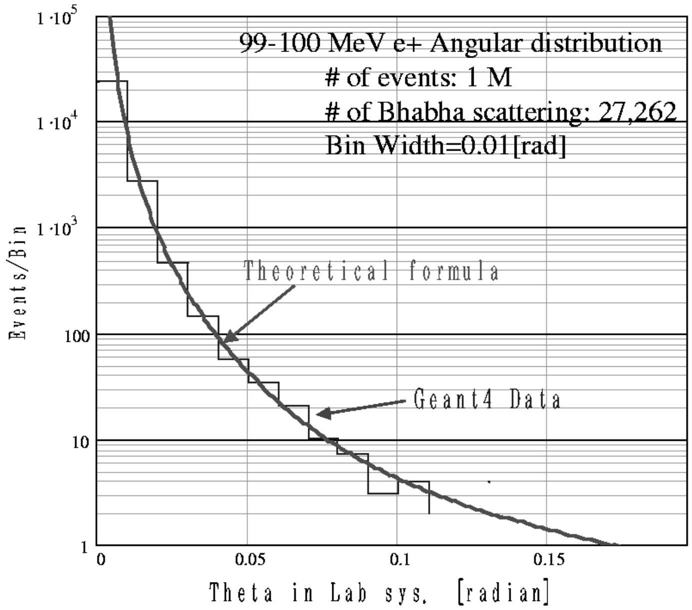

(b) 99 - 100 MeV positrons

Figure 5.3: Angular distribution of Bhabha scattering in the Geant4 simulation (histogram) and normalized differential cross section in the laboratory system for Bhabha scattering(solid line).

5.2 Bremsstrahlung

5.2.1 Angular distribution formula of emitted gamma-ray implemeted in Geant4

In this section we examine the angular distribution of electron bremsstrahlung in the Geant4. In the Geant4 simulation, the angular distribution of emitted gamma-ray by electron bremsstrahlung is calculated in the Geant4 code, G4eBremsstrahlung.cc. In the calculation the azimuthal angle is generated isotropically. The polar angular distribution is calculated based on the approximation of the Tsai formula [12, 13]. Tsai formula is the differential cross section of bremsstrahlung in photon energy and angle, and is written as,

$$\frac{d\sigma}{dkd\Omega} = \frac{2\alpha^3(\hbar c)^2}{\pi k}\frac{E^2}{(m_ec^2)^4}\left\{\left[\frac{2y-2}{(1+u^2)^2} - \frac{12u^2(1-y)}{(1+u^2)^4}\right](Z^2+Z)\right.$$
$$\left. + \left[\frac{2-2y+y^2}{(1+u^2)^2} + \frac{4u^2(1-y)}{(1+u^2)^4}\right][X - 2Z^2 f((\alpha Z)^2)]\right\} \tag{5.5}$$

where

$$u = \frac{E\theta}{m_ec^2}$$
$$X = \int_{t_{min}}^{(m_ec^2)^2(1+u^2)^2} [G_Z^{el}(t) + G_Z^{inel}(t)]\frac{(t-t_{min})}{t^2}dt$$
$$t_{min} = \left[\frac{k(m_ec^2)^2(1+u^2)}{2E(E-k)}\right]^2$$

$G_Z^{el,in}(t)$ atomic form factors

f Coulomb correction

$\alpha = 1/137$ fine structure constant

where E is the energy of the incident electron, k is the energy of photon, $y = k/E$, Z is the atomic number of a material and m_e is the electron mass. According to Physics Reference Manual of the Geant4 [14], the following approximated distribution as a function of $u = E\theta/m_ec^2$ is utilized to determine the angular distribution in the Geant4 since the Tsai distribution is quite complicated to sample and shows a very weak dependence on Z, E, k and y for a given value of u.

$$f(u) = C\left(ue^{-au} + due^{-3au}\right) \tag{5.6}$$

where

$C = \frac{9a^2}{9+d}$ $\quad a = 0.625$ $\quad d = 0.13\left(0.8 + \frac{1.3}{Z}\right)\left(100 + \frac{1}{E}\right)(1+y)$

where E is in GeV. However we have found that the Geant4 actually uses the constant $d = 27$ in the equation 5.6 instead of the variable d as mentioned above. Therefore we have examined the difference between the variable d and the constant d in various energies, as shown in Figure 5.4. This plot shows no remarkable difference between these distributions. We thus use the equation 5.6 with the constant d in the following analysis.

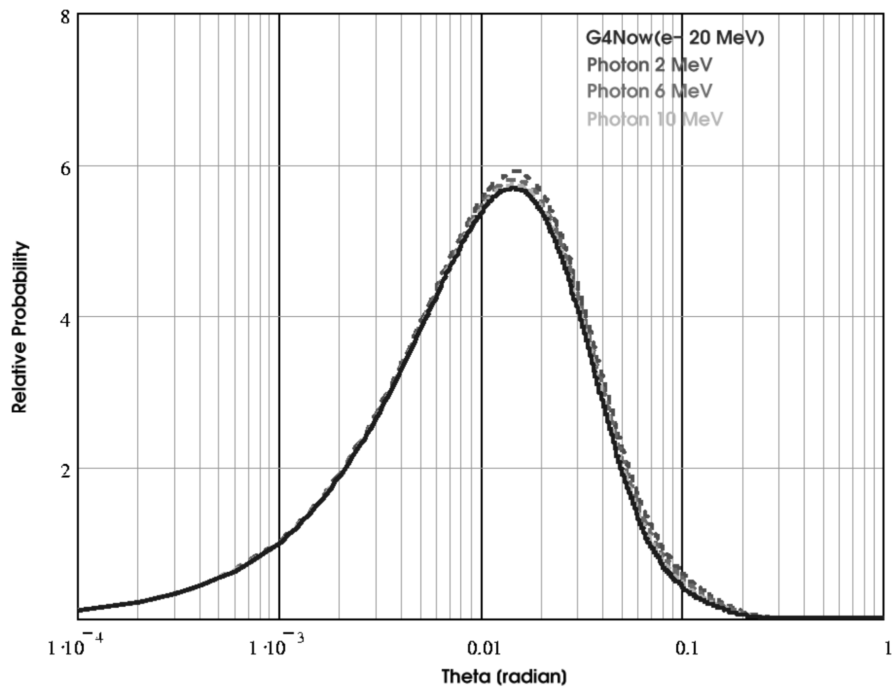

Figure 5.4: Comparison of the equation 5.6 with the constant $d = 27$ and the variable d. The incident energy is 20 MeV. Solid line represents the equation 5.6 with the constant d, which is currently implemented in the Geant4. This distribution is independent on the energy of generated photon. Dashed lines show the equation 5.6 with the variable d for 2 MeV, 6 MeV and 10 MeV photons, respectively. These four formulas show almost the same distribution.

5.2.2 Geant4 simulation

We have examined the angular distributions of photons of 2 MeV, 6 MeV and 10 MeV produced by bremsstrahlung of 20 MeV electrons to examine whether a Geant4 simulator reproduces the theoretical formula or not. In the Geant4 simulation we have constructed the same lead absorber in the analysis of Moller scattering, as shown in Figure 5.1, except for the thickness. The thickness used here is 10% radiation length of lead (0.056 cm) so as to get enough number of events. The number of electron we shot is 100k and the energy is 20 MeV. The cutoff energy is same as that used in the simulation of Moller scattring. We have modified G4eBremsstrahlung.cc to extract the data of bremsstrahlung, e.g., the energy of the parent electron before and after bremsstrahlung occurs, the energy of the generated photon and the scattering angle of the photon. To investigate bremsstrahlung of 20 MeV electron, we have selected events where energies of electrons that emit photons range from 19 MeV to 20 MeV. As for the equation 5.6, only the shape has meaning. Therefore we have normalized the theoretical values so that the height of the peak in the approximated Tsai distribution coincides with that of the Geant4 data.

We have compared the simulation and theoretical angular distribution in three energy ranges of emitted photons, as shown in Figure 5.5. In the plots histograms and dashed lines represent the Geant4 data and the equation 5.6, respectively. These plots show that the Geant4 data agreed with the equation 5.6 very well. We have concluded that the Geant4 well simulates the angular distribution of bremsstrahlung (equation 5.6).

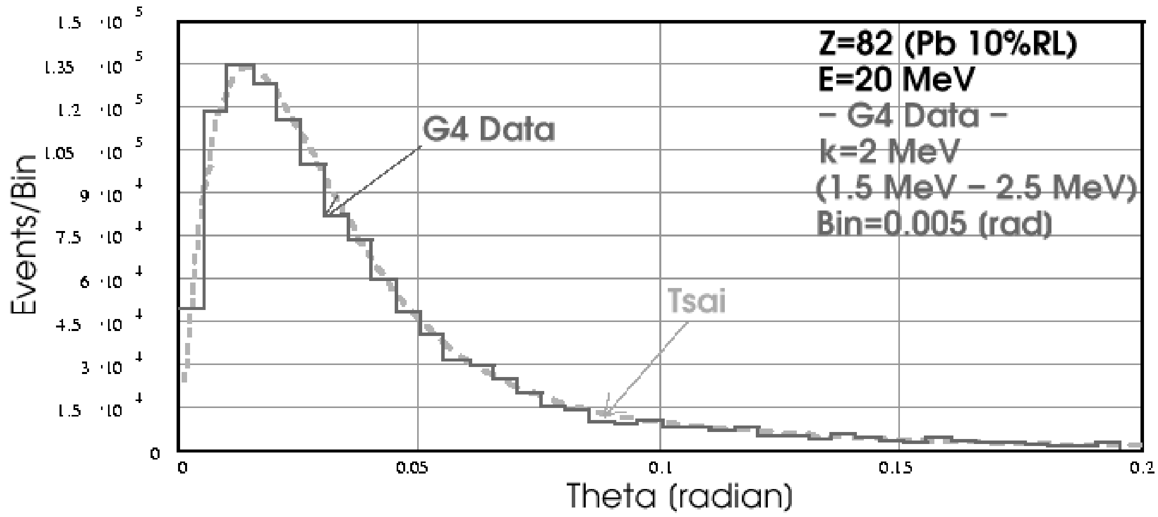

(a) Photon from 1.5 MeV to 2.5 MeV

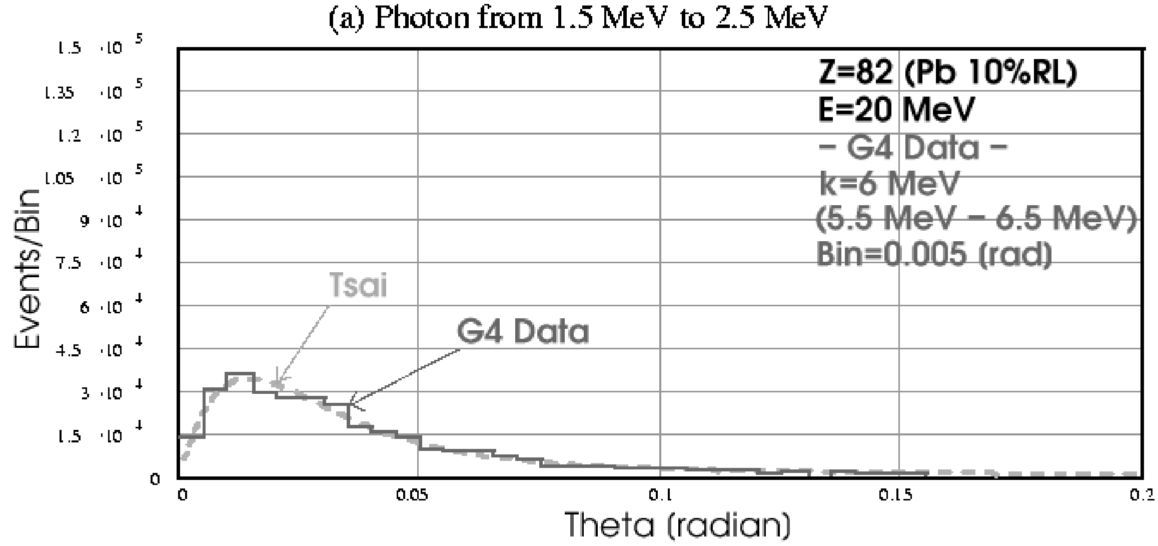

(b) Photon from 5.5 MeV to 6.5 MeV

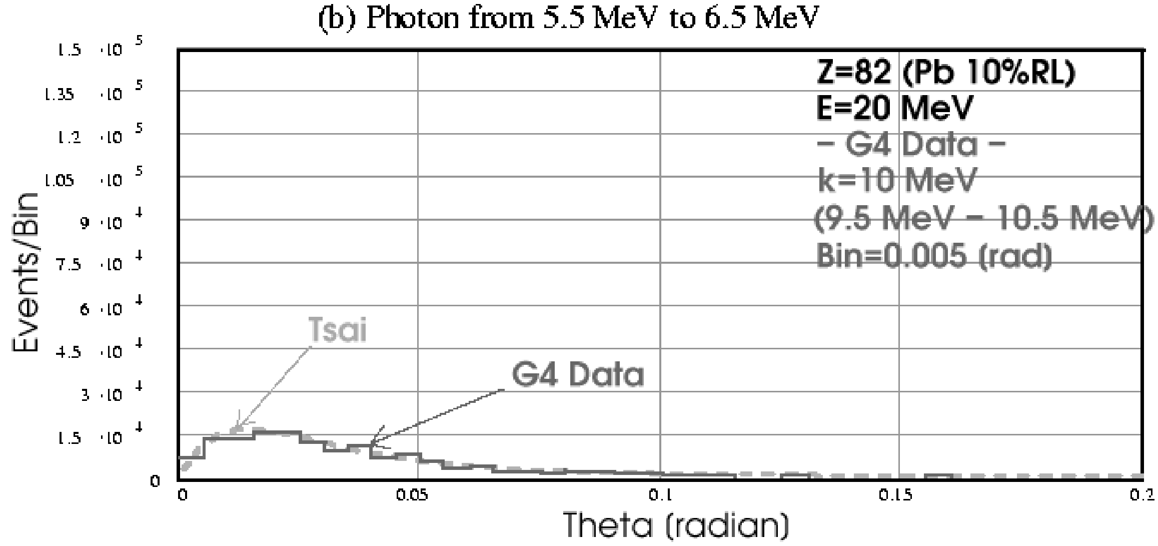

(c) Photon from 9.5 MeV to 10.5 MeV

Figure 5.5: The angular distribution of photons emitted by bremsstrahlung of electron of 20 MeV. Dashed lines and histograms represent the equation 5.6 and the Geant4 data, respectively. As for the distribution of the equation 5.6, only the shape has meaning.

5.2.3 Comparison with Schiff Distribution

EGS4 refers to different formula from that of the Geant4, called Schiff formula, to determine the angular distribution of photons generated via electron bremsstrahlung. In this section, we examine whether there exists any difference between two distributions by means of comparing the Geant4 data with Schiff formula to see if the difference between two formulas can cause the narrow shower profile of the Geant4 found in Chapter 4. The differential cross section of bremsstrahlung in photon energy and angle by Schiff is written as,[15]

$$\frac{d\sigma}{dkdy} = \frac{4\alpha Z^2 r_e^2 y}{k}\left\{\frac{16y^2E}{(y^2+1)^4E_0} - \frac{(E_0+E)^2}{(y^2+1)^2E_0^2} + \left[\frac{E_0^2+E^2}{(y^2+1)^2E_0^2} - \frac{4y^2E}{(y^2+1)^4E_0}\right]\ln M(y)\right\} \tag{5.7}$$

where,

$$y = E_0\theta/m_ec^2; \frac{1}{M(y)} = \left(\frac{km_ec^2}{2E_0E}\right)^2 + \left(\frac{Z^{1/3}}{111(y^2+1)}\right)^2,$$

where the following definitions for the variables apply:

k	energy of the photon
θ	angle between the outgoing photon and the incoming electron direction (in radian)
Z	atomic number of the target material
r_e	$\equiv e^2/4\pi\epsilon_0 m_ec^2$ (classical electron radius)
E_0,E	initial and final electron energy
α	=1/137 (fine structure constant)

The following table, derived from the H. W. Koth et al.[15] article, outlines the essential approximations employed in the development of Schiff formula.

	Approximation	Condition of validity
(1)	Approximate screening potential	$(Ze/r)e^{-r/a}$
(2)	First order Born approximation	$(2\pi Z/137\beta_0) \ll 1, (2\pi Z/137\beta) \ll 1$
(3)	Extreme relativistic	$E_0, E, k \gg m_ec^2$
(4)	Small angles	$\sin\theta = \theta$
(5)	Approximate e^- angular integration	$\theta < (Z^{1/3}m_ec^2/111E_0)$

The condition of the simulation is the same as the previous simulation except for the incident electron energy. We have tried two energies of the incident electrons, 20 MeV and 100 MeV. The results of the comparion between the Geant4 data and Schiff distribution are shown in Figure 5.6 and 5.7. The histograms and solid lines in the plots are the angular distiribution of the Geant4 and Schiff formulas, respectively. The Geant4 data agreed with Schiff distribution very well.

5.2.4 Conclusions

First we have validated the implementation of the angular distirubution of bremsstrahlung whether it follows the formula referred in the Geant4 and have found that the Geant4 reproduces the equation 5.6 appropriatelly. Second, we have compared it with Schiff formula used in EGS4 and have reached to the conclusion that the Geant4 reproduces Schiff distribution quite well, indicating that bremsstrahlung does not cause the narrow shower profile of the Geant4.

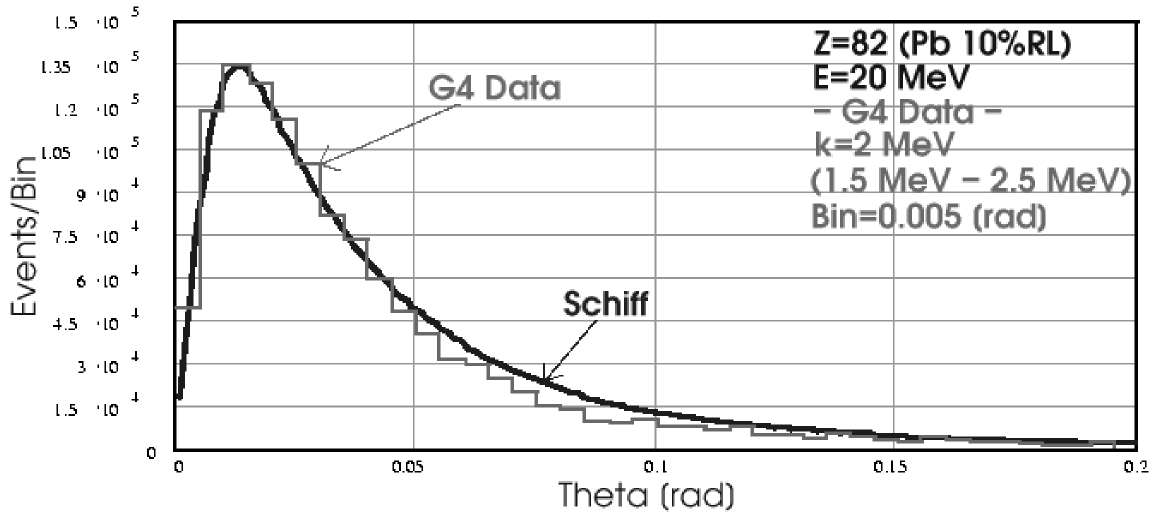

(a) Photon from 1.5 MeV to 2.5 MeV

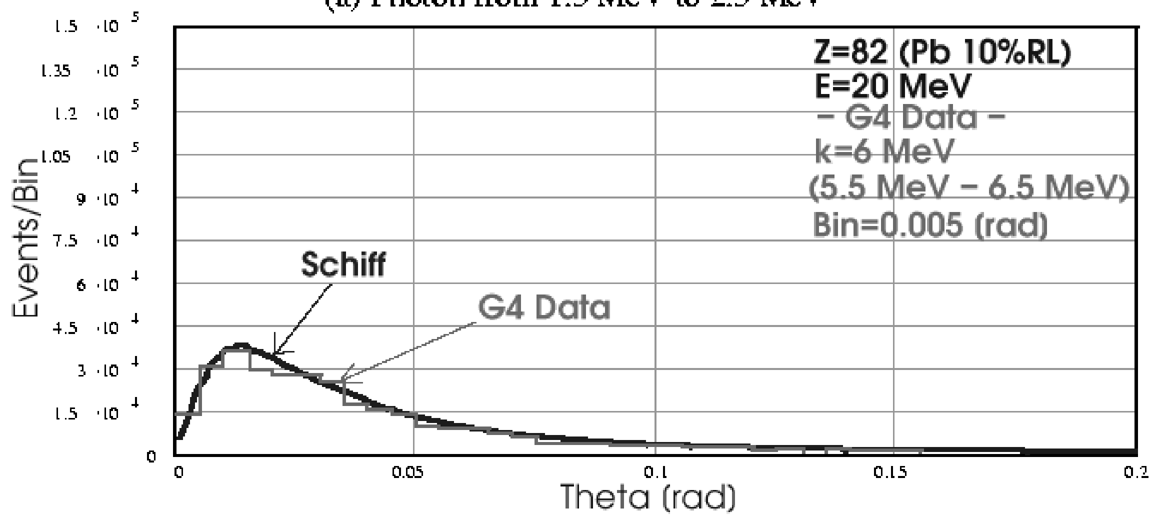

(b) Photon from 5.5 MeV to 6.5 MeV

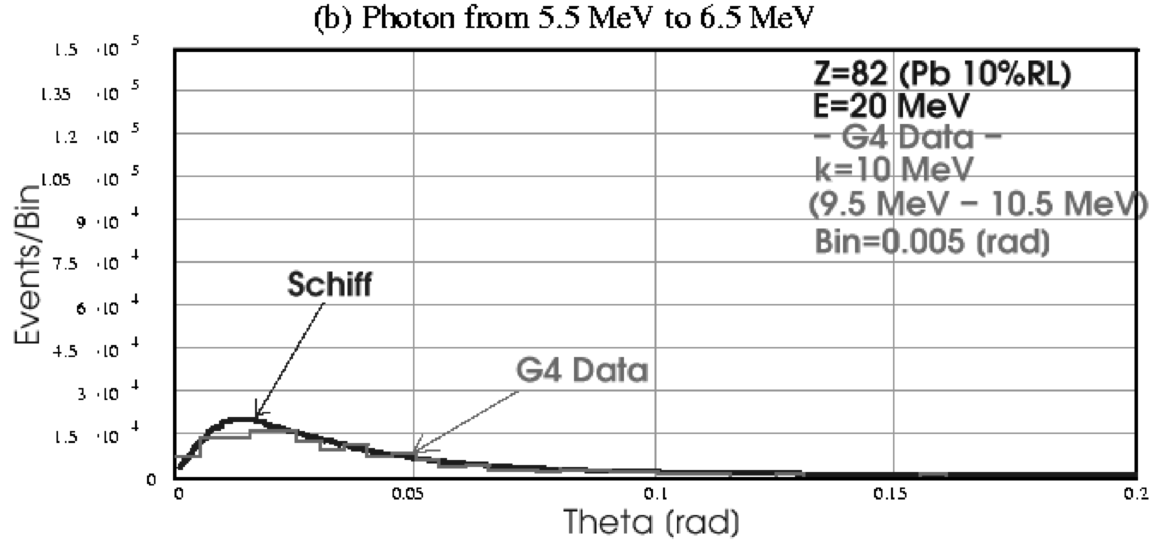

(c) Photon from 9.5 MeV to 10.5 MeV

Figure 5.6: The angular distribution of emitted photon generated by bremsstrahlung of electron of 20 MeV. Solid lines and histograms represent the equation 5.7 and the Geant4 data, respectively.

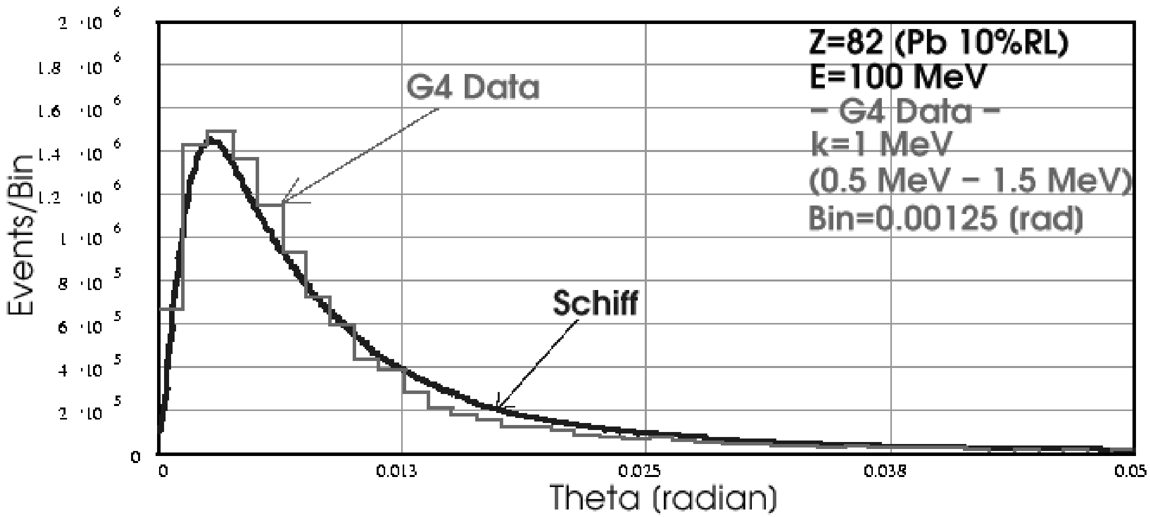

(a) Photon from 0.5 MeV to 1.5 MeV

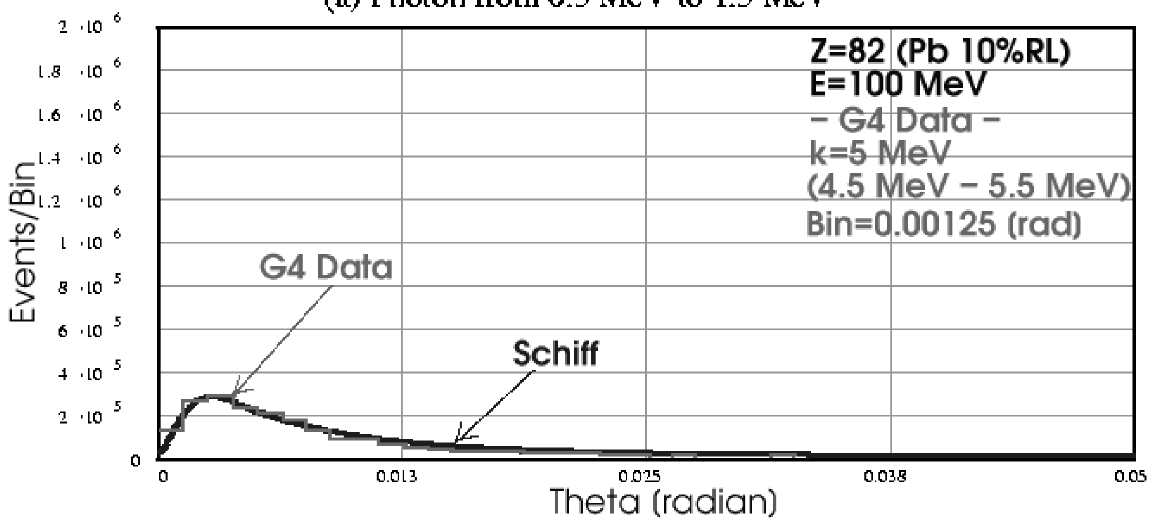

(b) Photon from 4.5 MeV to 5.5 MeV

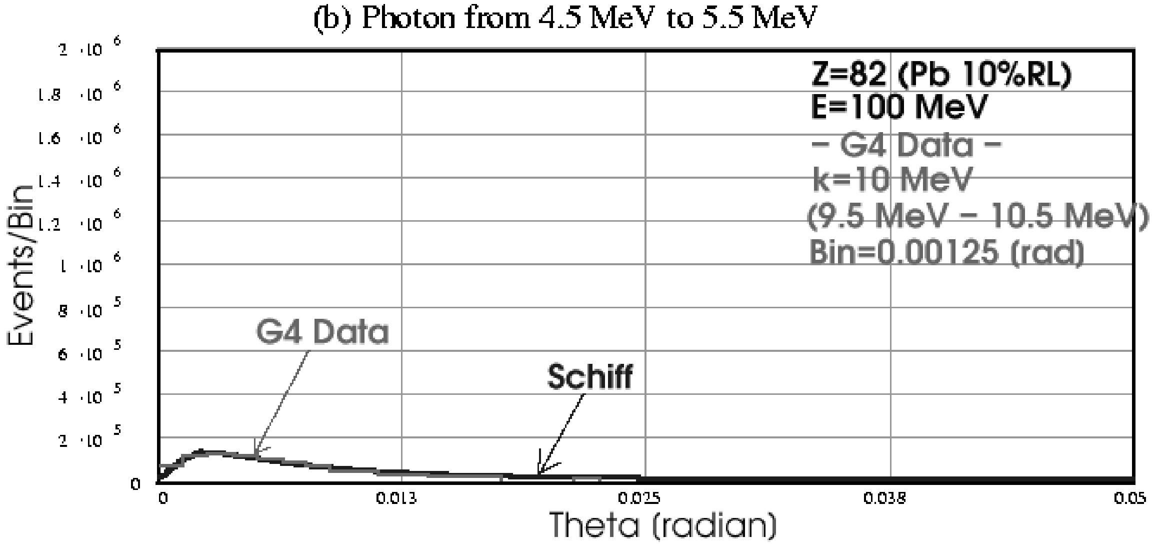

(c) Photon from 9.5 MeV to 10.5 MeV

Figure 5.7: The same as Figure 5.6 but for 100 MeV electrons.

5.3 Pair Creation

Among physical processes in the GLAST simulation, pair creation is one of the most important processes because this is a main process of electromagnetic shower, through which the energy and direction of the incident gamma-rays are determined. Therefore the validation of this process is an essential issue for the GLAST simulation, as well as for the pursuit of the reason for the narrow shower development of the Geant4 found in Chapter 4. In this section we investigate the cross section of pair creation and angular distibution of emitted e^+/e^- generated by pair creation in the Geant4 simulation.

5.3.1 Cross Section

The incident gamma-rays are converted into e^+/e^--pair in the tracker. Then the trajectories of the e^+/e^--pair are reconstructed to determine the direction of the gamma-rays. The converter used in the GLAST is a lead. Therefore we have compared the cross section of photon in a lead calculated in the Geant4 with that of theoretical values. The theoretical values are calculated by "XCOM program". This program calculates the cross sections for pair production, as well as compton scattering and photoelectric absorption, for any element, compound or mixture (Z<100), at energies from 1 keV to 100 GeV. This program can be refered to at "http://physics.nist.gov/PhysRefData/Xcom/Text/XCOM.html". In the program, the cross sections for pair production are based on complicated combinations of formulas from Bethe-Heitler theory with various other theoretical models to take into account screening, coulomb, and radiative corrections.

In the Geant4 simulation the cross section of photon in all materials we defined are calculated at the beginning of the simulation. This algorithm is written in the Geant4 code, G4GammaConversion.cc and we have modified some programs to extract these cross sections in a lead in this code. The information extracted here are the cross sections of pair creation in each energy step defined originally in the Geant4, the scattering angle of e^+/e^-, the energy of the gamma before pair production and the e^+/e^- energies after the pair creation. The data except for the cross sections are used in the later analysis of the angular distribution. We have compared these cross section with XCOM data and have showed the result in Figure 5.8. From the plot it can be found that the Geant4 shows a good description of the cross section of pair creation from 100 keV to 100 GeV. In the following analysis we will examine the angular distribution.

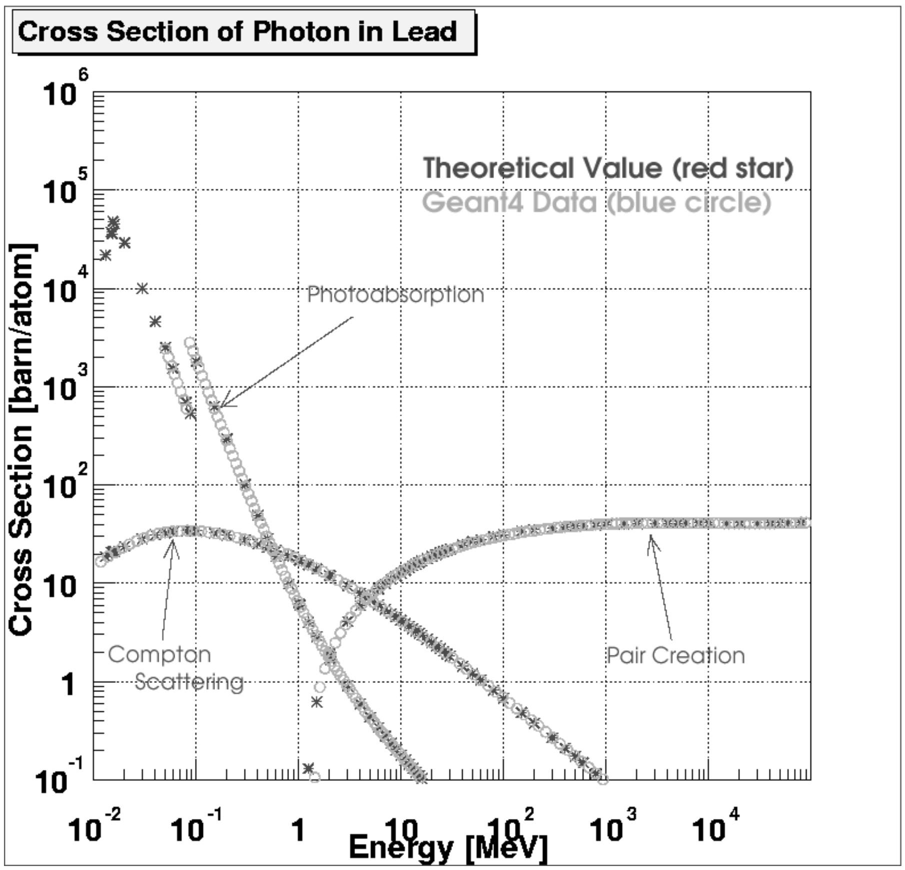

Figure 5.8: The cross sections of photon in the Geant4. The target material is a lead. The red stars and blue circles represent the cross section of the theoretical values calculated by XCOM and those calculated in the Geant4, respectively.

5.3.2 Angular Distribution in Geant4

In this section we investigate the angular distribution of the pair creation in a lead. The angular distribuiton of pair production is also calculated in the Geant4 code, G4GammaConversion.cc. According to the airticle [16], in the Geant4 the azimuthal angle is generated isotropically. The polar angle distribution is calculated based on an approximation of the Tsai formula [12, 13]. The differential cross section of the original Tsai equation is given as,

$$\frac{d\sigma}{d(pc)d\Omega} = \frac{2\alpha^3(\hbar c)^2}{\pi k}\frac{E^2}{(m_e c^2)^4}\left\{\left[\frac{2x(1-x)}{(1+u^2)^2} - \frac{12u^2x(1-x)}{(1+u^2)^4}\right](Z^2+Z)\right.$$
$$\left. + \left[\frac{2x^2-2x+1}{(1+u^2)^2} + \frac{4u^2x(1-x)}{(1+u^2)^4}\right]\left[X - 2Z^2 f((\alpha Z)^2)\right]\right\} \tag{5.8}$$

where

$$u = \frac{E\theta}{m_e c^2}$$

$$X = \int_{t'_{min}}^{(m_e c^2)^2(1+u^2)^2} [G_Z^{el}(t) + G_Z^{inel}(t)]\frac{(t - t'_{min})}{t^2}dt$$

$$t'_{min} = [k(m_e c^2)^2(1+u^2)^2/2E(E-k)]^2$$

$G_Z^{el,in}(t)$ atomic form factors

f Coulomb correction

$\alpha = 1/137$ fine structure constant

where k is the photon energy, p and E are the momentum and the energy of e^+/e^- pair, respectively, $x = E/k$, Z is the atomic number of a material and m_e is the electron mass. Since this equation is quite complicated to sample and depends very weakly on Z, E, k and x, the following approximated distribution as a function of $u = E\theta/m_e c^2$ is utilized in the Geant4 [16].

$$f(u) = C\left(ue^{-au} + due^{-3au}\right) \tag{5.9}$$

where

$C = \frac{9a^2}{9+d}$ $\quad a = 0.625 \quad$ $d = 0.13\left(0.8 + \frac{1.3}{Z}\right)\left(100 + \frac{1}{k}\right)(1+x)$

Where k is in GeV. At first we have confirmed whether the Geant4 reproduces the angular distribution of the equation 5.9. We have examined the angular distribution of electrons of 4 MeV, 10 MeV and 18 MeV generated by pair production of incident gamma of 20 MeV. In the Geant4 simulation we have constructed the same lead absorber in the analysis of bremsstrahlung. The number of gamma we shot is 100k and it's energy is 20 MeV. The cutoff energy is same as that used in the simulation of Moller scattring. We have modified G4GammaConversion.cc to extract the data of pair creation as we have done in the investigation of cross section and have selected events where pair creation occurred first.

The results are shown in Figure 5.9. We have normalized the equation 5.9 so that the height of the peak in the approximated Tsai distribution coincides with that of the Geant4 data since only the shape has meaning. There exists clear discrepancy between the Geant4 data and the proposed approximated formula, especially in low energy. Futhermore, the angular distributions reproduced by the Geant4 did not depended on the energies of electrons although the approximated distributions proposed in the airticle do depend on them. We therefore conclude that the polar angular distribution of e^+/e^- created by pair creation is inappropriate in the current Geant4 (Geant4 2.0).

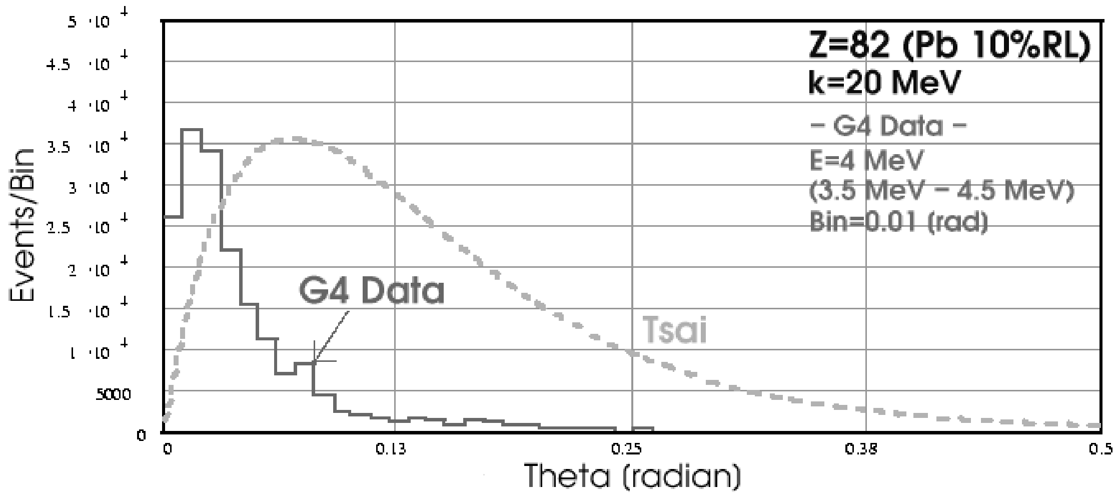

(a) Electron from 3.5 MeV to 4.5 MeV

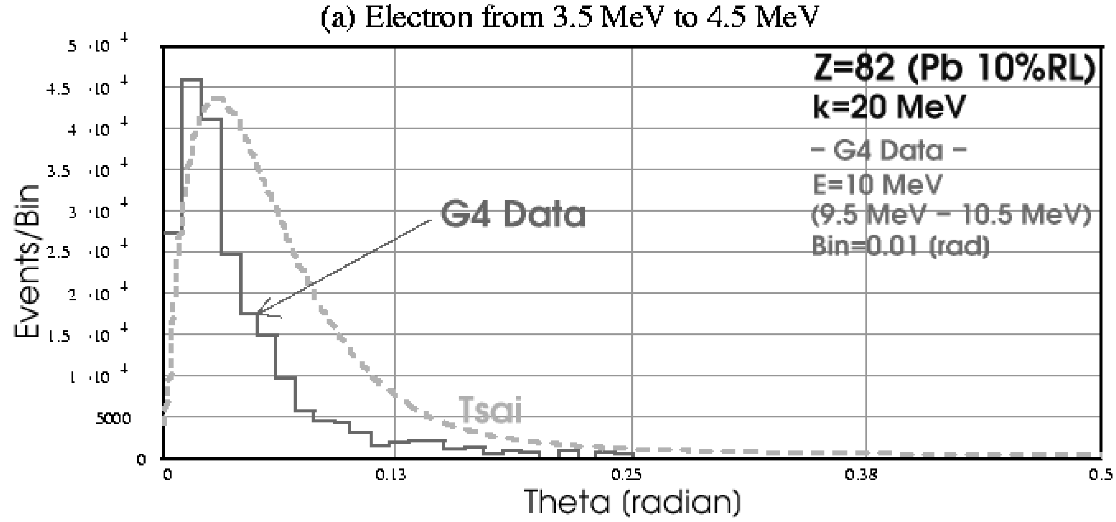

(b) Electron from 9.5 MeV to 10.5 MeV

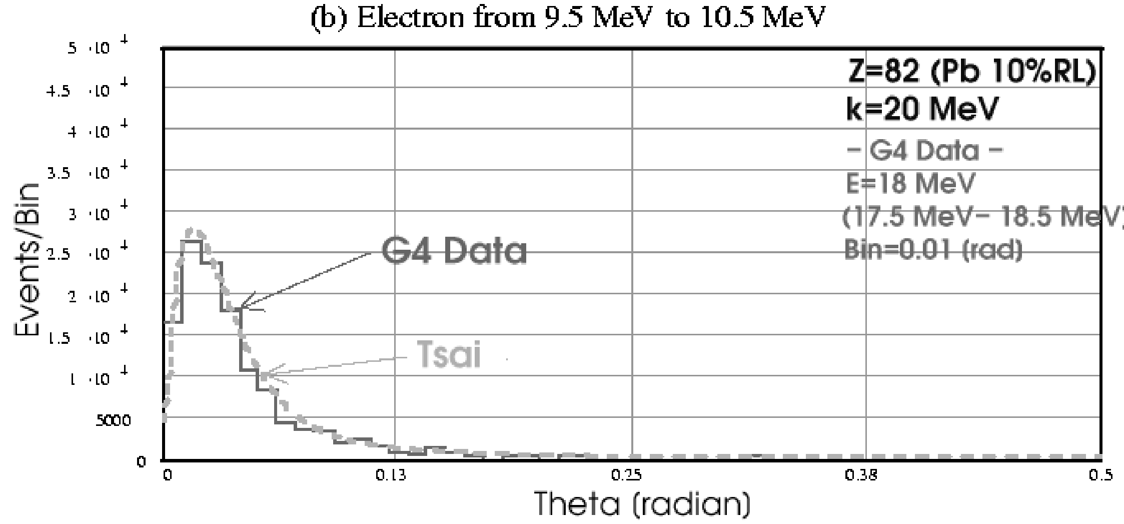

(c) Electron from 17.5 MeV to 18.5 MeV

Figure 5.9: The angular distribution of emitted electron generated by pair creation of gamma of 20 MeV. Dashed lines and histograms represent the equation 5.9 and the Geant4 data, respectively. As for the distribution of the equation 5.9, only the shape has meaning.

Modification of G4GammaConversion.cc To pursue the origin of the discrepancy found, we have studied the Geant4 code, G4GammaConversion.cc and have found the following clear difference between the formula mentioned above and the one actually implemented in the Geant4. Those are summarized below.

(1) The scattering angle, θ, used in the present Geant4 code was defined as $u = k\theta/m_ec^2$ instead of $u = E\theta/m_ec^2$ (equation 5.9). This indicates that the angular distribution is independent on the energies of emitted electron/positron.

(2) The Geant4 samples e^- direction as (dx, dy, dz) and e^+ direction as (-dx, -dy, dz) with respect to the direction of the incident photons, (0, 0, dz), although these directions should be determined independently, like EGS4.

(3) The Geant4 uses the constant, $d = 27$, to determine the angular distribution. However it should be a valiable according to "Geant4 Physics reference manual"[14].

Here, we propose the distribution as a function of $u = E\theta/m_ec^2$, with constant d in order to solve the discrepancy simply. (Note that this modification makes the angular distribution depend on the e^+/e^- energy.) Our function and the equation 5.9 are shown in Figure 5.10. The current angular distribution of the Geant4 (solid lines) does not depends on e^+/e^- energy although the equation 5.9 (thin dased lines) and that proposed by us (thick dashed lines) depend on it. This figure also shows no significant difference between the formula with constant d (thick dased lines) and that with valiable d (thin dashed lines), which means the (3) does not cause the serious problem.

We have thus modified (1) and (2) in G4GammaConversion.cc and have reproduced pair creation in the Geant4 simulation under the same condition as we have simulated in the previous simulation (§5.3.2). Figure 5.11 compared the polar angle distribution of electrons in the Geant4 between the original and modification, together with the equation 5.9. The distribution after the modification is shown by the histograms. After the modification the angular distribution of the Geant4 becomes coincident with the equation 5.9. In conclusion we have modified the angular distribution of the Geant4 appropriatelly.

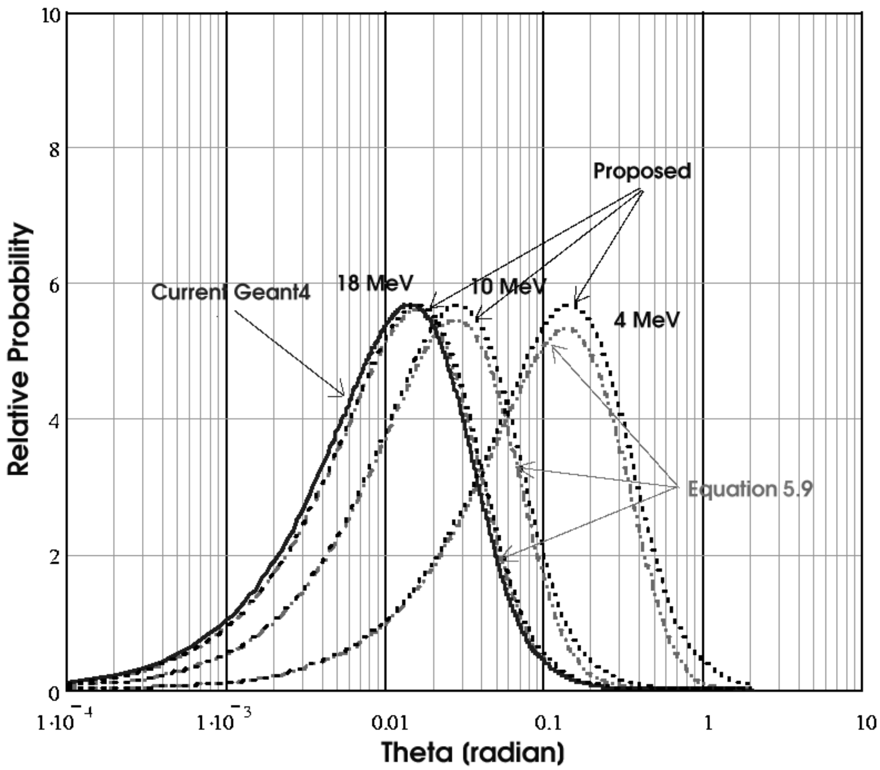

Figure 5.10: Comparison of the three formulas, i.e., polar angle distribution of the equation 5.9, that implemented in the current Geant4 and that after the modification proposed here. The incident energy is 20 MeV, and energy of e^+/e^- are 4, 10 and 18 MeV. Thin dashed lines are the equation 5.9, Thick dashed lines are what is proposed here, and solid line is the current Geant4 implementation. Note that the current Geant4 gives an angular distribution independent of e^+/e^- energy.

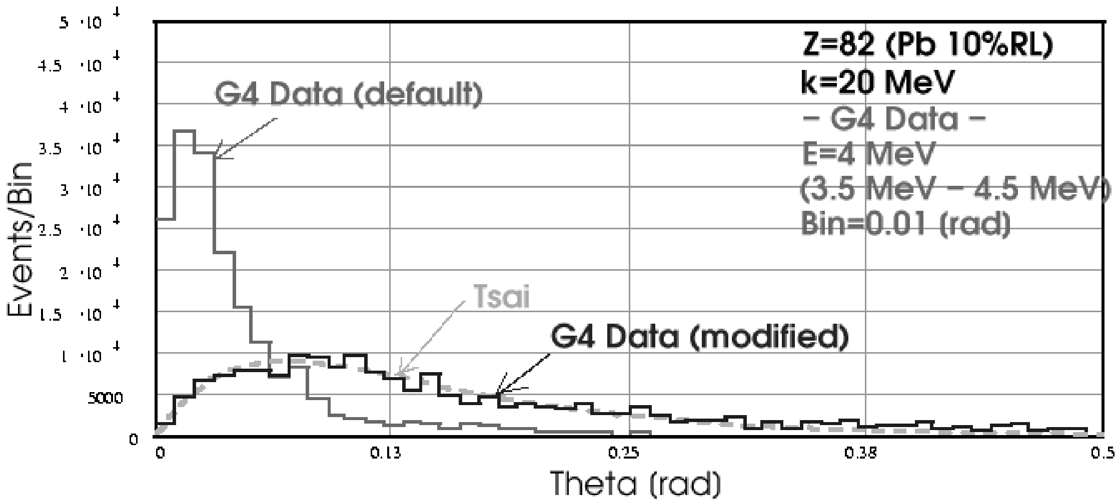

(a) Electron from 3.5 MeV to 4.5 MeV

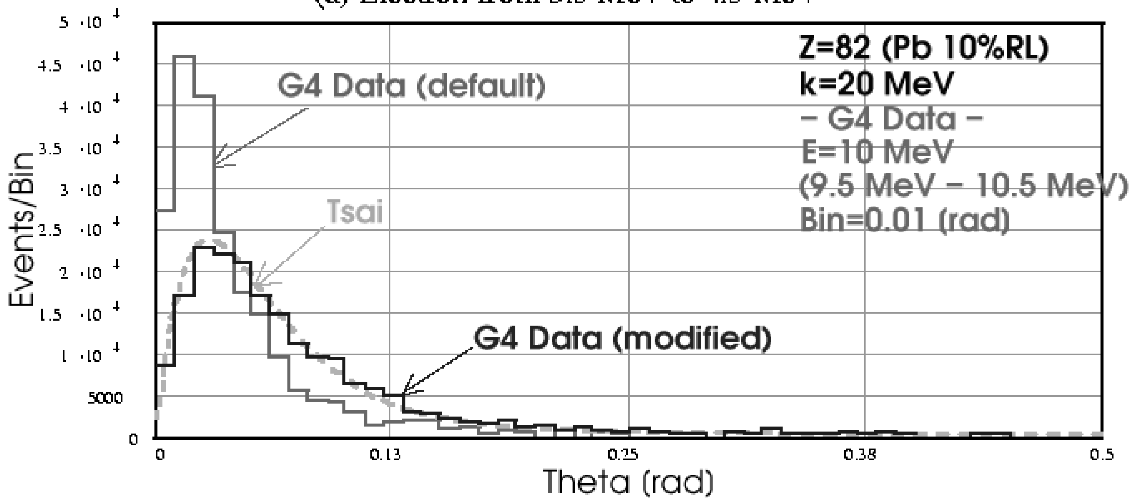

(b) Electron from 9.5 MeV to 10.5 MeV

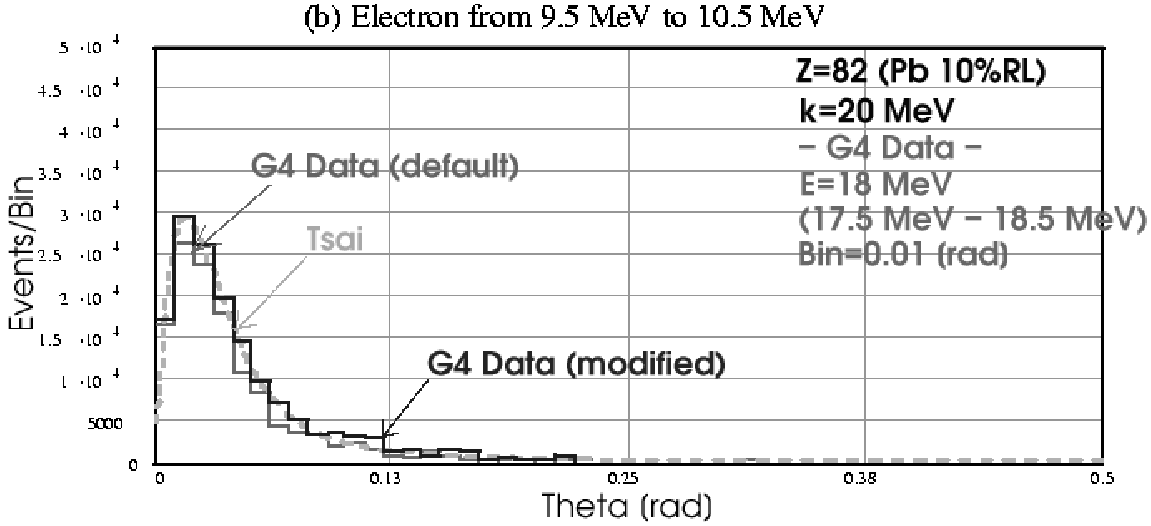

(c) Electron from 17.5 MeV to 18.5 MeV

Figure 5.11: The angular distribution of electrons generated by pair creation of gamma with 20 MeV after the modification of G4GammaConversion.cc. Dashed lines, thin histograms and thick histograms represent the equation 5.9, the Geant4 data before and after the modification, respectively. As for the distribution of the equation 5.9, only the shape has meaning.

5.3.3 Electromagnetic Shower Profile

As a next step we have simulated the electromagnetic shower using the corrected angular distribution to confirm if the narrow shower profile is improved or not. The condition of the simulation is same as that in section 4.1.3. The incident particle is 20 MeV gamma into the cylindrical lead absorber as showen in Figure 4.12. The difference between the shower profile is shown in Figure 5.12. In the plots the shower profiles after changing the angular distribution are shown by dashed lines with asterisks and has not improved very much in the longitudinal and lateral profiles, and still narrower than that of EGS4. Therefore we conclude that the issue (1) and (2) in section 5.3.2 alone can not explain the narrow shower profile of the Geant4.

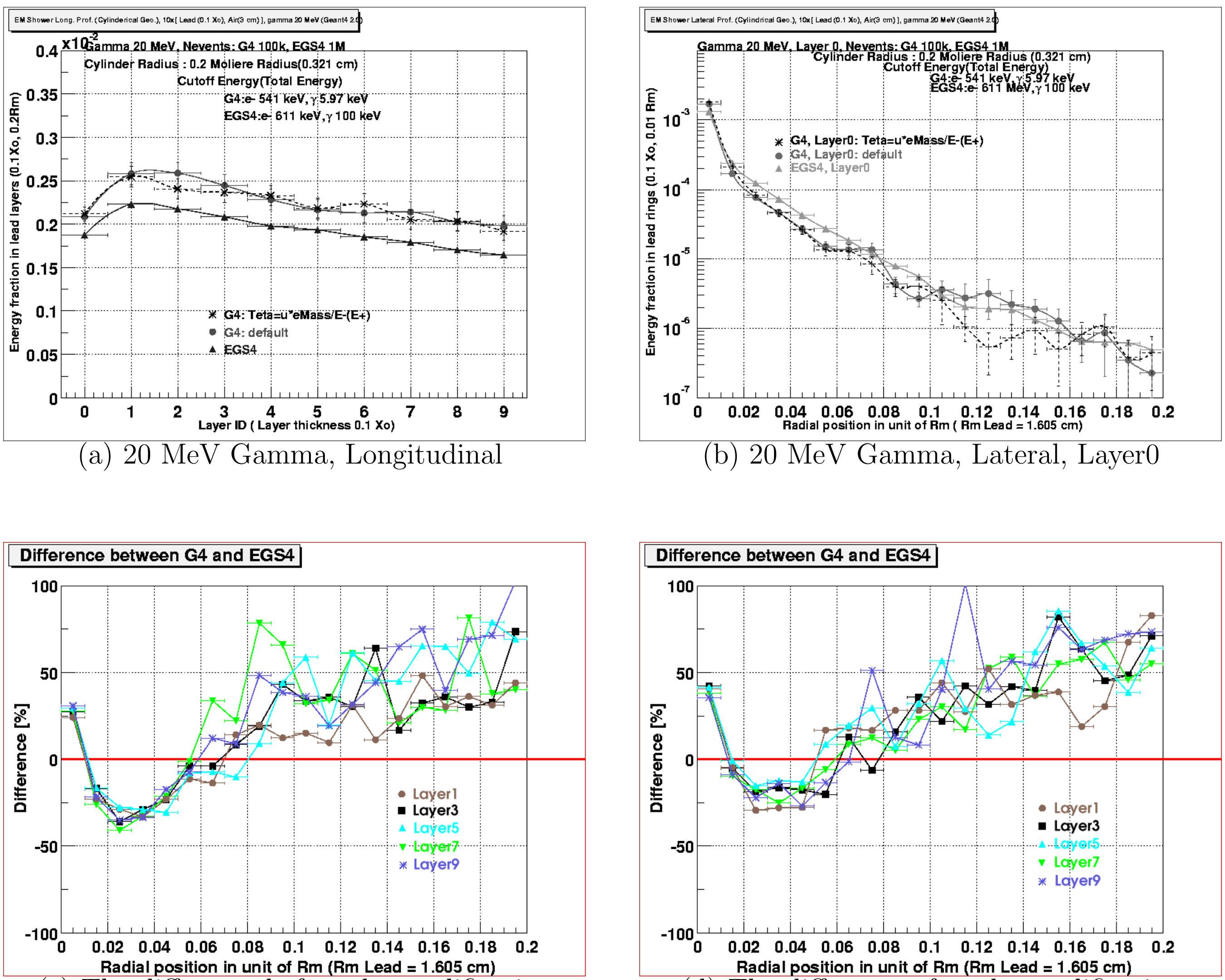

(a) 20 MeV Gamma, Longitudinal

(b) 20 MeV Gamma, Lateral, Layer0

(c) The difference before the modification

(d) The difference after the modification

Figure 5.12: Comparison between the angular distribution before and after the improvement of scaling factor, u, in the equation 5.9. In the plot (a) and (b), dashed lines with asterisks are the shower profile after the improvement. The plots (c) and (d) are the difference in the energy depostions between the Geant4 and EGS4 before and after the modification, respectively.

5.3.4 Comparison with Schiff Distribution

Since the EGS4 utilizes the Schiff formula for angular distribution of e^+/e^-, we compare the angular distribution modified in the previous section with the Schiff formula, the equation 3D-2003 of Motz et al(1969)[17]. Schiff formula is the differential cross section of pair creation in e^+/e^- energy and angle given as

$$\frac{d\sigma^2}{dE_\pm d\Omega_\pm} = \frac{2\alpha Z^2 r_e^2}{\pi}\frac{E_\pm^2}{k^3}\left\{-\frac{(E_+ - E_-)^2}{(u^2+1)^2} - \frac{16u^2 E_+ E_-}{(u^2+1)^4} + \left[\frac{E_+^2 + E_-^2}{(u^2+1)^2} + \frac{4u^2 E_+ E_-}{(u^2+1)^4}\ln M(y)\right]\right\} \tag{5.10}$$

where,

$$u = E_\pm \theta_\pm / m_e c^2; \frac{1}{M(y)} = \left(\frac{k m_e c^2}{2E_+ E_-}\right)^2 + \left(\frac{Z^{1/3}}{111(u^2+1)}\right)^2$$

and other valiables are summarized below,

k	energy of the photon
E_+, E_-	final $e^\pm$ total energy (k=$E_+ + E_-$)
$\theta_\pm$	angle between the outgoing $e^\pm$ and the incoming photon direction (in radians)
$\mathrm{d}\Omega_\pm$	differential solid angle of the outgoing $e^\pm$
Z	atomic number of the target material
r_e	$\equiv e^2/4\pi\epsilon_0 m_e c^2$ (classical electron radius)
α	=1/137 (fine structure constant)

The following table, derived from the Motz et al. article, outlines the essential approximations employed in the development of Schiff formula.

	Approximation	Condition of validity
(1)	Approximate screening potential	$(Ze/r)e^{-r/a}$
(2)	First order Born approximation	$(2\pi Z/137\beta_\pm) \ll 1$
(3)	Extreme relativistic	$E_\pm, k \gg m_e c^2$
(4)	Small angles	$\theta_\pm = O(E_\pm)$
(5)	Negligible nuclear recoil	$k \gg m_e c^2/m_n, k \ll m_n m_e c^2$ (large angles)

We have compared the simulation results of the Geant4 in Figure 5.11 (modified) and Schiff formula. We have also tried 100 MeV gamma. These results are shown in Figure 5.13 (20 MeV) and 5.14 (100 MeV). As a result, we have found that Schiff distribution was dependent on the energy of generated electrons, as well as the distribution after the modification. The Geant4 distribution have agreed with Schiff distribution although some discreancies were seen around the peak of the distribution. The reason of this discrepancy is unknown. However it can not be the serious problem because the cross section of pair creation in the Geant4 coincides with the theoretical values as validated in the beginning of the analysis of pair creation (§5.3.1).

5.3.5 Conclusions

In conclusion, the Geant4 has reproduced the cross section of pair creation quite well. As for the angular distribution we have found the problem of implementation of angular distribution

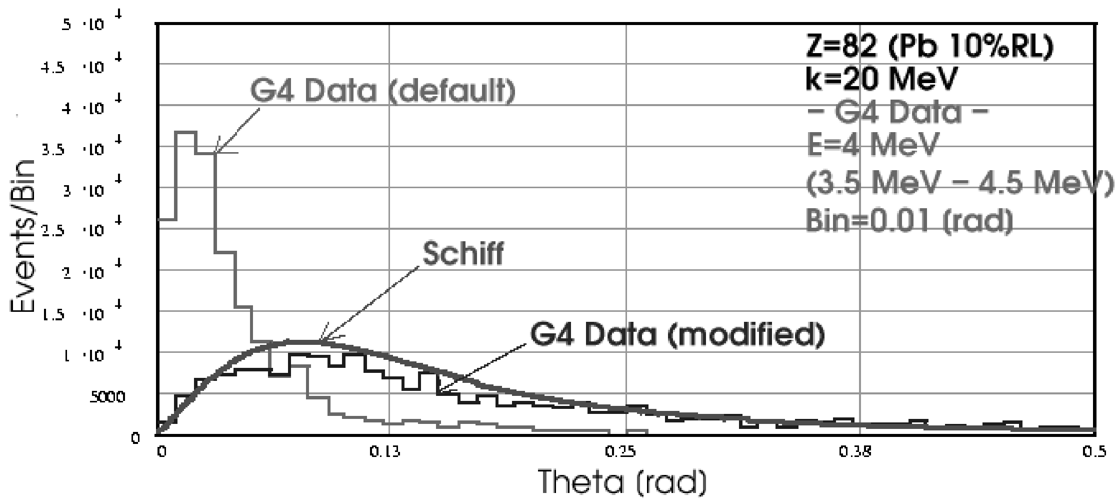

(a) Electron from 3.5 MeV to 4.5 MeV

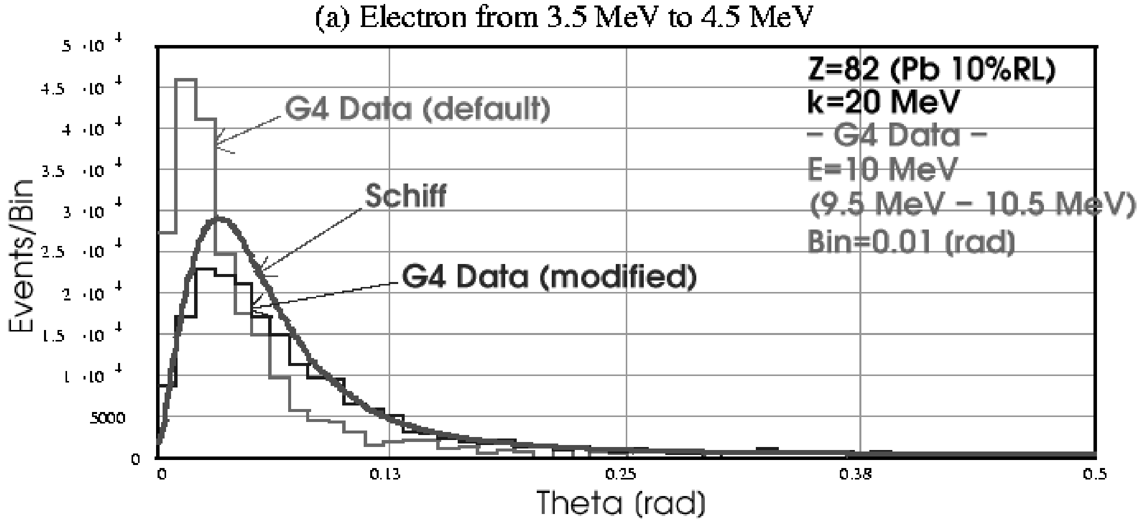

(b) Electron from 9.5 MeV to 10.5 MeV

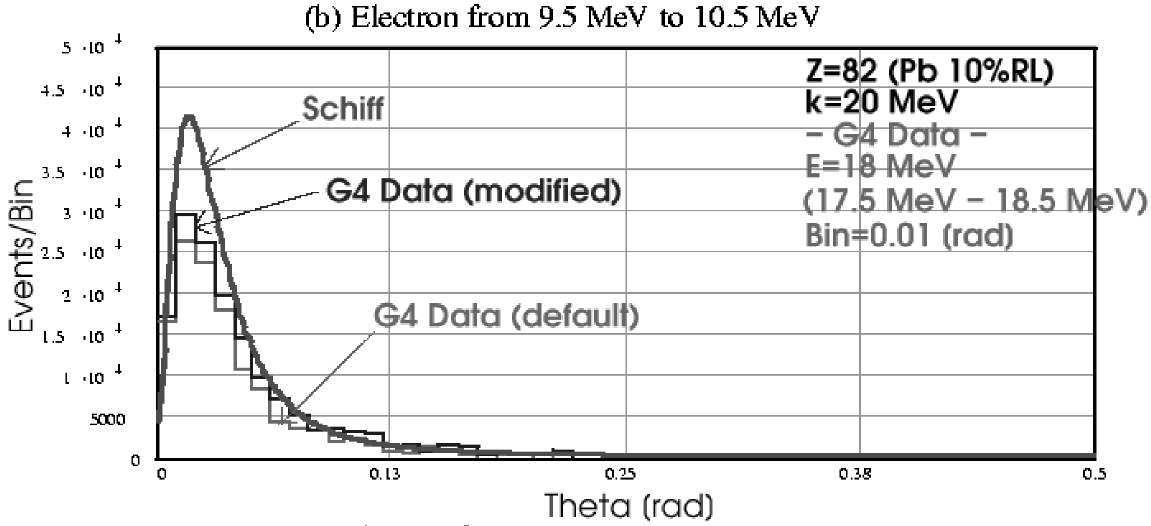

(c) Electron from 17.5 MeV to 18.5 MeV

Figure 5.13: The angular distribution of electrons generated by pair creation of gamma of 20 MeV. Thin histograms, thick histograms and solid lines represent the angular distiribution before and after modification and Schiff formulas, respectively.

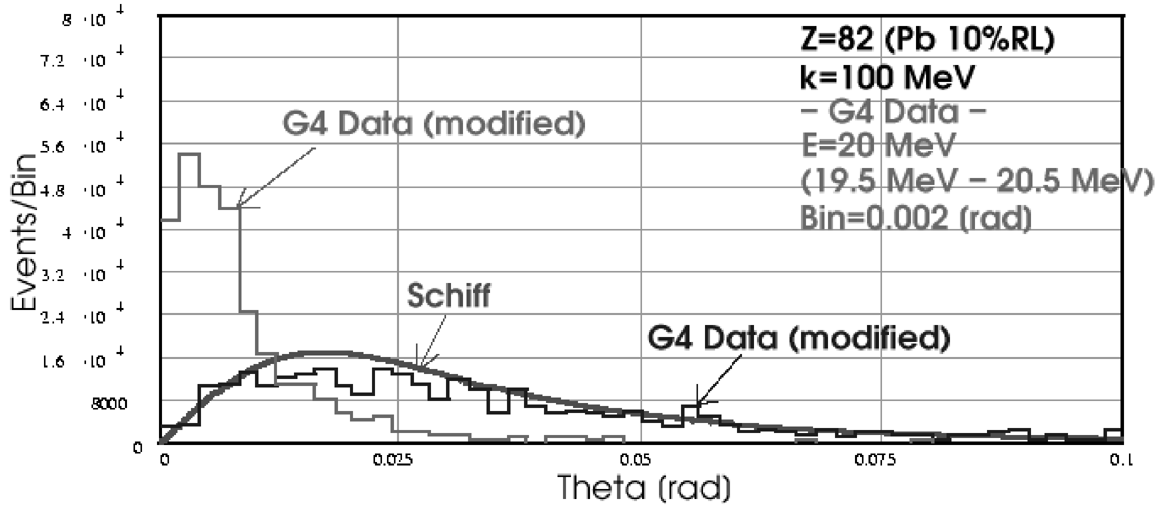

(a) Electron from 19.5 MeV to 20.5 MeV

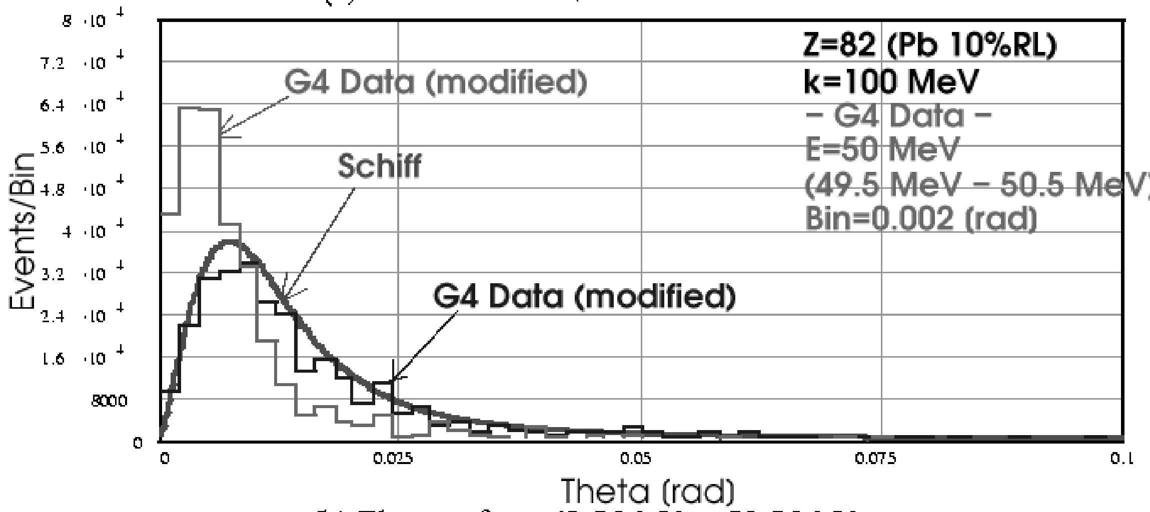

(b) Electron from 49.5 MeV to 50.5 MeV

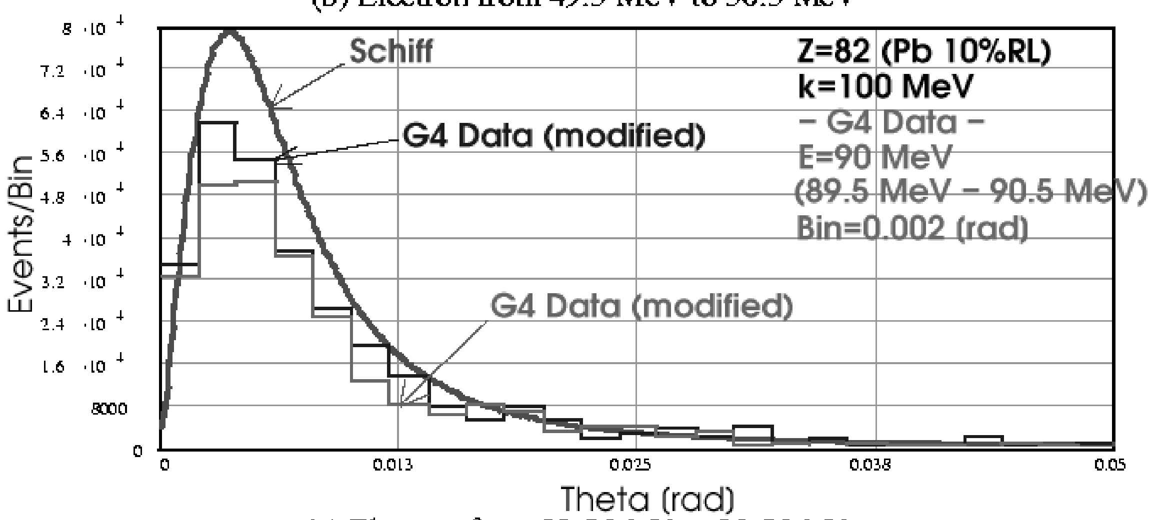

(c) Electron from 89.5 MeV to 90.5 MeV

Figure 5.14: The same as Figure 5.13 but for 100 MeV photons.

and have modified it appropriately. However, the reason of the narrow shower development is still unknown. The rest of the candidates for the discrepancy in the shower profile could be the multiple scattering of electrons.

Chapter 6

Summary

We have systematically validated the physical processes related to the GLAST observation reproduced by Geant4 2.0, e.g., the ionization loss and electromagnetic shower, in order to perform the simulation for the development of the GLAST satellite with a reliability.

In the validation of the ionization, we have investigated Bethe-Bloch formula, Landau distribution and range of protons reproduced by the Geant4. We have found that the Geant4 reproduces these processes well.

As for the electromagnetic shower, the Geant4 has been found to develop the slightly narrower shower profile than that of the experiment and the EGS4 simulation. It has been also found that the discrepancy between the Geant4 and the EGS4 increased as the energy of the incident gamma-rays reduced in the simplfied geometry of the tracker in the GLAST satellite. To pursue the cause of the narrow shower development in more detail, we have examined the processes composed of the electromagnetic shower, e.g., Møller scattering, Bhabha scattering, bremsstrahlung and pair creation. Then the implementation of the angular distribution for pair production in the Geant4 code has been found to be incorrect and we have modified it appropriately. As a result the modifed angular distribution has come to follow the theoretical distribution although the narrow shower development have not improved. The cause of the narrow shower profile is still unknown. The rest of candidate is multiple scattering. We will continuously investigate multiple scattering and check whether the narrow shower profile is improved in the latest Geant4 4.0.

Acknowledgments

This report has benefitted considerably from the guidance of Prof. T. Kamae, Dr. T. Mizuno, Prof. Y. Fukazawa and Prof. T Ohsugi. I am grateful to them for their helpful comments and guidance. I also wish to thank Prof. W. Ralph Nelson and Dr. James C. Liu of Stanford Linear Accelerator Center for giving a lot of advice as to the EGS4. I am indebted to Dr. T. Handa, Mr. T. Ohmoto, Dr. Y. Iwata and Dr. S. Yoshida for their valuable advise on my study. I would like to thank Mr. H. Mizushima, Mr. P. Valtersson, Mr. M. Rortarman, Mr. M. Sjögren, Mr. K Yamanaka, Mr. H. Masuda, and all the members in High Energy Physics Laboratory in Hiroshima University and the GLAST team in Stanford Linear Accelarator Center for the useful discussion. I would also like to thank Ms. K. Hayashi for her office supports.

Appendix A

Shower Profile in Lead and Tangsten

Table A.1: Mean energy leakage

Gamma energy	Mean Energy Leakage	
Tungsten	Geant4 [%]	EGS4 [%]
20 MeV	2.8	2.9
50 MeV	2.4	2.6
100 MeV	1.9	2.4
500 MeV	2.2	2.3
1 GeV	2.2	2.4
5 GeV	3.1	3.2
10 GeV	3.8	3.8
100 GeV	6.3	7.2
Lead		
20 MeV	2.7	2.9
50 MeV	2.4	2.4
100 MeV	2.2	2.2
500 MeV	2.0	2.1
1 GeV	2.1	2.3
5 GeV	3.2	3.1
10 GeV	3.5	3.8
100 GeV	7.1	7.2

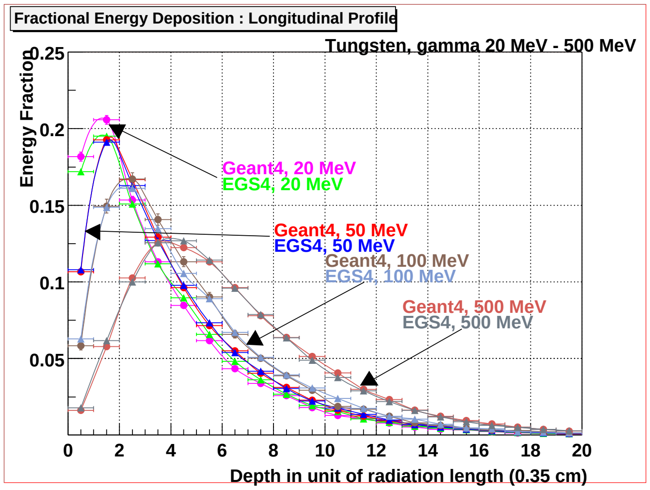

(a) From 20 MeV to 500 MeV gamma, Tungsten

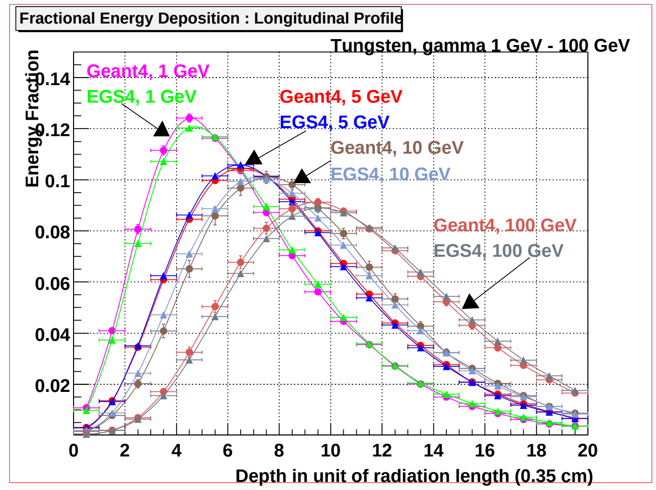

(b) From 1 GeV to 100 GeV gamma, Tungsten

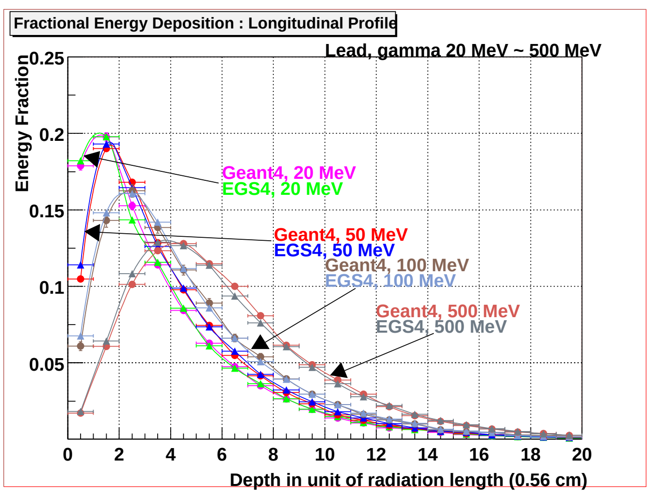

(c) From 20 MeV to 500 MeV gamma, Lead

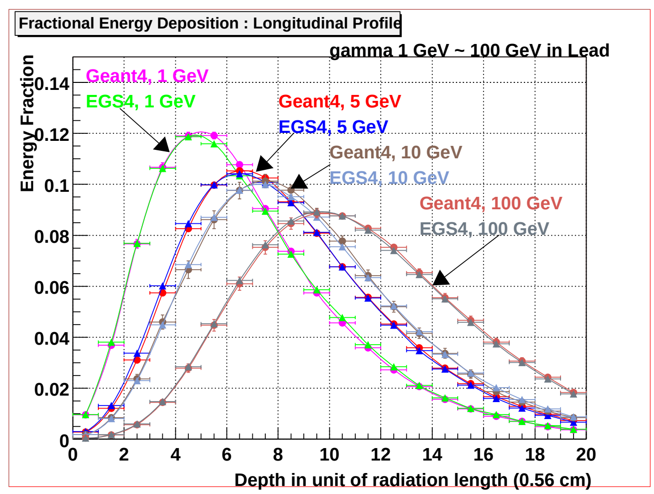

(d) From 1 GeV to 100 GeV gamma, Lead

Figure A.1: The Geant4 and EGS4 longitudinal plofiles of the gamma-induced cascades. The absorbers are lead and tungsten. Filled circles indicate the Geant4 data. Filled triangles are the EGS4 data.

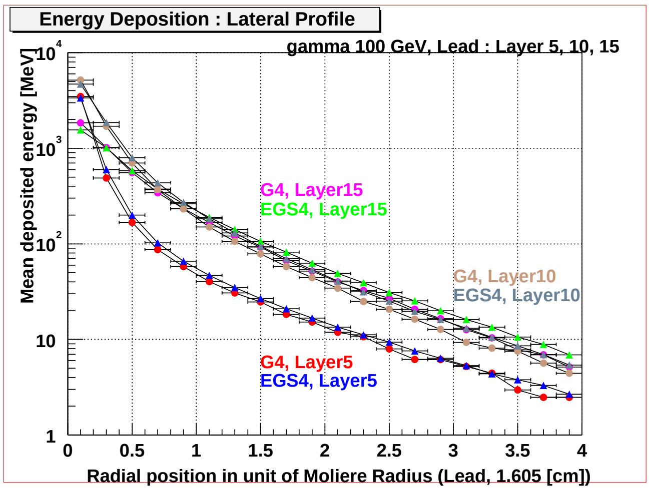

(a) 100 GeV gamma, Lead

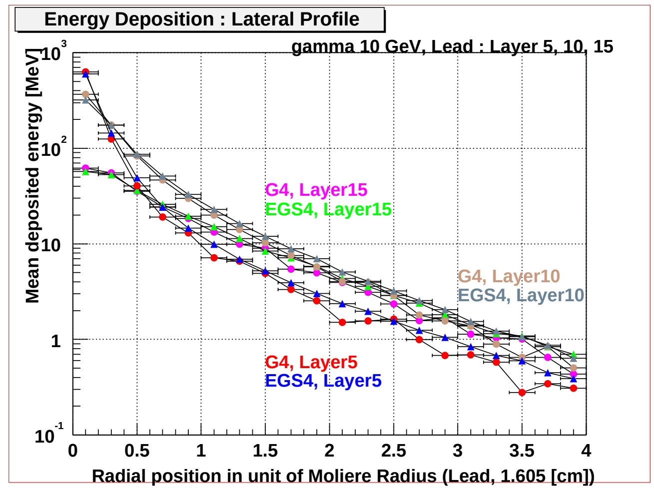

(b) 10 GeV gamma, Lead

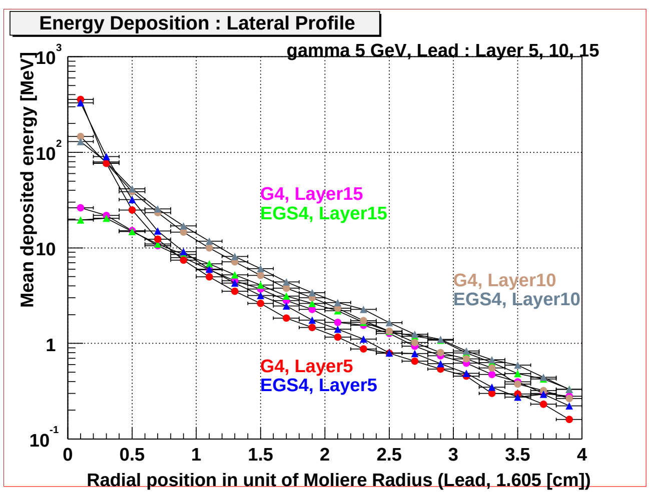

(c) 5 GeV gamma, Lead

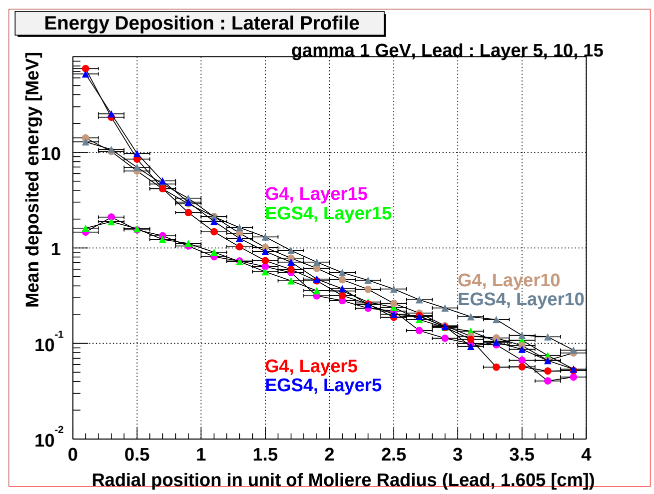

(d) 1 GeV gamma, Lead

Figure A.2: The Geant4 and EGS4 lateral profile of the gamma-induced cascades. The absorbers are lead. The energies of gamma are 100 GeV, 10 GeV, 5 GeV, and 1 GeV. Filled circles indicate the Geant4 data. Filled triangles are the EGS4.

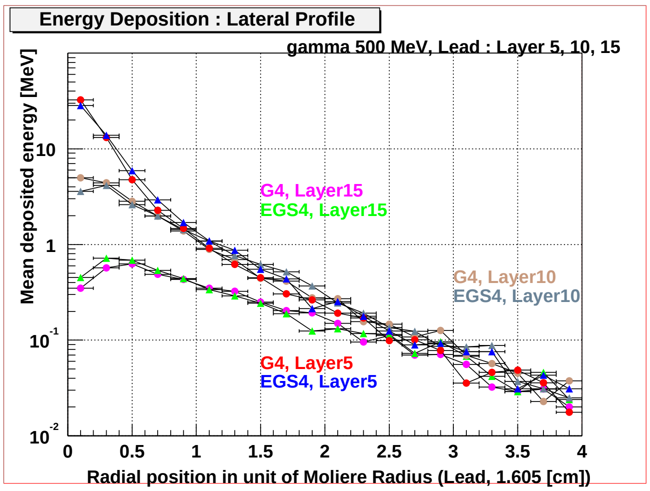

(e) 500 MeV gamma, Lead

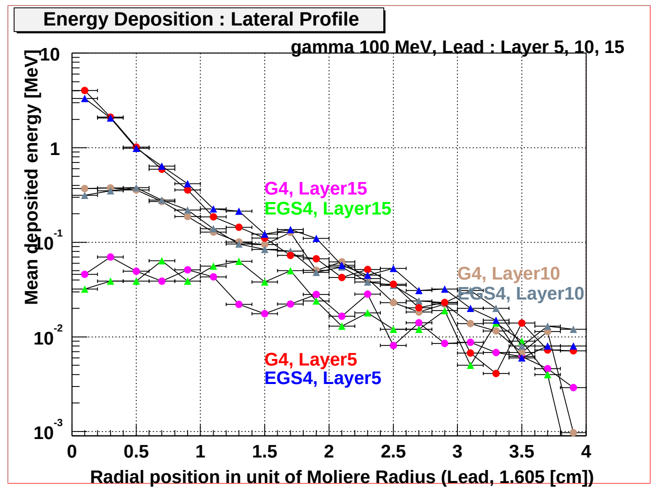

(f) 100 MeV gamma, Lead

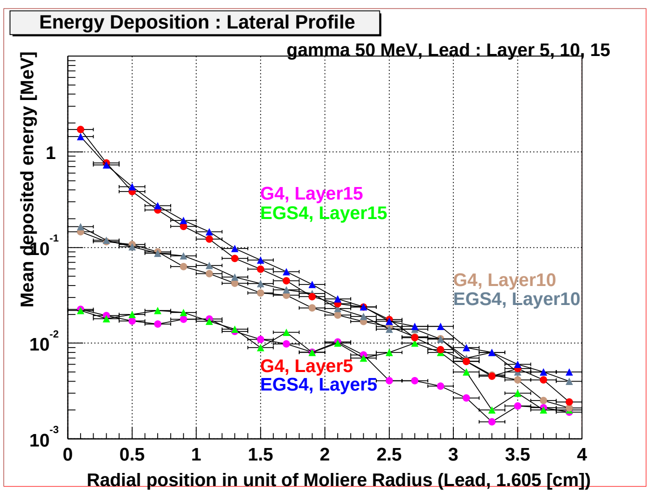

(g) 50 MeV gamma, Lead

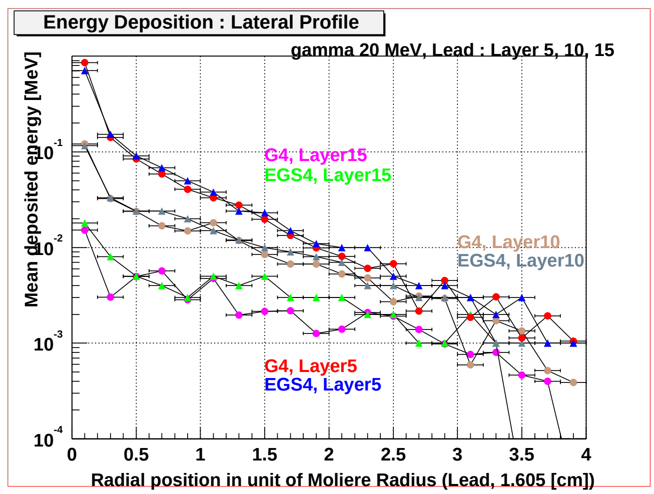

(h) 20 MeV gamma, Lead

Figure A.3: Same as Figure A.2, but the energies of gamma are 500 MeV, 100 MeV ,50 MeV, and 20 MeV.

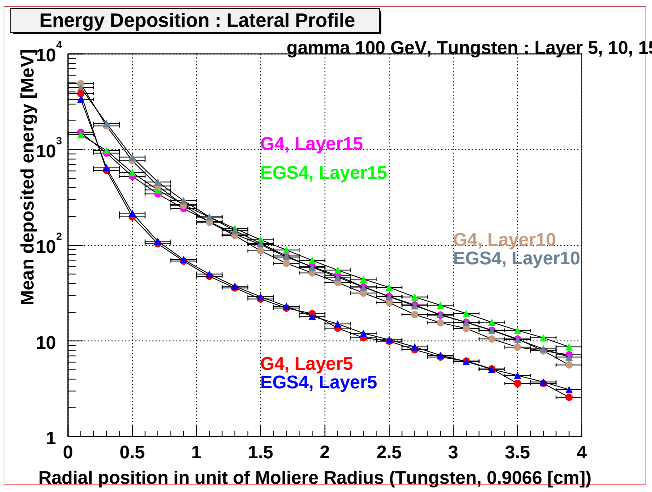

(a) 100 GeV gamma, Tungsten

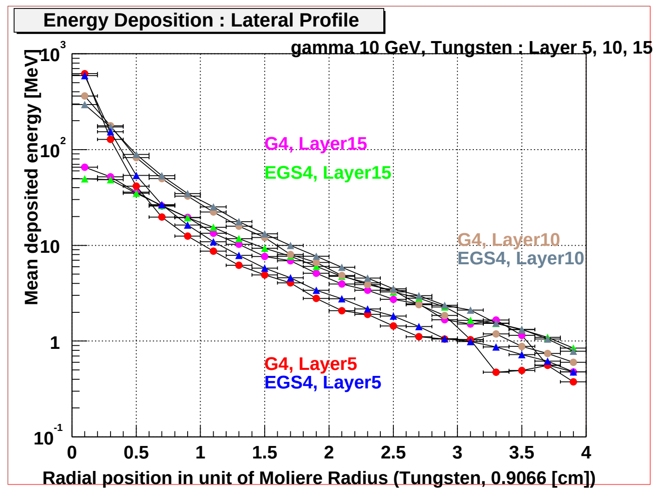

(b) 10 GeV gamma, Tungsten

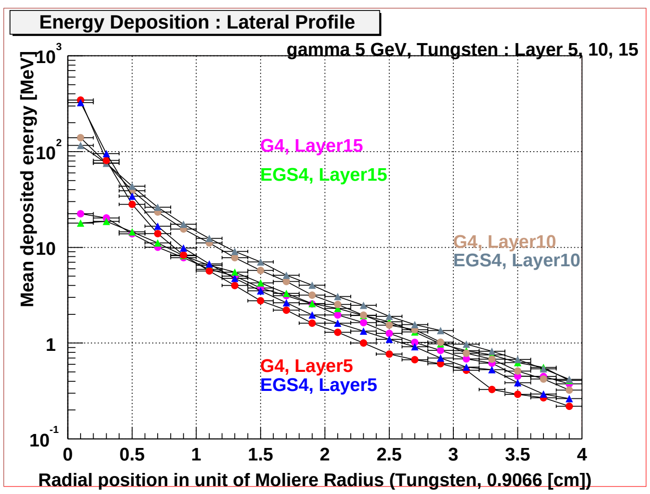

(c) 5 GeV gamma, Tungsten

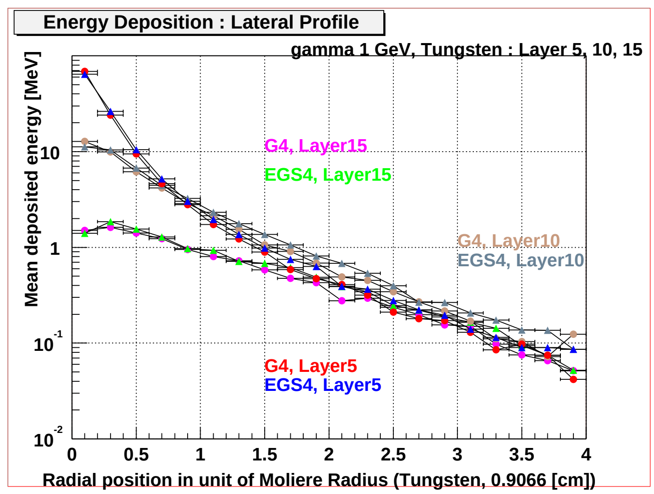

(d) 1 GeV gamma, Tungsten

Figure A.4: The Geant4 and EGS4 lateral profile of the gamma-induced cascades. The absorbers are tungsten. The energies of gamma are 100 GeV, 10 GeV, 5 GeV, and 1 GeV. Filled circles indicate the Geant4 data. Filled triangles are the EGS4.

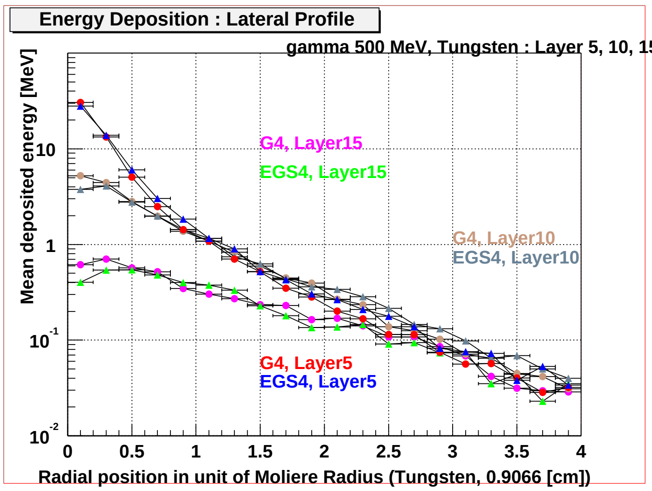

(e) 500 MeV gamma, Tungsten

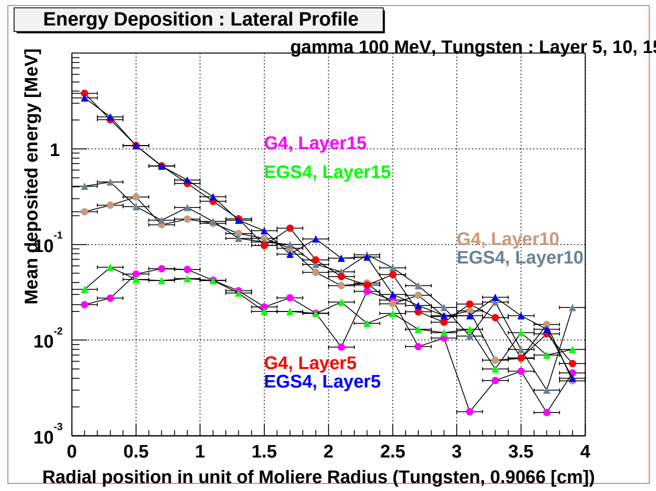

(f) 100 MeV gamma, Tungsten

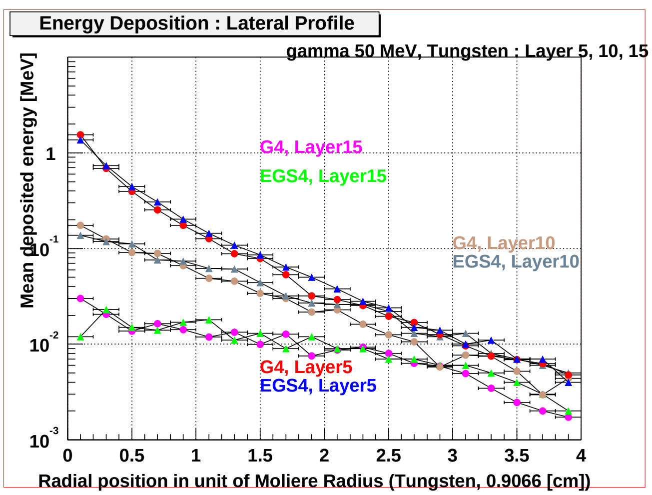

(g) 50 MeV gamma, Tungsten

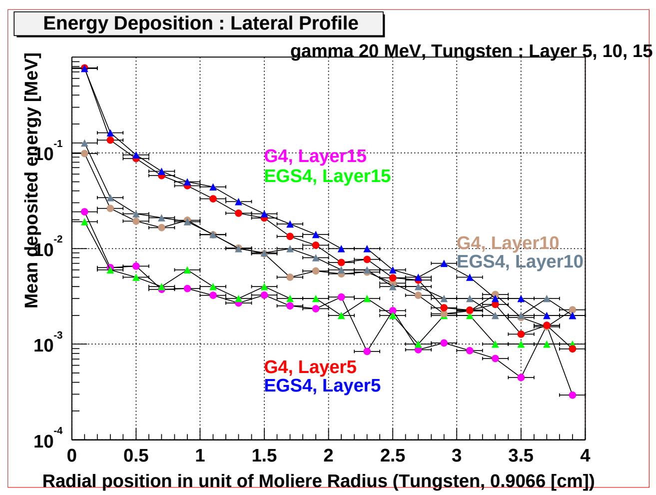

(h) 20 MeV gamma, Tungsten

Figure A.5: Same as Figure A.4, but the energies of gamma are 500 MeV, 100 MeV ,50 MeV, and 20 MeV.

Bibliography

[1] The GEANT4 Collaboration, http://wwwinfo.cern.ch/asd/geant4/geant4.html

[2] *"LAT Science Requirements Document"*, Steve Ritz and Tim Thurston, August, 2000

[3] *"Gamma Ray Large Area Space Telescope Balloon Flight Data Handling Overview"*, E. do Couto e Silva et al. 2001

[4] *Detector Geometry used for Geant4 Balloon Test Simulator (BalloonTestV13)*, T. Mizuno et al. 2001

[5] *Study of Cosmic Ray Background in the Balloon Experiment for the Gamma-ray Satellite GLAST*, H. Mizushima, 2002 (Masteral Thesis)

[6] *"Geant4 Based Cosmic-ray Background Simulator for Balloon Experiments"*, T. Mizuno et al. 2001 (2001 IEEE Transaction of Nuclear Science, submitted)

[7] *"Techniques for Nuclear and Particle Physics Experiments"*, William R. Leo, 1994

[8] *"Particle Physics Booklet"*, Particle Data Group, July, 2000

[9] *"THE EGS4 CODE SYSTEM"*, Walter R Nelson, Hideo Hirayama, and David W. O. Rogers, December 1985; see also the web site: http://pager.lbl.gov/egs/epub.html

[10] *"Electron-Induced Cascade Showers in Walter and Aluminum"*, C. J. Crannell, H. Crannell, R. R. Whitney and H. D. Zeman, Phys. Rev. 184 (1969) 426.

[11] H. Messel and D. F. Crawford. Pergamon Press, Oxford, 1970.

[12] *Pair production and bremsstrahlung of chrged leptons*, Yung-Su Tsai, Rev. Mod. Phys. 46, 815 (1974)

[13] *Erratum: Pair production and bremsstrahlung of chrged leptons*, Yung-Su Tsai, Rev. Mod. Phys. 40, 421 (1977)

[14] *Physics Reference Manual*, December 2000.
or http://wwwinfo.cern.ch/asd/geant4/G4UsersDocuments/Overview/html/index.html

[15] *Bremsstrahlung Cross-section Formulas and Related Data*, H. W. Koch and J. W. Motz, Rev. Mod. Phys. 31, 920 (1959)

[16] Geant3 manual (1993) Phys211

[17] *Pair Production by Photon*, J. W. Motz, Haakon A. Olsen and H. W. Koch, Rev. Mod. Phys. 41, 581-639

[18] *GEANT4 LOW ENERGY ELECTRONMAGNETIC MODELS FOR ELECTRONS AND PHOTONS*, J. Apostolakis et al., 19 August 1999

[19] J. Apostolakis, S. Giani et al., Nucl. Instr. and Meth. A 453 (2000) 597-605.

[20] *Improved angular sampling for pair production in the EGS4 code system* Alex F. Bielajew, August 14 1991

[21] *Improved bremsstrahlung photon angular sampling in the EGS4 code system* Alex F. Bielajew et al., November 14 1989

[22] *Electron Transport Theory, Calculations, and Experiments* C. D. Zerby and F. L. Keller, September 30 1966

[23] *BREMSSTRAHLUNG SPECTRA RROM ELECTRON INTERACTIONS WITH SCREENED ATOMIC NUCLEI AND ORBITAL ELECTRONS*, S.M.Seltzer and M.J.Berger. Nucl.Inst.Meth. B12 (1985) 95-134.